AD_____

Award Number: W81XWH-07-1-0428

TITLE: Department of Defense Era of Hope Scholar Award "Nanotechnology-Enabled Optical Molecular Imaging of Breast Cancer"
(Enter title of award)

PRINCIPAL INVESTIGATOR: Rebekah Drezek, Ph.D.

CONTRACTING ORGANIZATION: Rice University
Houston, TX 77005

REPORT DATE: July 2009

TYPE OF REPORT: Annual Report

PREPARED FOR: U.S. Army Medical Research and Material Command
Fort Detrick, Maryland 21702-5012

DISTRIBUTION STATEMENT:

X □ Approved for public release; distribution unlimited

The views, opinions and/or findings contained in this report are those of the author(s) and should not be construed as an official Department of the Army position, policy or decision unless so designated by other documentation.

REPORT DOCUMENTATION PAGE

Form Approved
OMB No. 0704-0188

Public reporting burden for this collection of information is estimated to average 1 hour per response, including the time for reviewing instructions, searching existing data sources, gathering and maintaining the data needed, and completing and reviewing this collection of information.

1. REPORT DATE *(DD-MM-YYYY)*	2. REPORT TYPE	3. DATES COVERED *(From - To)*
01-07-2009	Annual Report	06/15/2008 - 06/14/2009

4. TITLE AND SUBTITLE

DOD CDMRP Era of Hope Scholar Award: Nanotechnology-Enabled Optical Molecular Imaging of Breast Cancer

5a. CONTRACT NUMBER

5b. GRANT NUMBER
W81XWH-07-1-0428

5c. PROGRAM ELEMENT NUMBER

6. AUTHOR(S)

Rebekah Drezek, Ph.D.

5d. PROJECT NUMBER

5e. TASK NUMBER

5f. WORK UNIT NUMBER

7. PERFORMING ORGANIZATION NAME(S) AND ADDRESS(ES)

Rice University

Houston, TX 77251-1892

8. PERFORMING ORGANIZATION REPORT NUMBER

9. SPONSORING / MONITORING AGENCY NAME(S) AND ADDRESS(ES)

U.S. Army Medical Research and Material
Fort Detrick, Maryland 21702-5012

10. SPONSOR/MONITOR'S ACRONYM(S)

11. SPONSOR/MONITOR'S REPORT NUMBER(S)

12. DISTRIBUTION / AVAILABILITY STATEMENT
Approved for public release; distribution unlimited

13. SUPPLEMENTARY NOTES

14. ABSTRACT

This project focuses on development of nanotechnology-enabled optical molecular imaging technologies for applications in both breast cancer diagnosis and monitoring therapeutic response. The project consists of two major efforts: (1) optical instrumentation technology development and (2) development of complementary engineered nanomaterials for use in conjunction with the instrumentation created to provide molecular specificity. A particularly significant effort is underway to develop needle-compatible fiber optic probes to enable in vivo imaging of tumors with micron resolution in order to provide a new microscopic, high resolution imaging modality to complement the low resolution, macroscopic imaging modalities already in common clinical use. Over the first two years of this effort, a first and second generation needle-compatible fiber optic probe system have been developed as have new methods for synthesis and bioconjugation of shaped and layered gold nanoparticle imaging agents and cadmium-free luminescent quantum dots.

15. SUBJECT TERMS
nanotechnology, molecular imaging, optical imaging

16. SECURITY CLASSIFICATION OF:			17. LIMITATION OF ABSTRACT	18. NUMBER OF PAGES	19a. NAME OF RESPONSIBLE PERSON
					Dr. Rebekah Drezek
a. REPORT U	b. ABSTRACT U	c. THIS PAGE U	UU	105	19b. TELEPHONE NUMBER *(include area code)* 713-348-3011

Standard Form 298

Table of Contents

Introduction…….. 2

Body…….. 3

Key Research Accomplishments…….. 20

Reportable Outcomes…….. 22

Conclusion…….. 24

References……25

Appendices…….. 26

Introduction

There is a critical need to develop new imaging technologies which bridge the gap between our rapidly developing fundamental molecular understanding of breast carcinogenesis and our ability to rationally harness this understanding to develop more effective diagnostic and treatment strategies. Bridging that gap requires developing new tools which can rapidly detect, diagnose, and at times, intervene in the disease process based on recognition of specific molecular signatures of breast cancer *in vivo*. In this project, we focus on the development of miniaturized photonics-based imaging technologies (SOW, Project 1) and complementary nanoscale molecular-targeted imaging agents for detection and monitoring applications (SOW, Project 2 and Project 3) in order to provide a new approach to molecular imaging of breast cancer. Medical imaging plays a prominent role in all aspects of the screening, detection, and management of breast cancer today. A variety of imaging methods including screening and diagnostic x-ray mammography and resonance imaging (MRI) are currently used to evaluate and monitor breast lesions. Although existing imaging technologies provide a useful approach to delineating the extent of tumors, these methods offer only low resolution, non-specific issues of tissue and cannot provide a detailed picture of the molecular profile of a tumor. In addition, techniques such as x-ray imaging and MRI are not able to detect small early cancers or pre-cancerous breast lesions and are difficult to use in settings such as the operating room where near real-time dynamic images are required. Thus, there is a substantial clinical need for novel imaging methods for the detection and monitoring of breast cancers which offer improved sensitivity, specificity, portability, and cost-effectiveness. In this project we develop portable optical technologies which promise high resolution, noninvasive functional imaging of tissue at competitive costs. Optical approaches can detect a broad range of morphological, biochemical, and architectural tissue features directly relevant to characterizing breast lesions including sub-cellular physical parameters such as nuclear size and nuclear to cytoplasm (N/C) ratios and biochemical indicators such as hemoglobin concentration, metabolic rate, and collagen cross-linking levels. To make these technologies even more powerful we expand the current capabilities of photonics-based imaging approaches with the additional capacity to quantitatively and dynamically detect molecular markers of breast cancer *in vivo* without tissue removal (SOW, Project 2). Developing the optical molecular imaging tools and agents for breast cancer which will allow us to accomplish this goal is the focus of this project.

PROGRESS REPORT BODT

The body of the progress report is contained in this section. Over the past year, we have published a number of papers on our work which provide more detailed methods. In those cases, these materials are referred to and the papers appear as pdfs appended to the end of the report. Some of the text in the sections below is derived from those papers and from those which have not yet appeared in print. In general, we have kept the sections of the report focusing on already published work shorter while the portions reporting on work not yet published in the literature are somewhat more detailed. The numbering of projects and tasks discussed in the report corresponds to the numbers used in our currently approved Statement of Work.

Project 1: Needle Compatible-Optical Biopsy (NCOB) System

For background information on our motivation for developing a needle-compatible fiber optic system for breast cancer diagnostic and monitoring applications, information regarding the optical techniques and image analysis strategies we will use, and a description of how our system would interact with the technologies which are standard of care today please see our Year 1 report which covers those issues in detail. Below, we focus on progress on the instrument itself during the past reporting year. As described in the Statement of Work, Year 1 and most of Year 2 plans focused on design of this system and beginning initial construction. It was expected that the system (Figure 1) would be completed approximately 30 months after the design phase and evaluation would begin 2.5 years into the project. We are still ahead of schedule on this project and have built a second generation system which is modular in nature and rapidly reconfigurable – highly desirable properties as the instrument will be used in combination with imaging agents from Project 2 still under development. In this section we present initial data for the system which is already providing >10 micron resolution imaging capability through a needle probe. In Year 3 we will seek permission to modify our program of work to include more extensive clinical evaluation of this instrument than originally anticipated. Plans which note tissue studies and other clinical efforts below will only proceed presuming these modifications to our SOW are accepted and regulatory paperwork is approved.

During Year 2 of this project, to move the Needle-Compatible Optical Biopsy (NCOB) system closer to clinical applications, the needle probe has been made smaller and less invasive without sacrificing image quality. Experiments were carried out to verify the capability of the system to image individual cells. Ultimately, this system is intended for clinical use to

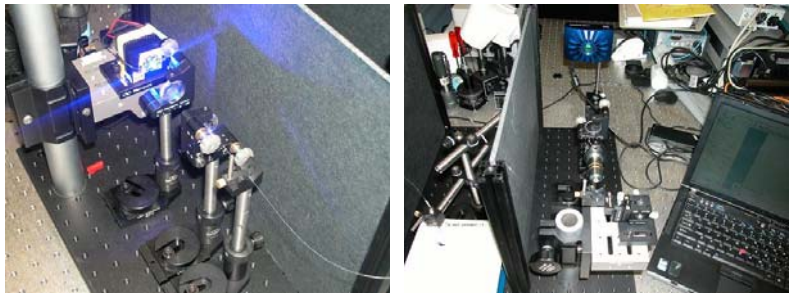

Figure 1: Our first system developed in Year 1 to evaluate a variety of different design considerations and to accommodate the CCD camera.

provide an imaging modality with the resolution to image individual cell morphology, ultimately including nuclear morphology, without any tissue removal from the body. "Optical biopsy" refers to our ability to obtain this information optically without physically acquiring a biopsy sample. To visualize the nucleus of the cell for quantitative cancer assessment, contrast agents will be introduced to enhance nuclear contrast and more elaborate software tools will be used to automatically measure cell and tissue structural characteristics. Additionally, molecular imaging will be achieved with this system through the use of targeted imaging agents under development in Project 2.

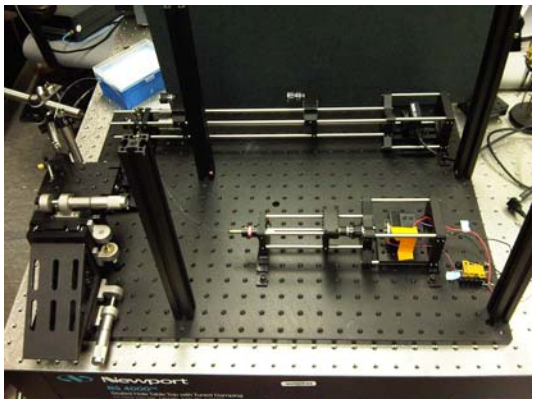

Figure 2: The current setup using a cage system allows facile focusing of the optical components is and very stable when the parts are locked down. The optical sections are also much more compact. This setup is modular for future large section modifications (i.e. illumination section, detector section, and a currently in development fiber bundle projection section).

After a year of testing out different components for the NCOB system, we have found the most suitable individual optical components to be used. It is therefore no longer necessary to use a setup where individual part can be switched out. Instead, a new cage based setup (Figure 2) has been constructed that emphasizes precise spatial adjustment of the optical components and stability once the fine adjustments are done. The new setup is also smaller and more easily isolated in separate compartments. Furthermore, the cage system can be easily broken down into optical sections that encompass numerous optical parts. While the parts are in locked positions relative to each other, the sections themselves can be easily modified. This is a very useful change because we are now implementing a new illumination scheme. Experiments in the last year on tissue mimics have suggested we will want to use imaging agents to improve visualization quality (both to visualize nuclear morphology and to label relevant molecular markers). This is not unexpected and is the motivation for Projects 2 and Projects 3. Because no one has built a system with the design we proposed before, we are learning as we go along what types of modifications are required to obtain images of sufficient quality. We discovered over the past year that given our intended clinical applications and imaging agents, the separate illumination and detection fiber bundles as they existed in the system design we presented last year is not ideal (too much specular reflection). Therefore, a new design has been put in place to minimize specular reflection the details of which are presented later.

Improvement in design: A key objective in the continuing effort to improve the NCOB system is minimizing the device's invasiveness while maintaining sufficient field of view (FOV) and resolution. At the start of the project, we set our goal to match and exceed the standards of core-needle biopsy (CNB) and fine-needle aspiration biopsy (FNAB), currently used to acquire

samples for breast cancer pathology. While our first system introduced a year ago had invasiveness comparable to the CNB (though no tissue is removed from the body), our current system uses a needle probe the size of FNAB needles without the main drawback of that method.

Specifically, the size of our needle probe has been reduced from 14-gauge (2.1 mm outer diameter) to 20-gauge (0.9 mm outer diameter). The improvement has surpassed the conventional CNB needle size of 16-gauge and become comparable to the 18 to 24-gauge needles employed for FNAB (Figure 3). We plan to reduce this diameter further as the project progresses. . In addition, the diagnostic potential of the NCOB has advantages to that of FNAB because the imaging is performed without significantly disrupting the morphology of target tissue allowing visualization of histopathology in addition to the limited cytopathology permitted by FNAB. Furthermore, we do not remove any tissue or cells from the body using our method. The system has met our initial designs goals.

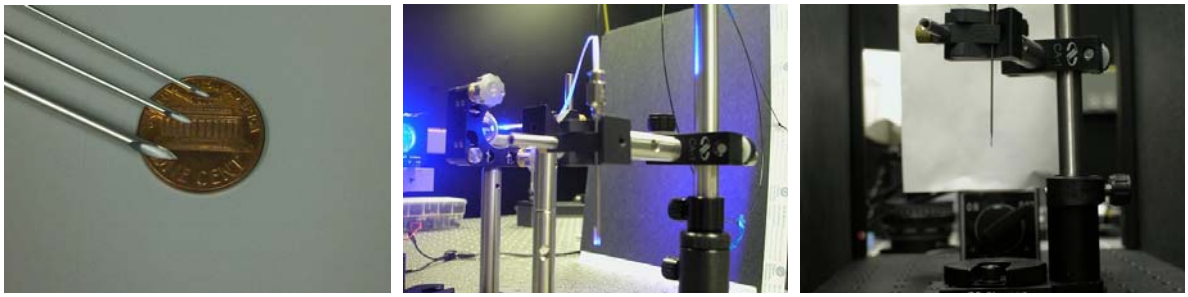

Figure 3: (left) the evolution of the needle probe for our system from 14-gauge to 20-gauge; (middle) the 14-gauge needle probe of the original system; (right) the 20-gauge needle probe of the new system.

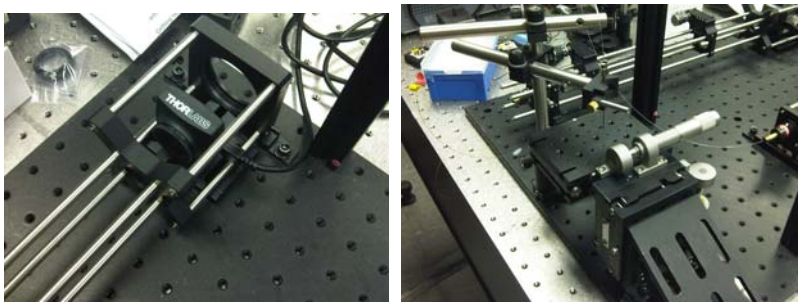

Figure 4: (Left) the new smaller and cheaper CMOS camera; (Right) the three-axis adjustable sample stage.

Besides more precise adjustment, enhanced robustness, and smaller size, the new cage based system has two other improvements (Figure 4) for biological experiments. One improvement is a $300 CMOS camera integrated into the cage system. This camera demonstrated comparable performance to the previous Zeiss camera but is smaller and much cheaper. Although price is not as an important consideration as quality, every bit of savings helps for a device aimed at making breast cancer screening and monitoring accessible to all patients. (We are building a tool which costs less than 5K using off the shelf parts and would

cost far less than that in a manufactured setting.) A second improvement is a three-axis sample stage (Figure 4). Although the system will ultimate use a movable probe, the sample stage will be very useful for the imaging of NP in ex-vivo biological specimens.

Improvement in performance

Using higher quality image guides, the resolution of our system has actually increased as the size of the needle probe decreased. Resolution is currently well below the 10 micron average diameter of the smaller of the cells we will need to view in vivo and provides greater confidence for image the details of both normal and cancerous tissue in the breast. At the same time, the reduction in needle probe size also has raised several potential challenges. A smaller probe also means less illumination and a smaller field of view. Both could adversely affect the performance of the system. After experimentation, however, it was discovered that the current probe does not significantly increase the necessary exposure time of imaging or reduce the FOV below clinically useful levels. The exposure time was increased by only 100% to 1 second, making real time imaging still very much feasible. Although the field of view was reduced to 240 um diameter from 1 mm diameter, this smaller FOV still allows the simultaneous viewing of several hundred epithelial cells. The decrease invasiveness to the patient and the improved resolution more than make up for these marginal drawbacks.

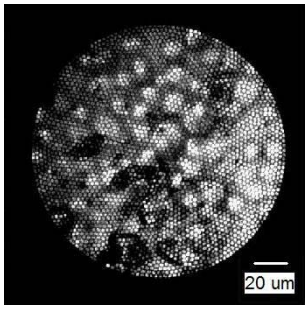

Figure 5: First images with second generation system shows the ability to detect individual breast cancer cells.

First Imaging Results

Our imaging work is slated to begin in Month 31 (this report covers Months 13-24). However, we are ahead of schedule and our now beginning to conduct these experiments which will be the primary focus of Year 3 of the project. The imaging of breast cancer is complicated by the need to discern specific disease features within a complex background of other breast structures. Figure 5 shows cultured SkBr3 breast cancer cells imaged by the NCOB system. As shown in the image, we are able to image at a cellular level visualizing individual breast cancer cells. Extensive imaging of cells in 3D constructs will be a focus of the next year with particular emphasis on using simple chemicals already in routine clinical use (toluidine blue, acetic acid, etc.) to stain nuclei for visualization and in our first assessment of the use of Project 2 imaging agents in conjunction with the Project 1 imaging system.

Illumination/detection fiber bundle projection

In order to improve the system to enable molecular imaging in vivo, a scheme to substitute the old probe, which consisted of separate illumination and detection fiber bundles with just an image guide is being implemented (Figure 6). This approach is advantageous because it strikes a good compromise between resolving specular reflection and making a small optical fiber probe. Bifurcated fiber bundles that split illumination and detection fibers at one end are hard to make

and are not readily available at the sub-millimeter size we require. However, any reflectance based imaging using optical fibers would benefit greatly from separate illumination and detection fibers, especially if they can be arranged into specific shapes.

Our approach uses a single image guide for the probe, but illumination is projected onto specific fibers in the image guide separate from the detection fibers. This significantly shrinks the lateral separation of the illumination from the detection fibers and allows better distribution of illumination from the probe. While this improvement is currently being constructed, we are also working on alternative optical pathways, such as projecting illumination onto the probe image guide at an angle or separate coaxial illumination fibers polished at an angle in the probe.

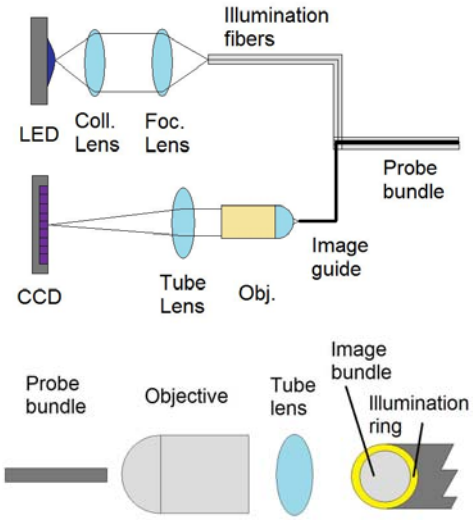

Figure 6: (Top) a schematic of the original optical pathway; (Bottom) the new illumination scheme projects an image of the old probe bundle onto the tip of another image guide, which serves as the new probe bundle; the old probe bundle, which no longer the probe, can be larger in size and of any geometry we need.

Software

A more detailed overview of the software component of Project 1 is described in the Year 1 report. Figure 7 shows two diagrams of the basic and advanced tasks we are undertaking and planning to undertake as part of this effort. The first task in software development is the adaption of the Hough transform to an algorithm that can mark the location of cells in an image so that subsequent processing and analysis by either the watershed algorithm or the optimal path problem can be performed. Before the Hough transform can even be applied, it is necessary to extract the cell boundaries from an image. The initial investigation showed that through pre-processing, the intensity of boundaries in the image can be greatly increased. This leads to the possibility of an adaptive local thresholding algorithm, which was used successfully in the initial testing to pick out most likely cell centers from the parameter space of the Hough transform. This method is more powerful for overcoming noise in an image, the source of difficulty with identifying the cell boundaries in our first attempt. Reducing the noise in the cell boundary plot significantly improves the chance of a successful Hough transform.

After modifications in the preprocessing have been made, the Hough transform itself will be modified and developed. One of the assumptions in the initial test was circular cells. Although cells in culture are often round, normal cells in tissue are generally not. This is especially true for epithelial cells in highly hierarchical tissue, where they are often flattened ovals with pinching ends. A new parameter space will be developed that more accurately parameterizes cells in the human breast. To properly design the new parameter space, images of different normal

human breast cells and cancerous cells will be studied. The most common features will be used to design a new parameter space for the Hough transform.

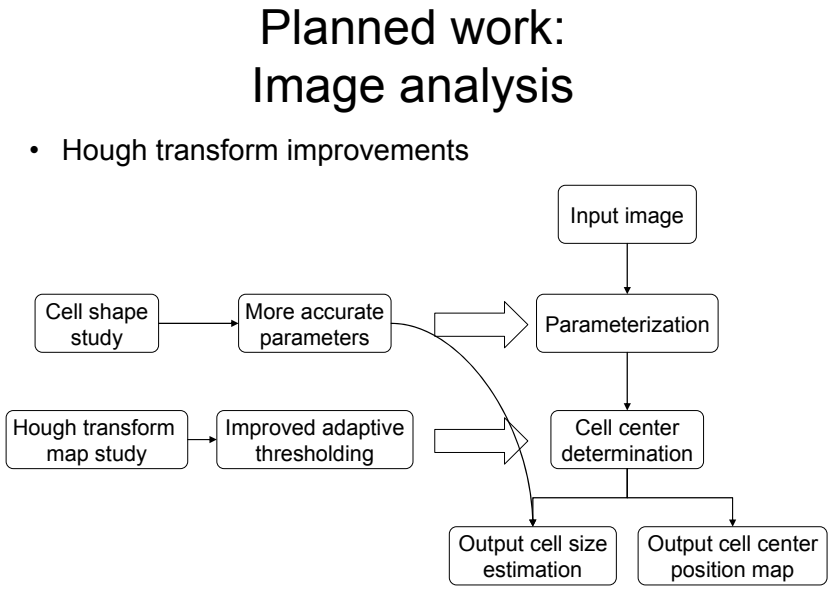

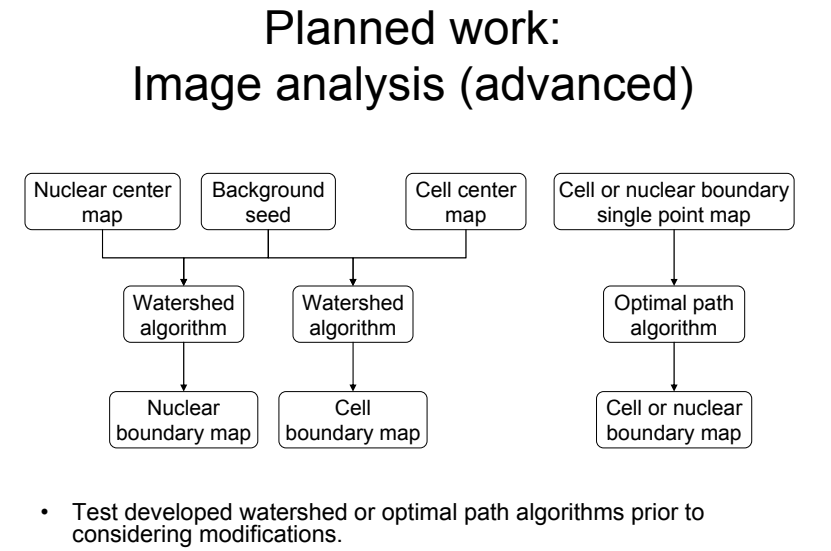

Figure 7: (Top) flow diagram for improving the Hough transform algorithm; (Bottom) flow diagram for applying watershed algorithm and optimal path algorithm to cell boundary detection.

The previous proposed investigations are some of the ways in which the preprocessing and Hough transform can be improved. After the Hough transform algorithm has been satisfactorily developed, work on either the watershed method or the optimal path problem will commence.

Because these are relatively complex image analysis methods, it is not efficient to simultaneously develop both of them. If the Hough transform demonstrates the ability to correctly locate the vast majority of cells, development of the watershed algorithm will be pursued. If the Hough transform can accurately detect only a limited number of cells, the optimal path problem method will be pursued. Because a branch point exists in the software development after the Hough transform, it is better to concentrate full effort on the investigations proposed in the preceding paragraphs and fully develop the algorithms before the branch.

Summary to Date: *Project 1 seeks to develop a new tool for breast cancer imaging and monitoring applications. This is a sub-mm probe which provides micron resolution imaging (expected to be ~4 microns after full optimization) in vivo without tissue removal. To the best of our knowledge, it is unlike any tool available for breast cancer imaging today offering resolution far exceeding what would be possible by other imaging techniques not requiring removal of tissue from the body. It is also extremely inexpensive using a $300 camera and light sources based on LEDs that cost under $50. The instrumentation design is being modified to provide optimal image quality when used in conjunction with the molecular imaging agents being developed in Projects 2 and 3. The instrument will be capable of imaging both intrinsic (cellular morphology and tissue architecture) optical signals and extrinsic contrast agents used either to facilitate visualization of nuclear morphology or to highlight molecular markers of breast cancer. We are on schedule with this project having completed the vast majority of Task 1 and Task 2 and initiated Task 3. We expect to request a SOW modification to allow further clinical evaluation of the device than originally proposed.*

Projects 2 and 3: Novel Nanoparticle-Based Imaging Probes for Breast Cancer Imaging Applications (Project 2) and for Monitoring Radiation Dose (Project 3)

We have merged the discussion of Projects 2 and 3 in this report as these two projects together encompass the two imaging agent components of the work. Projects 2 and 3 overlap in that work carried out in the first two tasks of Project 2 is also needed for Project 3. Both the imaging applications in Task 3 of Project 2 and all of the monitoring applications in Project 3, first require synthesis of appropriate nanoparticles. We describe the synthesis of these agents below and label each section to clarify whether the probes described are relevant to Projects 2, 3, or both. We also provide data from imaging (Project 2) and monitoring (Project 3) applications. We are developing two types of materials: (1) non-cadmium luminescent dots and (2) shaped and layered gold nanoparticles. The luminescent nanoparticle development work (Task 1, Months 1-12) was described in our Year 1 report. A Word copy of a submitted paper on that work was included at that time. This paper has now been published in Current Nanoscience (Sun et al, 2009) and the pdf is included in this year's Appendix and is not further discussed here. Multiple papers have appeared on the AuNP work described in the section which follows. Please refer to the Appendix section for copies of these papers. We concentrate our descriptions below only on those portions the work not yet published in final form.

Gold Nanoparticle Imaging Agent Development (Task 2 of Project 2 to Generate Materials for Use in Both Project 2, Task 3, and Project 3, All Tasks)

Project 2 focuses on synthesis of new forms of gold-based nanoparticles (AuNPs) generating the near infrared (NIR) optical properties needed for applications in Project 2 and Project 3 through shaping (non-spherical, rod-like structures) or layering (gold-silica-gold nanoparticles). The motivation for work with gold-based nanomaterials is that these materials are the nanomaterials closest to clinical translation largely because they are consider the most suitable for human *in vivo* use from a safety standpoint. Most gold-based biomedical nanomaterial work has used either conventional nanoshell (gold-silica) or gold colloid. Gold colloid cannot be tuned into the NIR and gold-silica nanoshells are too large for effective delivery for some of the types of applications we envision. Thus, in this project, we expanded our efforts to consider newer types of nanomaterials including gold nanorods expanding on previous research using these nanomaterials in particular by developing approaches which allow scale up to the volumes required for clinical use.

To facilitate future applications, it is necessary to synthesize complex gold nanorods with high yield and without secondary separation steps to remove spherical or triangular contaminants. As we noted in our report last year, such synthesis is particularly challenging for long nanorods. We are particularly interested in these longer nanorods as these are the rods which provide the NIR properties which place them in the NIR "water window" suitable for *in vivo* biomedical applications. Last year we were ahead of schedule on Project 2 so had proceeded with the synthesis which we described in last year's project report.

At the time of last year's report we had not proceeded to bioconjugation strategies. These strategies are required since we are fabricating these materials for ultimate use as molecular imaging agents for HER2, EGFR, and potentially other markers. The image below (Figure 8) shows our first images from a newly proposed method for attaching antibodies to nanorods. The image in the upper left shows successful labeling of HER2+ cells. Please see (Rostro-Kohanloo et al, 2009 (in press)) included in the Appendix for technical details of this approach. As opposed to what we reported last year (nanorods in CTAB), here were use a PEGylation based stabilization approach and heterobifunctional linkers with free carboxyl groups for the antibody attachment As we moved into the last three years of the overall project, Project 1 and Project 2 will begin to come together as we apply the agents being developed in Project 2 for use with the imaging system developed in Project 1.

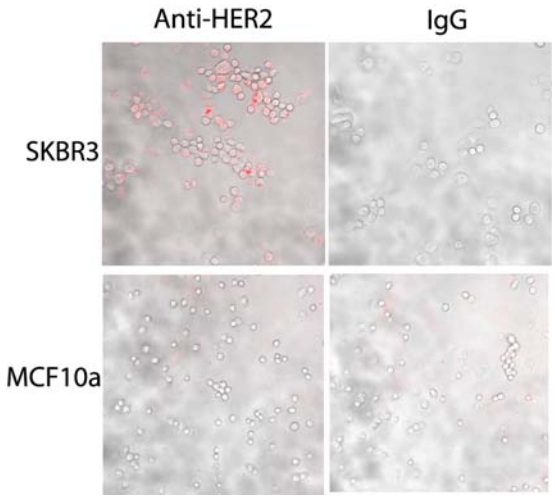

Figure 8. Nanorod conjugate targeting. Phase contrast shows the cell locations in grayscale, and two photon luminescence is displayed in red. Binding was only observed for the anti-HER2 conjugates and SKBR3 breast carcinoma cells.

As an alternative to the shaping approach considered last year, we are also investigating using a more sophisticated layering approach involving three of more layers of alternating metal and dielectric materials. The reason to consider this alternative over the shaping described above is stability. Any problem with the surface modification when working with nanorods will cause the nanorods to revert to a spherical configuration and lose their NIR properties. The method described above seems to produce by far the most stable nanorods we have developed to date. However, stability is always a hurdle when working with elongated nanoparticles. Agents inherently designed to have NIR properties while spherical will avoid this problem. An *Optics Express* paper we published in November (Hu et al, 2008) provides details on the new approach to developing tunable gold nanoparticles (NPs) for imaging (and if desired, integrated) therapy applications creating additional tunability in smaller diameter particles by addition of a small gold core into a silica-gold nanostructure (Figure 9). This approach overcomes several of the technical limitations we have encountered in our work using gold-silica nanoshells. The new gold-silica-gold NPs (1) maintain the near infrared (NIR) tunability of gold-silica NPs but will reduce the overall NP size to <100 nm to overcome delivery hurdles we have encountered with larger NPs; (2) feature narrower spectral line-widths to facilitate multiplexed labeling of molecular markers; (3) demonstrate increased extinction efficiency. The particles are formed beginning with easily synthesized gold colloid and then adding a thin silica layer followed by a final gold layer.

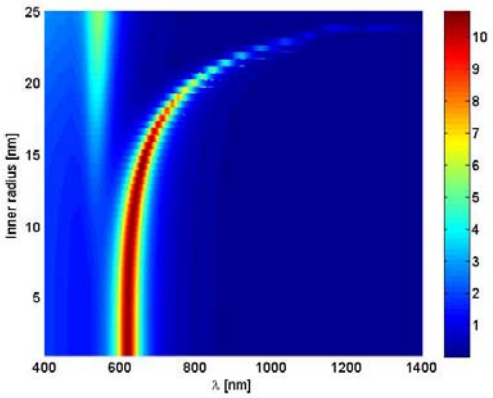

Figure 9. Extinction of *70* nm diameter multi-layer nanoshells in water as a function of inner radius.

.

Please see (Hu et al, 2008) in the Appendix for a paper describing the optical properties of gold-silica-gold materials. We do not describe the technical details of that work here as the paper covers these aspects. We have begun efforts on synthesis of these particles and describe those here. This work is not yet published and further efforts are required to bring the sizes down to a level where will we gain the advantages we seek with this class of materials. A multi-step procedure is performed to prepare gold-silica-gold nanoshells, composed of the following stages: (1) making gold colloid (15-100 nm), (2) silica coating of gold particles, (3) (3-aminopropyl)trimethoxysilane (APS) functionalization of gold-silica particles, (4) synthesis of THPC (tetrakis hydroxymethyl phosphonium chloride) gold solution composed of 1-2 nm gold colloids, and (5) finally synthesizing the complete gold-silica-gold nanoshells.

In this work, gold colloid (15-100 nm) was prepared by a standard sodium citrate reduction method. 0.86 ml of chloroauric acid solution was added to 98 ml of de-ionized water in a clean 250 ml glass flask with a stir bar, and the solution was brought to boiling temperature upon stirring. Subsequently, trisodium citrate solution was added to produce gold colloid. Particular sizes are created based on varying the amount of trisodium citrate. Upon addition of the trisodium citrate, the color of the solution changed to blue and then to red.

The preparation of the silica-coated gold nanoparticles involved priming citrate-terminated gold colloids with (3-aminopropyl)trimethoxysilane, followed by the addition of active silica to form a thin layer of silica on the gold surface. Extended growth was achieved by the Stöber method, in which silica coated gold nanoparticles were functionalized with tetraethyl orthosilicate and ammonia in ethanol. Other research groups have followed a direct coating method of citrate-stabilized gold nanoparticles with silica shells by reducing tetraethyl orthosilicate in ammonium hydroxide with isopropyl alcohol or ethanol. We are instead direct coating on

citrate-stabilized gold nanoparticles with silica shells – producing thickness from 20 nm to 150 nm – by optimizing the pH of the solution via ammonium hydroxide with isopropyl alcohol, and comparably by optimizing the amount of tetraethyl orthosilicate and ammonium hydroxide. This method does not require any coupling molecules and is based on a method that our group has been using for the preparation of various thicknesses of silica particles on various radii of gold particles: 50nm (Figure 10a-1c), and 20 nm (Figure 10d). A suitable amount of 3-aminopropyl)trimethoxysilane (1 mM) from 300 – 500 µl was added to silica-coated gold nanoparticles that were vigorously stirred in ethanol solution. The mixture is allowed to react for 12 hours. To enhance covalent bonding of the 3-aminopropyl) trimethoxysilane groups to the silica shell surface, the solution was gently refluxed for one hour. The APS functionalized gold-silica nanoparticles were then collected in ethanol. A THPC gold solution composed of 1-2 nm gold colloids was prepared according to the method of Duff and Baiker. Under rapid stirring, 1.2 mL of 1 M NaOH was added to 180 mL of water, followed by the addition of 4 ml of 1.2 mM aqueous THPC solution. After 5 minutes of continuous stirring, 6.75 ml of 1 wt% aqueous chloroauric acid was added in one quick motion, after which the solution immediately turned to a medium brown color. The final solution was refrigerated for at least 2 weeks before use.

A solution containing reducible gold salt was prepared in order to grow a continuous gold layer on the gold-primed silica-coated nanoparticles. Briefly, 50 mg of potassium carbonate was dissolved in water followed by the addition of 3 ml of 1.0% wt of THPC gold solution. Gold-silica-gold nanoshells were then grown by reacting gold salt with the gold-silica-gold colloids (1-2 nm) in the presence of formaldehyde. Currently, we are focused on reducing the overall size of the nanoshells made using this approach to less than 100 nm for Project 2 and Project 3 applications. Nanoshell formation was visualized and assessed with a transmission electron microscope (TEM). We expect to be able to report fully on this new class of gold nanostructures next year.

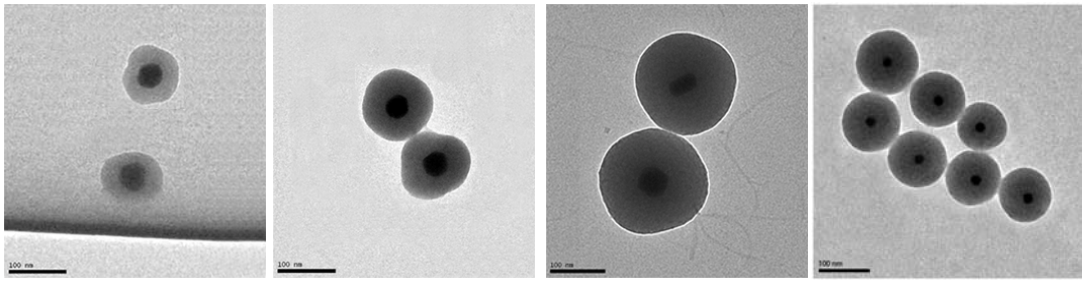

Figure 10. TEM images of silica gold (50 nm) nanoparticles with overall sizes of (a) 104 nm, (b) 125 nm, (c) 180 nm (left to right). (d) TEM image using a 20 nm gold nanoparticle as the starting point (far right).

Biological Evaluation (Relevant to Both Projects 2 and Project 3)

Last year we reported imaging results using darkfield microscopy for imaging. Although this method provides a facile approach to imaging cells in a laboratory setting, it is not relevant to the clinical imaging applications we are ultimately heading towards. In those applications where we will ultimately be imaging intact tissue (for example, using the needle probe device being built in Project 1), we detect reflected not transmitted optical signals. We will also ultimately be detecting reflected not transmitted optical signals in the radiation dose monitoring described in Project 3. Thus, it is important to consider how our nanomaterials perform in a reflectance-based geometry. In the work described here (paper on this work to be included in next year's progress report), we use NIR reflectance confocal microscopy. Future experiments will use the imaging system developed in Project 1.

Three breast cancer cell lines that are known to overexpress different levels of HER2 receptors were imaged: SK-BR-3, HCC1419, and JIMT-1. The normal mammary epithelial cell line, MCF10A, was also analyzed as a control that does not overexpress the HER2 antigen. All cell lines were purchased from the American Type Culture Collection with the exception of the JIMT-1 cell line, which was purchased from DSMZ (Germany). The SK-BR-3, HCC1419, and JIMT-1 cell lines were grown with medium (McCoy's 5A, RPMI-1640, and Dulbecco's Modified Essential Medium, respectively) supplemented with 10% fetal bovine serum (FBS) and 1% penicillin-streptomycin. The MCF10A cells were cultured in Mammary Epithelial Basal Medium (MEBM) supplemented with a BulletKit (Clonetics). The cells were maintained at 37ºC in 5% CO_2 atmosphere.

Each cell line was grown to confluency, trypsinized and then counted using a hemocytometer. The cells were then incubated with either media alone, PE anti-human CD340 (erbB2/HER-2) antibody (BioLegend), or PE mouse IgG1 isotype control antibody (BioLegend) for 30 minutes on ice in the dark. The cells were then washed, resuspended in 500 µl of cell staining buffer (BioLegend), and stored on ice until they were analyzed at The University of Texas M.D. Anderson Cancer Center (MDACC) flow cytometry core for the immunofluorescence intensity of HER2 expression levels. In order to determine the mean immunofluorescence intensity for each cell line, we used a commercially available kit including PE Anti-Human CD340 (erbB2/HER-2) Antibody, cell staining buffer, and a PE Mouse IgG1 Isotype Control (BioLegend) for background signal correction. The immunofluorescence intensity was converted into antigen binding capacity using the Quantum Simply Cellular anti-Mouse IgG kit (Bangs Laboratories, Inc.). This kit utilizes four different samples of microbeads with a predetermined number of antigen binding sites which correlates with respective immunofluorescence intensity. A linear scale is then generated and used for the interpretation of antigen binding sites on cell samples of known intensity.

Nanoshells were fabricated using previous published procedures. Briefly, silica cores were generated using the Stöber method and surfaces were terminated with amine groups. The final silica particles were measured by scanning electron microscopy (SEM) to obtain the average

diameter of 276 nm. Gold colloid of 1-3 nm in diameter was then prepared and adsorbed onto the silica cores through the amine groups (nanoshell 'seeds'). The gold shell overlay was completed by mixing the nanoshell seeds with additional gold solution, potassium carbonate and formaldehyde. A UV-vis spectrophotometer (Varian Cary 300) was used to analyze the spectrum of the completed nanoshells. Mie Theory was then used to derive the absorption, scattering, and extinction coefficients and, subsequently, the concentration of nanoshells in solution. As confirmed by SEM, the nanoshells had an average diameter of 350 nm, a peak surface plasmon resonance at 840 nm and a concentration of approximately 2.3×10^9 particles/mL.

To create molecularly-targeted particles, the nanoshell surfaces were first modified by the addition of either specific or non-specific antibodies (anti-HER2/neu or anti-IgG, respectively) as previously described by Loo et al. A custom made heterobifunctionalized polyethylene glycol linker, orthopyridyl-disulfide-PEG-N-hydroxysuccinimide ester (OPSS-PEG-NHS, MW = 2kD, CreativeBiochem Laboratories), was incubated with either anti-HER2 antibodies (C-erbB-2/HER-2/*neu* Ab-4, Lab Vision Corporation) or anti-rabbit-IgG (Sigma Aldrich) at a molar ratio of 3:1 in sodium bicarbonate (100 mM, pH 8.5) overnight on ice and under refrigeration. All aliquots were then stored at -80ºC. The linker permits conjugation to the antibodies via amide linkages (NHS) and conjugation to the nanoshell gold surfaces via sulfur groups (OPSS).

In order to perform biological studies, the nanoshells (2.3×10^9 particles/mL) were incubated with the prepared anti-HER2-linker or anti-IgG-liker solution for 1 hour under refrigeration and further stabilized by incubation with a 10 mM polyethylene glycol-thiol solution (PEG-SH, MW = 5kD, Nektar) overnight under refrigeration. Nanoshells were then centrifuged to remove unbound antibodies and resuspended in water. Prior to experimental studies, the nanoshells were brought to room temperature and a solution of bovine serum albumin (BSA) and phosphate-buffered saline (PBS) was added at a final concentration of 1% each. Samples were vortexed briefly before use.

Approximately $6x10^5$ cells of each cell line (MCF10A, SK-BR-3, HCC1419, and JIMT-1) were isolated, washed and incubated with a 2 ml solution of either PBS alone, anti-HER2 targeted nanoshells ($2x10^9$ particles), or anti-IgG targeted nanoshells ($2x10^9$ particles). The nanoshell-cell suspensions and controls were then incubated in a hybridization chamber (VWR International) at 37ºC and 7 rpm for 15 minutes. After incubation, the suspensions were centrifuged and rinsed two times with PBS to remove unbound nanoshells. The cell pellets were resuspended in 60 µL of the appropriate cell media. This solution was then aliquoted onto a glass slide fitted with a 0.12 mm deep spacer (Invitrogen) and then coverslipped. Images of the different cell types were obtained with a Lucid VivaScope 2500 inverted confocal microscope, which employs an incident wavelength of 830 nm. The Lucid VivaScope 2500 is a portable, FDA approved system used to assess freshly excised tissue in clinics. Images were taken at the same distance from the glass surface for each condition and at a power of 1.4 mW.

The optical intensity of the reflectance of the cells was measured using ImageJ processing software. An image of pure black was designated with a value of 0 and that of pure white with a value of 255. Average intensity values for each cell line under each condition were calculated from 7 independent areas of the respective glass slide used for imaging. Images used for this component of the study contained areas where no cells were present; therefore, although the intensity of individual cells incubated with HER2-targeted nanoshells approach 255 (data not shown), this was not possible for widespread images due to the diluted sample allowing certain areas to be void of cells. Sample normality was assessed to evaluate the error distribution for all data points. A normal probability plot of the residuals verified that the samples followed a normal distribution (data not shown). F-tests were also used to determine the equality of variance before applying two-tailed paired Student's t-tests to evaluate significance in the difference in reflectance intensity of cells between two treatment conditions.

The goal of this study was to determine if gold nanoshells conjugated to anti-HER2 antibodies could optically enhance the identification of breast cancer cells that overexpress HER2 receptors. Therefore, three breast cancer cell lines (HCC1419, SK-BR-3, and JIMT-1) that are known to overexpress HER2 and a normal mammary epithelial cell line (MCF10A) were chosen to optimize the binding conditions and evaluate specificity of targeted nanoshells. Using flow cytometry, the calculated number of HER2-antigen binding sites, along with the 95% confidence interval for each cell line, was determined. Specifically, the breast cancer cell lines were found to have significantly higher (17 to 77 times more) binding sites than the normal breast epithelial cells (MCF10A).

The capacity of the nanoshells to optically image the breast cancer cell lines were then visualized using a Lucid VivoScope reflectance confocal microscope, a portable reflectance imaging system that is currently used in clinics. Since the nanoshells are made with a gold shell and have an optical peak resonance at 840 nm, the cells that are bound with the nanoshells clearly reflected more light using reflective confocal microscopy than the cells that are not bound to nanoshells. Qualitatively, the reflective confocal microscopy images in Figure 11 demonstrate that the nanoshells conjugated to anti-HER2 antibody bound the most to the three breast cancer cell lines. Most of the cell surface could be visualized. The labeling of the cancer cells was very specific against the HER2 receptor since the nanoshells conjugated with non-specific IgG resulted in only punctate labeling of the same cells. Similarly, only punctate labeling of MCF10A normal epithelial cells was imaged by the nanoshells conjugated with anti-HER2 antibody. This low level of reflectance is likely due the presence of the low level of HER2 receptors present on MCF10A cells.

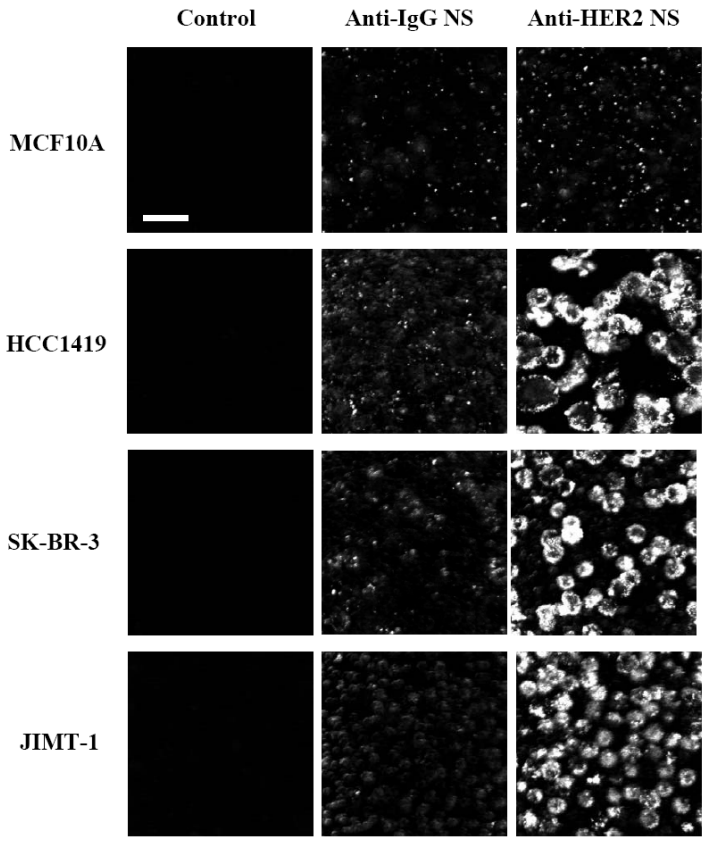

Figure 11. The right hand column shows NIR reflectance confocal imaging using targeted gold nanoparticles. Of particular interest are the 2nd and 4th rows here. These cells are herceptin resistant yet clearly we still able to achieve strong targeting. This is intriguing because these same gold nanoparticles can be used for direct photothermal ablation of cells suggesting a novel approach to treatment of HER2+, Herceptin resistant women.

Quantitatively (Figure 12), the reflectance intensity from each breast cancer cell line with HER2 overexpression that was treated with nanoshells conjugated with anti-HER2 antibody was 5 times higher than the reflectance from normal human breast epithelial cells (MCF10A) treated with the same nanoshells ($P<0.001$). For each cell line, the binding of nanoshells appeared to be dependent upon the anti-HER2 antibody because the reflectance intensity of the cells was 3 to 5 fold higher when the cells were treated with nanoshells conjugated to anti-HER2 antibody than to non-specific IgG ($P<0.001$). There was no difference in reflectance intensity between any cell type incubated with only PBS (the control condition) ($P>0.1$) or with IgG-targeted nanoshells ($P>0.1$).

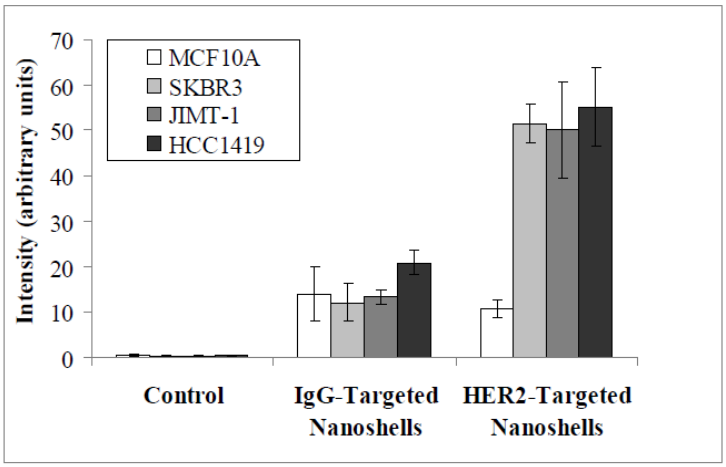

Figure 12. Quantification of imaging results.

The results obtained with RCM provide a first step towards developing these particles for the types of imaging applications we anticipate; the critical results will be those we obtain using the imaging system under construction in Project 1. We are also collaborating to investigate highly exploratory new techniques (photothermal imaging) which would dramatically increase the optical contrast achievable with gold nanoparticle based imaging agents so that the optical imaging performed will be sensitive to much lower levels of expression than what is needed using conventional approaches. A paper (Hleb et al, 2008) provides details on this work.

Summary to Date: *Project 2 remains ahead of schedule. As proposed, the first two years were a basic science chemistry directed effort to create synthesis and bioconjugation strategies for the biological experiments proposed in the latter years of the projects. We have initiated imaging studies and look forward to integrating the agents being developed in this project with the imaging system developed in Project 1. We expect to submit a revised SOW request and appropriate regulatory paperwork to enable an accelerated and more ambitious set of imaging experiments to be performed. An unexpected result which may open up new avenues of work was the high level of nanoparticle targeting we were able to achieve using herceptin resistant cell lines including a line where we would have anticipated MUC interference. Because our nanoparticles inherently have both imaging and therapeutic (photothermal ablation) properties, these results suggest a possible new approach to treatment of HER2+, herceptin resistant women. Depending how the rest of the project evolves, we may in the future request a SOW modification to pursue this possibility.*

Nanoparticle Probes to Monitor Radiation Dose (Project 3)

Project 3 is the smallest and most risk effort of the project we originally proposed. The idea underlying this project is to develop an optical approach for monitoring radiation which would provide more information than the bulk dose measurements which can be achieved today. Our MDACC coPI is a radiation oncologist by training and proposed this idea. Our work to date has

been focused on the very first step towards this approach: Can we use nanoparticles to generate a change in optical signal with radiation dose? Last year we presented data demonstrating that indeed we could employ a plasmonic nanoparticle-based approach to accomplish this idea (Task 1 of Project 3). Essentially, we monitor the perturbation in optical nanoparticle as nanoparticles are released from an area after exposure to radiation. We found we could do this at a radiation dose of 100 Gy, At this point, we had a choice to make. We could move on to Task 2 which provides a more desirable signal change to measure (Our strategy in Task 1 measures *loss* of optical signal after exposure to radiation while our strategy in Task 2 measures *gain* in signal after radiation. Signal-to-background issues are already much easier to handle if we start with a probe that is dark in its original configuration. However, if we moved to Task 2 directly we would be working at radiation levels we know are not consistent with what would make this a clinically viable technique for breast cancer. (The radiation doses we are seeking to measure clinically are far lower.). Thus, it is important to examine whether it is possible to bring down sensitivity levels further. The experiment shown in Figure 13 is at a dose 50% lower than the 100 Gy data included in last year's report. For this experiment, gold colloid is prepared by using the standard sodium citrate reduction method discussed previously. Chloroauric acid solution is added to deionized water and the solution is brought to boiling temperature upon stirring. Subsequently, trisodium citrate solution is added. The size of gold can be controlled based on the amount of trisodium citrate. Based on our radiation experiments to date, 50 Gy is the lowest radiation dose for which we can potentially detect the loss of signal we are looking for as an assay (Figure 12). Because it has been hard to make definitive quantitative statements regarding signal loss, we are exploring the use of AFM to help us in this aspect of the work.

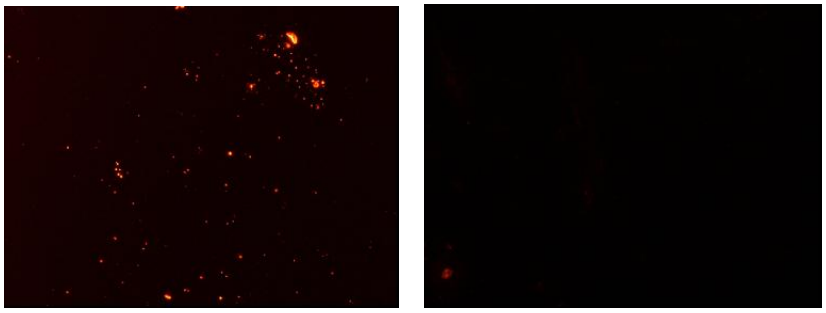

BEFORE RADIATION **AFTER 50 Gy RADIATION**

Figure 13. Gold nanoparticles (13 nm) after radiation treatment. We are seeking some level of loss of the bright spots shown in the image on the left (before treatment) after radiation. The radiation dose in these images is 50 Gy.

Summary to Date: *This project is the smallest and most high risk component of our proposal. Work to date on Project 3 has indicated that idea proposed (generating an optical signal which could be measured in response to radiation dose) is fundamentally sound. However, further improvements in sensitivity are required for optical monitoring of radiation dose to become a clinically viable approach.*

Key Research Accomplishments

- Development of a second generation needle-compatible fiber optic imaging system prototype for breast cancer applications. Unlike our first year design, this system is readily reconfigurable (modular illumination, detection, etc.) to provide flexibility as our design requirements evolve. The goal of this system is to provide an inexpensive method ($< 5K cost/instrument) for *in situ* tissue analysis with micron level resolution in a sub-mm package to provide optical biopsy without tissue removal. (Project 1)

- Demonstration of targeted molecular imaging using a novel gold nanorod bioconjugation method. These structures may be used for both the imaging experiments which comprise the last tasks in Project 2 and for the activatable radiation monitoring applications throughout Project 3. Nanorods are more attractive than conventional silica-gold nanoshells for some types of imaging/therapy applications due to smaller size and enhanced absorption. A heterobifunctional PEG with exposed carboxyl groups for antibody conjugation was used to generate surface modified nanorods for HER2 targeted imaging applications. Proof of principle cellular imaging results are reported. (Project 2/Project 3)

- As an alternative to shaping gold (gold nanorods), we have demonstrated both by simulation and now experimentally similar NIR tunability can be achieved through a new type of gold nanoshell (multilayered gold-silica-gold nanoshells). An *Optics Express* paper reports on the physics governing these particles' properties. Synthesis efforts are underway and it is expected these particles may be used in breast cancer imaging and radiation monitoring applications in Projects 2 and 3 in future years. (Project 2/3)

- As part of the biological characterization component of Project 2, we evaluated a number of cells lines including herceptin-resistant lines. We unexpectedly discovered targeted nanoshells bind to herceptin-resistant cell lines much more strongly than we would have anticipated for the line where one might expect MUC interference. This is possibly due to the high surface area/volume allowing large numbers of potential binding sites on the nanoparticle to be present and opens up intriguing new possibilities for the use of these types of particles as nanotheranostics for treatment of HER2+, herceptin resistant women (Project 2)

- Evaluated strategy for dose measurement during radiation treatment for breast cancer (Project 3)

- My proposal expressed a desire to build connections between my group with the breast centers at both MD Anderson Cancer Center and Baylor College of Medicine to create a

sustainable infrastructure for breast cancer research that will continue after the present grant ends. I attended the Baylor College of Medicine Breast Cancer Center Annual Retreat this year and gave a talk on my work resulting in a number of new collaborations. Based on these presentations, I was recently invited by the head of the center to become an adjunct faculty member which will facilitate my future involvement and provide access to all of Baylor's shared cores at internal prices.

Reportable Outcomes

Journal Articles Acknowledging DOD Era of Hope Scholar Support

- Sun, J., Fu, K., Zhu, MQ, Bickford, L., Post, E., and Drezek, R. "Near-infrared quantum dots for fluorescence tissue imaging" *Current Nanoscience*, 5 (2), 160-166 (2009). *(Last year this work was reported as submitted. It has now been accepted and published. A pdf of the published version is included.)*

- Hu, Y., Fleming, R., and Drezek, R. "Optical properties of gold-silica-gold multilayered nanoshells." *Optics Express.* Vol 16, 24, 19579 (2008).

- Hleb, E., Hu, Y., Drezek, R., Hafner, J., and Lapotko, D. "Photothermal bubbles as optical scattering probes for imaging live cells." *Nanomedicine.* 3(6), 797-812 (2008). (doi:10.2217/17435889.3.6.797)

- Rostro-Kohanloo, B., Bickford, L., Payne, C., Day, E., Anderson, L., Zhong, M., Zhong, Lee, S., Mayer, K., Zal, T., Adam, L., Dinney, C., Drezek, R., West, J., and Hafner, J. "Stabilization and Targeting of Surfactant-Synthesized Gold Nanorods." *Nanotechnology.* Accepted for publication in 2009 (*A copy of the accepted manuscript is included. Page proofs have not arrived yet.)*

- Bickford, L., Chang, J., Fu, K., Sun, J., Hu, Y., Gobin, A., Yu, TK, and Drezek, R. "Evaluation of Immunotargeted Gold Nanoshells as Rapid Diagnostic Imaging Agents for HER2+ Breast Cancers." *Nanobiotechnology*. 1551-1286 (Print) 1551-1294 (Online); DOI 10.1007/s12030-008-9010-4 (2008). *Became available online in 2008 and in print 2009.*

- Bickford, L., Sun, J., Fu, K., Lewinski, N., Nammalvar, V., Chang, J., Drezek, R. "Enhanced Multi-Spectral Imaging of Live Breast Cancer Cells Using Immunotargeted Gold Nanoshells and Two-Photon Excitation Microscopy." *Nanotechnology*. 19: 315102 (6pp) doi: 10.1088/0957-4484/19/31/315102 (2008). *Published June 24, 2008.*

Abstracts

- Bickford, L. and Drezek, R. Gold Nanoshells as Potential Real-Time Intraoperative Molecular Probes for HER2/NEU Overexpression Using Near-Infrared Reflectance Confocal Microscopy. Annual Houston Conference on Biomedical Engineering Research. Houston, TX. March 2009.

- Hu, Y., and Drezek, R. Angular scatter patterns from multi-layered gold nanoshells. Materials Research Society Spring Annual National Meeting. San Francisco, CA. April 2009.

- Sun, J., Fu, F., Zhu, M-Q., Bickford, L., Post, E., and Drezek, R. "PbS quantum dots for near-infrared fluorescence imaging." OSA 2008 Frontiers in Optics (FiO)/Laser Science XXIV Conference. Rochester, NY. October 19-23, 2008.

Invited Presentations

- Optical activatable nanoparticles for imaging and therapy of cancer. Department Seminar. Duke University Fitzpatrick Optics Institute 2008-2009 Seminar Series. Durham, NC. March 2009.

- Optical molecular imaging of breast cancer. Baylor College of Medicine Cancer Center Annual Retreat. Cleveland, TX. November 2008.

- Optical molecular imaging and therapy of breast cancer. Distinguished Speaker Seminar Series. Department of Pharmacology. University of Houston. April 2009.

- Optically activatable nanoparticles for imaging and therapy of cancer. Department Seminar. University of Rochester. Department of Biomedical Engineering. Rochester, NY. November 2008.

- Translational research in optical molecular imaging of breast cancer. Rice University Something New for Lunch Lecture Series. Houston, TX. October 2008.

- Invited talked "Advances in Nanobiophotonics" IEEE LEOS Summer Topical Conference. July 2008.

Employment

- The PI was promoted to Professor of Biomedical Engineering in large part because of results obtained through this research project.

- The PI has been invited to become Adjunct Faculty at Baylor College of Medicine because of the breast cancer collaborations initiated as part of this research

CONCLUSIONS

Our research team, comprised of my group at Rice and MDACC collaborators, is focusing the majority of its Era of Hope research efforts specifically in areas of breast cancer care where the combination of ***miniaturized optical devices*** and ***molecular-specific imaging agents*** offer the potential to address current gaps in care. There are two primary areas where I believe our technologies can make the biggest difference: ***early detection*** and ***monitoring therapy*****.** Optical spectroscopy, implemented through small fiber optics, can provide clinically valuable information ranging from cellular metabolic status (via endogenous fluorescence) to nuclear size (correlated to optical scatter) to quantitative measurements of molecular markers (through targeted imaging agents under development in our lab). Most of our effort has focused on development of needle-compatible spectroscopic and direct imaging probes for breast cancer applications. The technology is being designed for clinical applications for which it is valuable to have a local high resolution imaging method to complement a more macroscopic imaging modality (for example, during ultrasound guided breast biopsy). Progressive design and evaluation of these needle-based technologies is **Project 1** of our DOD project. In addition to technology efforts funded by CDMRP, we have also been able to initiate other new translational breast imaging projects since moving into the breast cancer field after receipt of an EOHS award. For instance, we are developing a wide-field spectral imaging device to monitor response to treatment of inflammatory breast cancer patients. To complement our imaging technology development projects, the second primary effort underway is development of molecular-specific optical imaging probes (**Projects 2/3**). Many similar probes developed to date have been suitable for lab-based but not clinical work. A challenge of most NP-based molecular contrast methods has been that conventional imaging protocols require incubation periods of over one hour. This is not clinically viable for either for our diagnostic or monitoring applications. During Year 1, we developed protocols for imaging of HER2 which preserves ~90% of optical contrast at 10 minutes. The fast imaging times we have been able to achieve open up the possibility of another type of breast cancer monitoring application: tumor margins assessment. Especially in community hospital settings, there is a critical need for new technologies for rapid intraoperative margins assessment. To be viable, a complete procedure must be accomplished in under 15-20 minutes. Much of the work already underway in **Project 2** is directly applicable to tumor margins assessment and we expect to request several modifications to the SOW during Year 3 to allow us to pursue more focused biological evaluation than initially proposed (adding in tissue protocols to future years) incorporating tumor margin applications into our effort. In summary, our EOHS award is guided by a philosophy of developing practical, low cost technologies which can be moved quickly into clinical testing so that we can most effectively understand the potential and limitations of these new approaches to optical imaging of breast cancer and optimally direct our efforts to maximize impact on detection and treatment.

References

Bickford, L., Chang, J., Fu, K., Sun, J., Hu, Y., Gobin, A., Yu, TK, and Drezek, R. "Evaluation of Immunotargeted Gold Nanoshells as Rapid Diagnostic Imaging Agents for HER2+ Breast Cancers." *Nanobiotechnology*. 1551-1286 (Print) 1551-1294 (Online); DOI 10.1007/s12030-008-9010-4 (2008).

Bickford, L., Sun, J., Fu, K., Lewinski, N., Nammalvar, V., Chang, J., Drezek, R. "Enhanced Multi-Spectral Imaging of Live Breast Cancer Cells Using Immunotargeted Gold Nanoshells and Two-Photon Excitation Microscopy." *Nanotechnology*. 19: 315102 (6pp) doi: 10.1088/0957-4484/19/31/315102 (2008).

Hleb, E., Hu, Y., Drezek, R., Hafner, J., and Lapotko, D. "Photothermal bubbles as optical scattering probes for imaging live cells." *Nanomedicine.* 3(6), 797-812 (2008). (doi:10.2217/17435889.3.6.797)

Hu, Y., Fleming, R., and Drezek, R. "Optical properties of gold-silica-gold multilayered nanoshells." *Optics Express.* Vol 16, 24, 19579 (2008).

Rostro-Kohanloo, B., Bickford, L., Payne, C., Day, E., Anderson, L., Zhong, M., Zhong, Lee, S., Mayer, K., Zal, T., Adam, L., Dinney, C., Drezek, R., West, J., and Hafner, J. "Stabilization and Targeting of Surfactant-Synthesized Gold Nanorods." *Nanotechnology.*

Sun, J., Fu, K., Zhu, MQ, Bickford, L., Post, E., and Drezek, R. "Near-infrared quantum dots for fluorescence tissue imaging" *Current Nanoscience*, 5 (2), 160-166 (2009).

Near-Infrared Quantum Dot Contrast Agents for Fluorescence Tissue Imaging: A Phantom Study

Jiantang Sun[1, 3], Kun Fu[2, 3], Ming-Qiang Zhu[1], Lissett Bickford[1], Eric Post[4] and Rebekah Drezek[1, 2, *]

[1]*Departments of Bioengineering,* [2]*Electrical and Computer Engineering and* [3]*Rice Quantum Institute, Rice University, 6100 Main Street, Houston, TX 77005, USA;* [4]*Biomedical Engineering, Louisiana Tech University, 818 Nelson Avenue, Ruston, LA 71270, USA*

Abstract: Due to their small size and red-shifted excitation and emission bands, lead sulfide (PbS) near-infrared (NIR) quantum dots (QDs) are potentially promising optical contrast agents for *in vivo* tumor imaging applications. In this phantom-based study, we correlated PbS NIR QD concentrations to feasible imaging depths. A fluorescence imaging system (FIS) was used to acquire images of QD-filled tumor models, which were embedded in liquid tissue phantoms. For the lowest tested concentration of 200 nM, PbS-QD-filled tumor models could be imaged at a tissue phantom depth of 15 mm. Additionally, the FIS was used to compare the imaging potential of PbS QDs to quantum dots that fluoresce in the visible spectral range. Results indicated that tumor models with photons emitted in the NIR region can be imaged with less distortion than those with photons emitted in the visible spectrum. As the phantom thickness over the tumors was increased from 0 to 1.75 mm, the half-intensity widths of normalized fluorescence images produced by red QDs (acquired peak at ~645 nm) increased by ~300%; for NIR QDs (acquired peak at ~880 nm), the widths increased by ~140%. Due to the decreased scattering effect of the tissue phantoms in the NIR spectral range, the margins of PbS QD images were better defined than those of the corresponding red images.

Key Words: Near-infrared, quantum dot, fluorescence, optical imaging, phantom.

1. INTRODUCTION

A "therapeutic window" exists in the spectral region of 700 to 1200 nm which allows near-infrared (NIR) light to penetrate several centimeters into human tissue [1-4]. Recently, the development of various NIR fluorescence contrast agents has promoted the application of NIR fluorescence biomedical imaging techniques [4-8]. Among those strategies employing fluorescence contrast agents, the use of lead sulfide (PbS) NIR quantum dots (QDs) is expected to yield promising results for *in vivo* imaging applications. PbS QDs are nanometer-sized, core-shell semiconductor structures that possess a strong emission peak in the NIR region [6, 9, 10]. With specific surface-modification, the water solubility and biocompatibility of PbS QDs can be greatly enhanced [11]. Since the emission peak of these quantum dots can be easily tuned to the desired wavelength by tailoring the particle size, PbS QDs can provide great emission band flexibility for *in vivo* NIR tissue imaging applications [5, 6, 9, 11, 12].

Since the introduction of quantum dots in the late 1970s, numerous reports have been published that examine the use of these nanoparticles as fluorescence imaging contrast agents [6, 10, 12-15]. Compared to quantum dots that fluoresce in the visible spectral range, PbS NIR QDs have their own unique properties for *in vivo* deep tissue fluorescence imaging applications [2, 6, 9, 10, 16]. As reported in previous publications, for PbS QDs that have an emission peak at ~1010 nm, the average particle size is ~4 to 5 nm before surface modification; after surface modification, particles show no significant increase in size when observed by transmission electron microscopy (TEM) [9]. Therefore, it is believed that the relatively small size of PbS QDs will facilitate body clearance of these particles during clinical trials [17]. Moreover, the corresponding excitation spectrum of these QDs spans the range from visible to NIR [9, 11-12] and the emission peak of PbS QDs can be systematically tuned in the NIR spectral range. Thus, both the wide excitation band and the red-shifted emission peak provide flexibility in the choice of proper working wavelength regions; this will, in turn, avoid most of the effects of tissue autofluorescence [18, 19].

A bandpass excitation filter of 671 to 705 nm was selected for the depth-resolved tissue phantom experiments discussed below. This range avoids the major absorption peaks of intrinsic autofluorophores, and therefore permits improved illumination into the samples [18-21]. In this experiment, the fluorescence spectrum of the excited PbS QDs peaks at a wavelength of ~880 nm when acquired with a Maestro imaging system (CRi, Woburn, MA). Under these conditions, the NIR quantum dot signal can be easily distinguished from tissue autofluorescence background [18] and images with improved contrast can then be obtained. Furthermore, in comparison with visible QDs, the minimum absorption and scattering coefficients of tissue samples in the NIR region allow photons emitted from PbS QDs to propagate deeper into tissue [1, 2]. Images of PbS-QD-filled tumor models embedded in tissue phantoms also exhibit minimal blurring at tumor margins due to the reduced scattering effect.

We have previously shown the possibility of using bioconjugated PbS QDs as NIR contrast agents for targeted molecular imaging applications [22]. As a step towards *in vivo* tissue fluorescence screening using PbS NIR quantum dots and the Maestro imaging system, a tissue phantom study was carried out to identify and evaluate the imaging potential of these NIR nanocrystals and to acquire a basic understanding of the contrast agent concentrations required to obtain clear and acceptable images. Additionally, the imaging advantages of NIR QDs have been compared with QDs that fluoresce in the visible spectral range.

2. METHODS

2.1. NIR Quantum Dot Fabrication and Surface Modification

The lead sulfide NIR QDs used in this study were synthesized [9, 11, 12] and surface modified in accordance with methods presented in previous publications [6, 10, 11]. The NIR fluorescence peak of these PbS quantum dots can be tailored to the desired imaging wavelength range and optimized for the imaging system employed [9, 11].

2.2. Tissue Phantom and Tumor Models

Human tissue is a highly turbid media with strong absorption and scattering effects in the ultraviolet (UV) and visible spectral regions [1, 18, 23]. However, it is within the NIR wavelength region of 700 to 1200 nm where most biomolecular absorption coefficients reach their minimum values [1, 2, 5, 18, 24]. To study light propagation and distribution in human tissue, various phantoms have previously been developed that simulate tissue optical proper-

*Address correspondence to this author at the Department of Bioengineering, Rice University, 6100 Main Street, Houston, TX 77005, USA; Tel: (713) 348-3011; Fax: (713) 348-5877; E-mail: drezek@rice.edu

1573-4137/09 $55.00+.00 © 2009 Bentham Science Publishers Ltd.

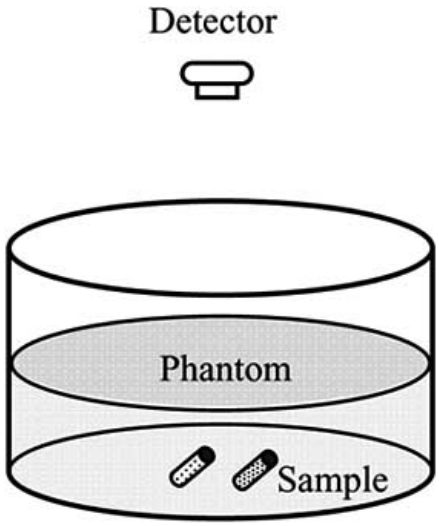

Fig. (1). Experimental tissue phantom setup (I).

ties within the visible and NIR spectral regions [23, 25]. In the following experiments, tissue phantoms composed of 1% Liposyn solutions (Abbot Labs, North Chicago, IL) were used to mimic the absorption and scattering properties of human breast tissue [23, 25-27].

Two types of experimental phantom setups were employed. First, different concentrations of PbS-QD filled cylindrical 20 × 8 mm glass vials were embedded in a 1% Liposyn phantom. By changing the volume of the Liposyn solution, tumors with different QD concentrations can be imaged at various phantom thicknesses (Fig. (**1**)). This procedure was used to provide insight into the possibility of using PbS QDs for deep tissue imaging, as well as impart a fundamental understanding of the contrast agent concentrations required for sufficient tumor image acquisition at various depths.

Second, a phantom-filled transparent container was placed above a 384-well microplate (Greiner Bio-one North America, Inc.) which has 3.7 × 3.7 mm square wells that were used to house quantum dot suspensions (see Fig. (**2**)). Two adjacent wells were filled, respectively, with CdSe/CdS red quantum dots and PbS NIR quantum dots of the same concentration (~1 μM) and same volume (100 μL/well). Using the Maestro imaging system, fluorescence images of tumor models with both the red QDs (acquired emission peak at ~645 nm) and the NIR QDs (acquired emission peak at ~880 nm) were analyzed. This procedure was used to obtain specific data about the blurring effect associated with using the tumor margin model for each type of QD, which was assessed by varying phantom thickness (Fig. (**2**)).

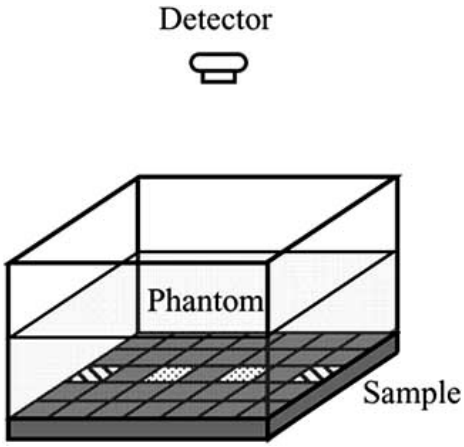

Fig. (2). Experimental tissue phantom setup (II).

The second phantom setup was used to simulate relatively small tumor tissue embedded close to superficial skin. To simultaneously image visible and NIR QDs, an excitation band of lower wavelengths was necessary. As a result of using lower wavelengths, however, the excitation photons could not penetrate deep into the tissue phantom. In addition, a strong autofluorescence background was associated with this excitation band. To minimize the influences of the excitation light, a superficial phantom setup was needed. Moreover, the 384-well microplate provided well-defined square geometries and sharp edges, which were necessary for the blurring-effect component of the study.

2.3. Fluorescence Image Acquisition and Processing

A Maestro imaging system equipped with proper filter sets (CRi, Woburn, MA) was used to acquire all the fluorescence images in this report. The working wavelength ranges of all the filters used were provided by the Maestro imaging system unless otherwise specified. Table **1** summarizes the filter sets that were used in the study. With the advantages of multispectral acquisition and quantitative data analysis, this system can provide improved imaging flexibility and sensitivity [28]. Therefore, the fluorescence signals from phantom autofluorescence, red QDs, and NIR QDs can be effectively separated from the stack of wavelength-resolved fluorescence images. To further evaluate the dimensions of the image of each square well of QDs, as described in the previous section (Fig. (**2**)), post-acquisition image processing was performed using MatLab codes.

Table 1. Filter Sets Used in Study

	Set 1	Set 2	Set 3
Excitation Filter	575–605 nm 615–665 nm	671–705 nm	503–555 nm
Emission Filter	700 nm longpass	750 nm longpass	600 nm longpass

3. RESULTS

Four cylindrical 20 × 8 mm glass vials were filled with 0.2 μM, 0.4 μM, 1 μM, and 2 μM PbS quantum dots suspended in phosphate buffered saline (PBS), respectively. For the condition in which there was no phantom above these vials (see Fig. (**1**)), fluorescence images of all four samples were obtained under the exact same acquisition conditions using the fluorescence imaging system. The average signal intensity of the acquired images of each vial of QDs was then extracted using the Maestro image processing program. To assess the influences of acquisition time and quantum dot concentration on the average signal intensities, NIR fluorescence images were taken in a series and then processed. As shown in Fig. (**3a**) and Fig. (**3b**), the average QD image intensity increased linearly as the QD concentration increased. Additionally, the slope also increased linearly as the acquisition time increased for images obtained with acquisition times of 100 ms, 200 ms, and 300 ms. The imaging results show that these same quantum dot image intensities can be affected by the particular applied excitation band [11]. Specifically, Fig. (**3a**) and Fig. (**3b**) show the differences that result from variations in the excitation bands, since the same 700 nm longpass emission filter was utilized. An excitation band from 615 to 665 nm was used for Fig. (**3a**), whereas the corresponding excitation band for Fig. (**3b**) ranged from 575 to 605 nm.

To evaluate the PbS QD concentration needed for an acceptable image at different tissue depths, the thickness of the phantom above each NIR tumor model was systematically varied (Fig. (**1**)). For the visible and near-infrared spectral ranges, the wavelength-dependent reduced scattering coefficient of the 1% Liposyn tissue phantom, as shown in Fig. (**4**), was obtained from previous literature [26, 27, 29-

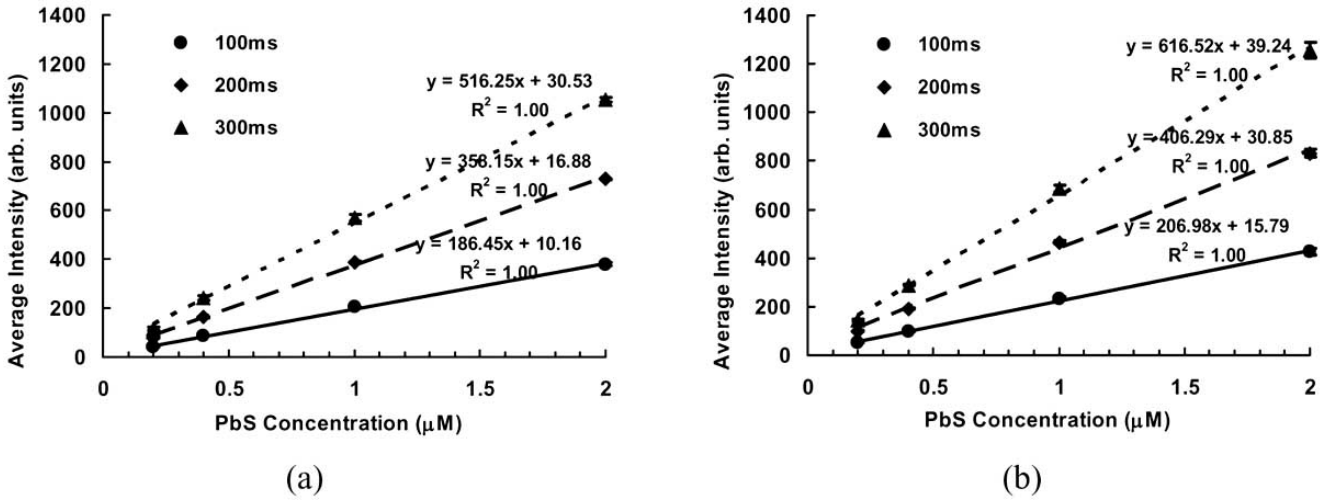

Fig. (3). Average image intensities of PbS NIR QDs acquired with no phantom and a 700 nm longpass emission (Em) filter (**a**) Ex (excitation): 615–665 nm (**b**) Ex: 575–605 nm. (n=3).

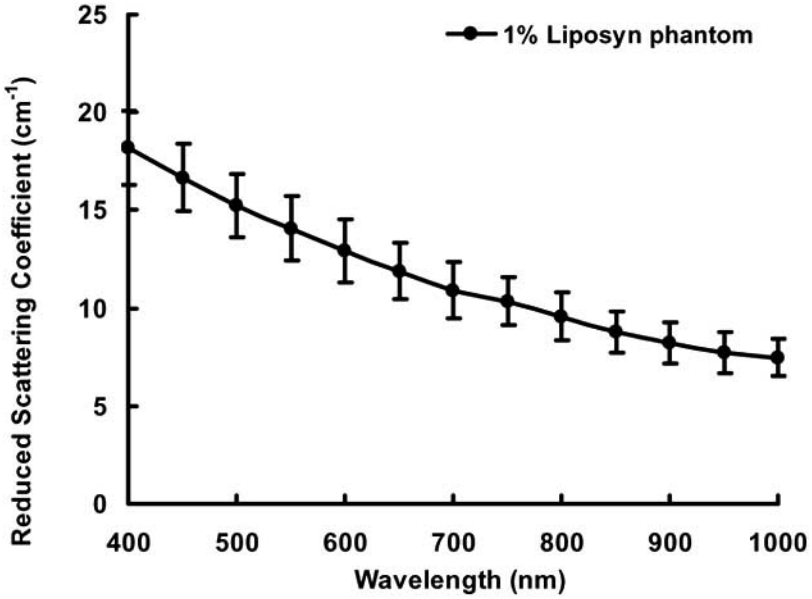

Fig. (4). Reduced scattering coefficient of 1% Liposyn tissue phantom.

31]. The corresponding absorption coefficient was dominated by water absorption, which varies from 0.001 to 0.3 cm^{-1} [26, 29, 32]. To demonstrate potential *in vivo* tissue diagnostic applications, the imaging process was optimized by using a bandpass excitation filter of 671 to 705 nm (deep-red excitation filter) coupled with a 750 nm longpass emission filter (deep-red emission filter) to acquire the fluorescence images of PbS-QD-filled tumor models. Both the average QD image intensity and quality decreased with increasing phantom thickness. To assess image quality, the tumor-to-background ratio (TBR) was evaluated. Similar to that described by Adams *et al.* [33], TBR is defined as the ratio of the average tumor region intensity to the average background region intensity. A TBR threshold value of 1.22 was used to distinguish acceptable images from unacceptable ones. Clear fluorescence images (TBR>1.22) of both 1 μM and 2 μM quantum dot suspensions were obtained at a phantom thickness of 25 mm with an acquisition time of 900 ms. However, even with the same imaging conditions, a clear QD image (TBR>1.22) could only be acquired at a phantom thickness of less than 20 mm for the 0.4 μM quantum dots. As for the 0.2 μM QD tumor model, which has a similar order of magnitude of QD concentration as previous reports [34], reasonable images could not be obtained when the phantom was thicker than 15 mm. The normalized average QD image intensities at various concentrations are shown in Fig. (**5**). These normalized average image intensities were obtained by subtracting the average background region intensities from the average tumor region intensities. Although the maximum imaging depths for different concentrations of QDs vary considerably, their normalized average image intensities have the same decreasing trend when plotted as a function of phantom thickness (Fig. (**5**)).

To compare the imaging properties of visible quantum dots and near-infrared quantum dots, the second experimental phantom setup (see Fig. (**2**)), as described in the methods section, was employed. The normalized fluorescence spectra of both CdSe/CdS (red) and PbS (NIR) quantum dots obtained under the same excitation and imaging conditions are shown in Fig. (**6**). A green bandpass excitation filter of 503 to 555 nm and a 600 nm longpass filter were used in tandem to simultaneously obtain the fluorescence images of both types of quantum dots. After spectral unmixing [28], CdSe/CdS

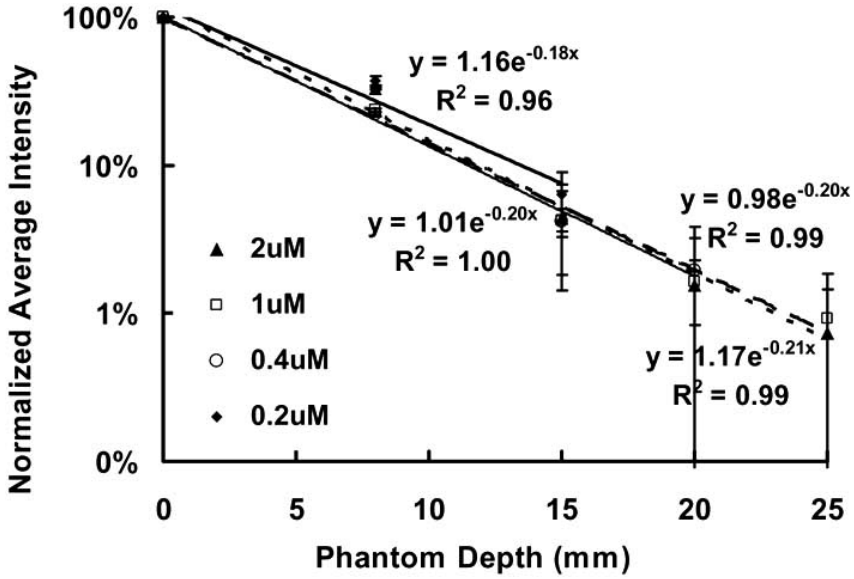

Fig. (5). Normalized average intensities of different concentrations of PbS NIR QDs versus phantom thickness (obtained with a bandpass excitation filter of 671 to 705 nm coupled with a 750 nm longpass emission filter, acquisition time: 900 ms) (n=3).

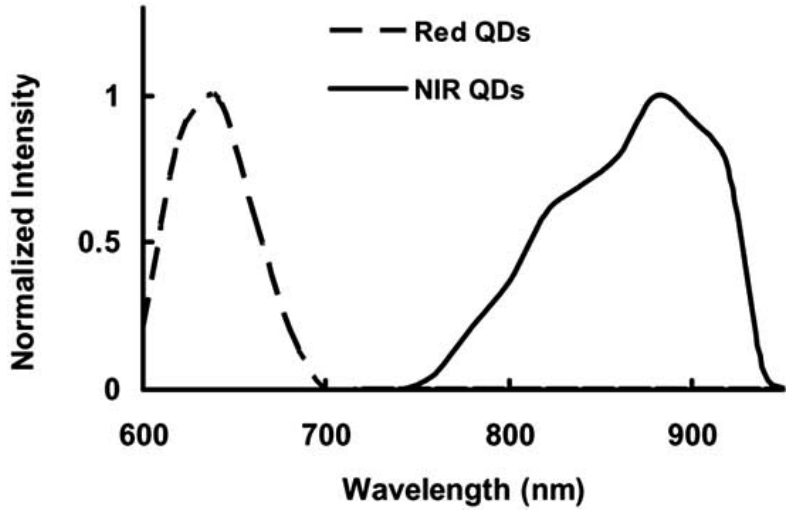

Fig. (6). Normalized fluorescence spectra of CdSe/CdS (red) and PbS (NIR) quantum dots (obtained with Maestro Imaging System).

(red) and PbS (NIR) quantum dot images can be isolated from each other as well as from the phantom autofluorescence. A series of fluorescence images, after the spectral unmixing processing for both the red and the NIR Qds, is shown in Fig. (**7**). Initially, when there are no phantoms above the QDs, clear images of the square wells can be acquired, and the image size of these wells is almost exactly the same for both types of QDs. As the phantom thickness gradually increased, the average intensities decreased for both kinds of quantum dot fluorescence images, a finding which supports previous results. Notably, the images of the red QDs are larger and less distinct than those of the NIR QDs, even though they are obtained under the same conditions. To compare the enlarging and blurring effects of these two different types of QDs as a function of the phantom thickness, a section line was drawn for each fluorescence square well in Fig. (**7**). This section line goes directly through the center of every square well image and splits it into two equal rectangular parts. The normalized fluorescence intensity along the section line was plotted as a function of pixel position. Based on the data in Fig. (**8**), it can be observed that when the phantom thickness increased from 0 to 1.75 mm, the half-intensity widths of the red-QD-filled wells expanded by ~300%, while those of the NIR-QD-filled wells expanded by only ~140%. Moreover, the margins of the NIR-QD-filled wells were better defined than the margins of the red-QD-filled wells.

4. DISCUSSION AND CONCLUSIONS

The phantom results indicate that lead sulfide NIR quantum dots possess essential properties for fluorescence imaging applications. Increasing either the concentration of QDs used or the image acquisition time can enhance collected image intensities. When PbS QDs are directly excited with yellow or red light and imaged with the Maestro system, clear fluorescence images can be obtained with the lowest tested concentration of 200 nM and the lowest tested acquisition time of 100 ms. In addition to these two factors, PbS QD fluorescence image intensity is also influenced by the excitation band used (Fig. (**3**)). Since tissue absorption and scattering effects are heavily wavelength-dependent [2, 18, 23], an optimized excitation band should be carefully chosen before PbS QDs are used for NIR tissue imaging applications.

For the results shown in Fig. (**5**), clear NIR images were obtained with the lowest tested PbS QD concentration of 200 nM at the phantom depth of 15 mm when imaged with an acquisition time of 900 ms and deep-red excitation and emission filter sets. The red-

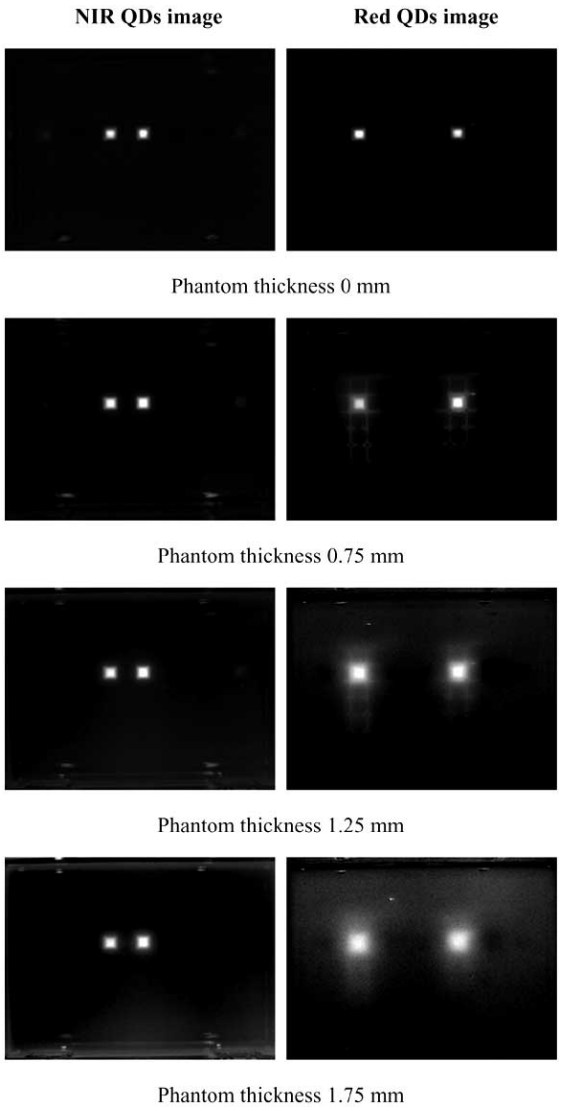

Fig. (7). Phantom thickness-resolved florescence images of NIR QDs (spectral unmixed, left column) and red QDs (spectral unmixed, right column).

shifted excitation band of 671 to 705 nm maximizes the illumination penetration depth into the tissue phantom, and the 750 nm longpass emission filter eliminates most phantom autofluorescence. Both factors improved image quality at relatively deep tissue sites. The optimal excitation and emission wavelengths for PbS QD fluorescence imaging were determined using a step-by-step approach. First, the emission wavelengths were selected to be in the NIR region. This region was selected because both tissue absorption and scattering coefficients are minimal in the NIR. For our imaging system, and with the use of PbS QD contrast agents, the optimal emission band of 750 to 950 nm was chosen. Then the optimal excitation wavelengths were selected based on the aforementioned emission band. There were three excitation filters available: one with an excitation band of 575 to 605 nm, a second with 615 to 665 nm, and a third with 671 to 705 nm. The 575 to 605 nm filter was eliminated because it induced a strong autofluorescence background. Although tissue phantom autofluorescence induced by the 615 to 665 and 671 to 705 nm filters were similar to each other, the 671 to 705 nm excitation band resulted in less tissue scattering. The optimal excitation wavelength range of 671 to 705 nm was finally chosen in conjunction with the optimal emission band of 750 to 950 nm. As shown in Fig. (**5**), although the QD concentration and the imaging depth vary over a wide region, the normalized average image intensity for each assessed concentration possesses the same variable trend with respect to the corresponding increase in tissue phantom depth.

Another advantage of using PbS QDs for tissue imaging applications is their red-shifted emission wavelengths in the NIR region. As previously reported, tissue absorbs and scatters NIR light less than UV or visible light [2, 26, 35]. Therefore, most of the NIR emission photons from PbS QDs will pass through the phantom with only a few scattering events and be detected by the camera [1, 19, 36]. This reduced scattering effect will potentially result in an important property of NIR QD imaging: improved margin delineation.

The ability to obtain better-confined tumor images significantly impacts both cancer diagnosis and surgery [37-40]. Currently, surgeons excise both the suspected malignant tumor tissue and the benign tissue surrounding the tumor site to ensure elimination of cancer cells. Aside from causing the patient pain and suffering, this procedure requires extensive recovery time [37-40]. However, if the tumor could be imaged with improved clarity during surgery, for example, with the potential help of bioconjugated PbS NIR QDs, the required tissue excision would be greatly reduced, with promising benefits for both patients and physicians [37-40].

As shown in Fig. (**7**), as the phantom thickness increases, the images of the NIR-QD-filled square wells demonstrate better-

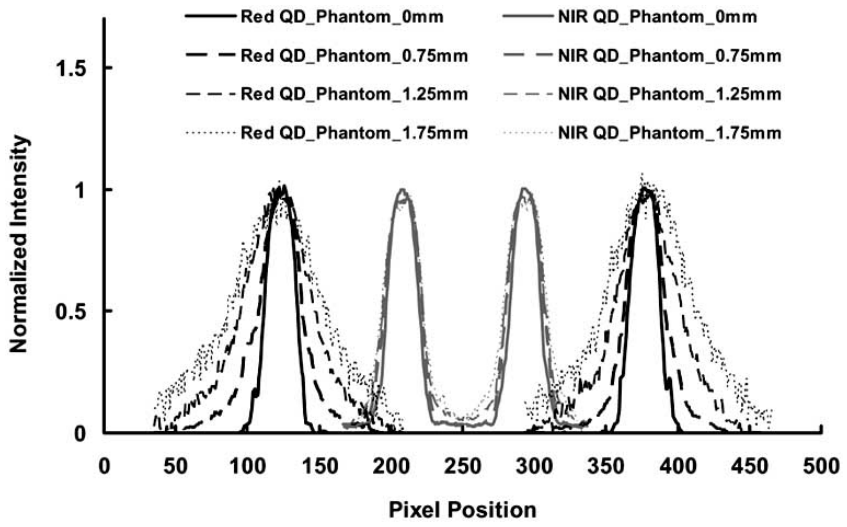

Fig. (8). Normalized fluorescence intensity of red and NIR QDs at various phantom depths versus pixel position along section line.

defined margins than those of the red-QD-filled wells. In addition, the images of the red wells with a 1.75 mm phantom are much larger than their initial images taken without a phantom, even though both were obtained under the same imaging conditions. In contrast, the corresponding images of the NIR wells are similar in size regardless of phantom presence. It is believed that the wavelength-dependent phantom optical properties may be one of the most important factors that result in these different red and NIR images.

Although the experimental results shown in Fig. (**7**) are promising, there may be concerns about the green excitation band (503 to 555 nm) used and the maximum imaging depth achieved. A green filter was used for excitation in order to simultaneously excite both the red and NIR QDs and compare the images obtained under the same conditions. With the fluorescence imaging system, a red (615 to 665 nm) or deep-red (671 to 705 nm) excitation band is typically recommended for deep tissue PbS NIR QD imaging because this band maximizes illumination penetration and, simultaneously, avoids the excitation of most tissue autofluorescence. The maximum phantom depth of 1.75 mm was applied in the above experiments in order to obtain reasonable images from both the red and NIR QDs at that depth.

In conclusion, a phantom study in which PbS QDs are used as contrast agents for fluorescence imaging applications is reported. The experiments show that lead sulfide NIR quantum dots possess enhanced fluorescence imaging properties. When collected with the deep-red excitation and emission filter set, adequate NIR QD fluorescence images were obtained with a maximum tissue phantom thickness of 15 mm at a particle concentration of 200 nM and an acquisition time of 900 ms. Furthermore, the improved tumor margin confinement images obtained from PbS QD contrast agents, as explained above, are indicative of their promising surgical applications for future *in vivo* tumor detection.

ACKNOWLEDGEMENTS

The authors thank financial support for this work by the Department of Defense Congressionally Directed Breast Cancer Research Program Era of Hope Scholar Award, the Center for Biological and Environmental Nanotechnology (EEC-0118007 and EEC-0647452), and the Gulf Coast Center for Computational Cancer Research. We thank Mr. David Martin for his editing assistance.

ABBREVIATIONS

PbS	=	lead sulfide
NIR	=	near-infrared
QDs	=	quantum dots
FIS	=	fluorescence imaging system
TEM	=	transmission electron microscopy
UV	=	ultraviolet
PBS	=	phosphate buffered saline
TBR	=	tumor-to-background ratio
Em	=	emission
Ex	=	excitation

REFERENCES

[1] Wilson, B.C.; Jacques, S.L. Optical reflectance and transmittance of tissue: principles and application. *IEEE J. Quantum Electron.*, **1990**, *26*, 2186.

[2] Cheong, W.F.; Prahl, S.A.; Welch, A.J. Review of the optical properties of biological tissues. *IEEE J. Quantum Electron.*, **1990**, *26*, 2166.

[3] Pogue, B.W.; Geimer, S.; McBride, T.O.; Jiang, S.; Osterberg, U.L.; Paulsen, K.D. Three-dimensional simulation of near-infrared diffusion in tissue: boundary condition and geometry analysis for finite-element image reconstruction. *Appl. Opt.*, **2001**, *40*, 588.

[4] Kim, S.; Lim, Y.T.; Soltesz, E.G.; De Grand, A.M.; Lee, J.; Nakayama, A.; Parker, J.A.; Mihaljevic, T.; Laurence, R.G.; Dor, D.M.; Cohn, L.H.; Bawendi, M.G.; Frangioni, J.V. Near-infrared fluorescent type II quantum dots for sentinel lymph node mapping. *Nat. Biotechnol.*, **2004**, *22*, 93.

[5] Cai, W.; Shin, D.-W.; Chen, K.; Gheysens, O.; Cao, Q.; Wang, S.X.; Gambhir, S.S.; Chen, X. Peptide-labeled near-infrared quantum dots for imaging tumor vasculature in living subjects. *Nano Lett.*, **2006**, *6*, 669.

[6] Michalet, X.; Pinaud, F.F.; Bentolila, L.A.; Tsay, J.M.; Doose, S.; Li, J.J.; Sundaresan, G.; Wu, A.M.; Gambhir, S.S.; Weiss, S. Quantum dots for live cells, in vivo imaging, and diagnostics. *Science*, **2005**, *307*, 538.

[7] Lin, A.W.H.; Lewinski, N.A.; West, J.L.; Halas, N.J.; Drezek, R.A. Optically tunable nanoparticle contrast agents for early cancer detection: model-based analysis of gold nanoshells. *J. Biomed. Opt.*, **2005**, *10*, 064035.

[8] Zuluaga, A.F.; Drezek, R.; Collier, T.; Lotan, R.; Follen, M.; Richards-Kortum, R. Contrast agents for confocal microscopy: how simple chemicals affect confocal images of normal and cancer cells in suspension. *J. Biomed. Opt.*, **2002**, *7*, 398.

[9] Hines, M.A.; Scholes, G.D. Colloidal PbS nanocrystals with size-tunable near-infrared emission: observation of post-synthesis self-narrowing of the particle size distribution. *Adv. Mater.*, **2003**, *15*, 1844.

[10] Medintz, I.L.; Uyeda, H.T.; Goldman, E.R.; Mattoussi, H. Quantum dot bioconjugates for imaging, labeling and sensing. *Nat. Mater.*, **2005**, 435.

[11] Zhu, M.-Q.; Chang, E.; Sun, J.; Drezek, R.A. Surface modification and functionalization of semiconductor quantum dots through reactive coating of silanes in toluene. *J. Mater. Chem.*, **2007**, *17*, 800.

[12] Bakueva, L.; Gorelikov, I.; Musikhin, S.; Zhao, X.S.; Sargent, E.H.; Kumacheva, E. PbS quantum dots with stable efficient luminescence in the near-IR spectral range. *Adv. Mater.*, **2004**, *16*, 926.

[13] Clapp, A.R.; Medintz, I.L.; Mauro, M.; Fisher, B.R.; Bawendi, M.G.; Mattoussi, H. Fluorescence resonance energy transfer between quantum dot donors and dye-labeled protein acceptors. *J. Am. Chem. Soc.*, **2004**, *126*, 301.

[14] Bruchez, M.J.; Moronne, M.; Gin, P.; Weiss, S.; Alivisatos, A.P. Semiconductor nanocrystals as fluorescent biological labels. *Science*, **1998**, *281*, 2013.

[15] Medintz, I.L.; Clapp, A.R.; Mattoussi, H.; Goldman, E.R.; Fisher, B.; Mauro, J.M. Self-assembled nanoscale biosensors based on quantum dot FRET donors. *Nat. Mater.*, **2003**, *2*, 630.

[16] Choi, J.; Wolf, M.; Toronov, V.; Wolf, U.; Polzonetti, C.; Hueber, D.; Safonova, L.P.; Gupta, R.; Michalos, A.; Mantulin, W.; Gratton, E. Noninvasive determination of the optical properties of adult brain: near-infrared spectroscopy approach. *J. Biomed. Opt.*, **2004**, *9*, 22114(14).

[17] Zimmer, J.P.; Kim, S.-W.; Ohnishi, S.; Tanaka, E.; Frangioni, J.V.; Bawendi, M.G. Size series of small indium arsenide-zinc selenide core-shell nanocrystals and their application to in vivo imaging. *J. Am. Chem. Soc.*, **2006**, *128*, 2526.

[18] Richards-Kortum, R.; Sevick-Muraca, E. Quantitative optical spectroscopy for tissue diagnosis. *Annu. Rev. Phys. Chem.*, **1996**, *47*, 555.

[19] Mycek, M.-A.; Pogue, B.W. *Handbook of Biomedical Fluorescence*, Marcel Dekker, Inc.: New York, Basel, **2003**.

[20] Drezek, R.; Sokolov, K.; Utzinger, U.; Boiko, I.; Malpica, A.; Follen, M.; Richards-Kortum, R. Understanding the contributions of NADH and collagen to cervical tissue fluorescence spectra: Modeling, measurements, and imliications. *J. Biomed. Opt.*, **2001**, *6*, 385.

[21] Georgakoudi, I.; Jacobson, B.C.; Mueller, M.G.; Sheets, E.E.; Badizadegan, K.; Carr-Locke, D.L.; Crum, C.P.; Boone, C.W.; Dasari, R.R.; Van Dam, J.; Feld, M.S. NAD(P)H and collagen as in vivo quantitative fluorescent biomarkers of epithelial precancerous changes. *Cancer Res.*, **2002**, *62*, 682.

[22] Sun, J.; Zhu, M.-Q.; Fu, K.; Lewinski, N.; Drezek, R.A. Lead sulfide near-infrared quantum dot bioconjugates for targeted molecular imaging. *Int. J Nanomed.*, **2007**, *2*, 235.

[23] Pogue, B.W.; Patterson, M.S. Review of tissue simulating phantoms for optical spectroscopy, imaging and dosimetry. *J. Biomed. Opt.*, **2006**, *11*, 041102.

[24] Torricelli, A.; Pifferi, A.; Taroni, P.; Giambattistelli, E.; Cubeddu, R. *In vivo* optical characterization of human tissues from 610 to 1010 nm by time-resolved reflectance spectroscopy. *Phys. Med. Biol.*, **2001**, *46*, 2227.

[25] Joshi, A.; Bangerth, W.; Sevick-Muraca, E.M. Non-contact fluorescence optical tomography with scanning patterned illumination. *Opt. Express*, **2006**; 14(14): 6516.

[26] Jacques, S. *Oregon Medical Laser Center, Portland, OR. Available at: http://omlc.ogi.edu/spectra/intralipid*, **1998**.

[27] Hebden, J.C.; Veenstra, H.; Dehghani, H.; Hillman, E.M.C.; Schweiger, M.; Arridge, S.R.; Delpy, D.T. Three-dimensional time-resolved optical tomography of a conical breast phantom. *Appl. Opt.*, **2001**, *40*, 3278.

[28] *User manual for Maestro 2.2 (CRi)*, CRi, **2006**.

[29] Xu, H.; Patterson, M.S. Determination of the optical properties of tissue-simulating phantoms from interstitial frequency domain measurements of relative fluence and phase difference. *Opt. Express*, **2006**, *14*, 6485.

[30] Godavarty, A.; Eppstein, M.J.; Zhang, C.; Theru, A.; Thompson, A.B.; Gurfinkel, M.; Sevick-Muraca, E.M. Fluorescence-enhanced optical imaging in large tissue volumes using a gain-modulated ICCD camera. *Phys. Med. Biol.*, **2003**, *48*, 1701.

[31] van Staveren, H.J.; Moes, C.J.M.; van Marle, J.; Prahl, S.A.; van Gemert, M.J.C. Light scattering in intralipid-10% in the wavelength range of 400-1100 nm. *Appl. Opt.*, **1991**, *30*, 4507.

[32] Palmer, K.F.; Williams, D. Optical properties of water in the near infrared. *J. Opt. Soc. Am.*, **1974**, *64*, 1107.

[33] Adams, K.E.; Ke, S.; Kwon, S.; Liang, F.; Fan, Z.; Lu, Y.; Hirschi, K.; Mawad, M.E.; Barry, M.A.; Sevick-Muraca, E.M. Comparison of visible and near-infrared wavelength-excitable fluorescent dyes for molecular imaging of cancer. *J. Biomed. Opt.*, **2007**, *12*, 024017.

[34] Chu, T.C.; Shieh, F.; Lavery, L.A.; Levy, M.; Richards-Kortum, R.; Korgel, B.A.; Ellington, A.D. Labeling tumor cells with fluorescent nanocrystal-aptamer bioconjugates. *Biosens. Bioelectron.* **2006**, *21*, 1859.

[35] Qu, J.; MacAulay, C.; Lam, S.; Palcic, B. Optical properties of normal and carcinomatous bronchial tissue. *Appl. Opt.*, **1994**, *33*, 7397.

[36] Wang, L.-H.; Jacques, S.L.; Zheng, L.-Q. MCML-Monte Carlo modeling of photon transport in multi-layered tissues. *Comput. Meth. Prog. Biol.*, **1995**, *47*, 131.

[37] Kappas, A.M.; Roukos, D.H. Quality of surgery determinant for outcome of patient with gastric cancer. *Ann. Surg. Oncol.*, **2002**, *9*, 828.

[38] Haka, A.S.; Volynskaya, Z.; Gardecki, J.A.; Nazemi, J.; Lyons, J.; Hicks, D.; Fitzmaurice, M.; Dasari, R.; Crowe, J.P.; Feld, M.S. *In vivo* margin assessment during partial mastectomy breast surgery using Raman spectroscopy. *Cancer Res.*, **2006**, *66*, 3317.

[39] Haglund, M.M.; Hochman, D.W.; Spence, A.M.; Berger, M.S. Enhanced optical imaging of rat gliomas tumor margins. *Neurosurgery*, **1994**, *35*, 930.

[40] McDougal, W.S. Conservative surgery for penile cancer: what surgical excision margins are needed to achieve oncologic control? *Nat. Clin. Pract. Oncol.*, **2006**, *3*, 132.

Received: July 23, 2008 Revised: October 20, 2008 Accepted: December 03, 2008

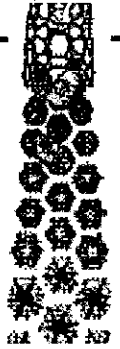

For reprint orders, please contact: reprints@futuremedicine.com

Photothermal bubbles as optical scattering probes for imaging living cells

Aims: We propose and have experimentally studied a new method with improved sensitivity and specificity of imaging of living cells. **Method:** Intracellular photothermal bubbles generated around gold nanoparticles (NPs) and their clusters were proposed as optical scattering probes for the amplification of scattered light. **Results:** Microbubbles generated around gold spheres and shells with 10-ns 532-nm laser pulses in individual living cells (leukemia cells, lung and squamous carcinoma cancer cells) have amplified optical side scattering up to 1800-times relative to that of intracellular gold NPs, and without detectable damage to host cells. We explain the discovered optical amplification by the endocytosis-mediated clustering of NPs in cells, and by the selective generation of microbubbles (that do not disrupt the host cell) around these clusters at minimal levels of laser pulse fluence. **Conclusions:** Photothermal bubbles generated around laser-activated gold NPs may significantly improve the sensitivity and specificity of cell imaging, and can be considered as a new type of optical cellular probes.

KEYWORDS: bubble, cell, endocytosis, gold nanoparticle, photothermal, scattering

Ekaterina Y Hleb[1], Ying Hu[2], Rebekah A Drezek[2], Jason H Hafner[3] & Dmitri O Lapotko[1,3]

*Author for correspondence:
[1]AV Lykov Heat & Mass Transfer Institute, 15 P Brovka Street, Minsk, 220072, Belarus
[2]Department of Bioengineering, Rice University, Houston, TX 77005, USA
[3]Department of Physics & Astronomy, Rice University, Houston, TX 77005, USA
Tel: +375 172 842 483;
Fax: +375 172 842 483;
E-mail: dmitri.lapotko@rice.edu

The excellent optical absorption and scattering properties of metal nanoparticles (NPs), combined with their safety and functionality of selective targeting, have stimulated their cytometric and imaging applications as cellular and molecular probes [1]. Gold NPs are the safest imaging nanomaterial [2,3], and their optical properties can be adjusted through their shape and size [2–8]. Functionalized gold NPs can be delivered to target molecules located in the cellular membrane, and potentially to the cytoplasm and nuclei without compromising cell physiology [9,10]. Optical scattering with NPs as cellular probes [11–15] has been applied for microscopy, flow cytometry and endoscopy by coupling strongly scattering NPs with target endogenous molecules, whose scattering properties are too weak for imaging. Results have shown the strong potential of gold NPs as optical probes. Scattered optical signals can be detected *in vivo* and *in situ*. In comparison with fluorescent probes, gold NPs are less toxic and have higher photodamage thresholds. However, gold NPs as optical scattering probes do not provide high sensitivity and specificity at the cellular and molecular levels, especially when being used in a highly heterogeneous environment, which is typical for *in vivo* application. Cellular components provide a strong scattering background. The optical energy that is scattered by NPs depends strongly on the particle's diameter (the sixth power), which requires an increase of probe size by hundreds of nanometers to improve sensitivity. However, this complicates the delivery of the NPs into the cells because biological factors limit the maximal diameter of NPs that can be delivered into living cells by 100 nm for cytoplasm, and by 20 nm for nuclei [9,10]. The scattering efficiency of small single NPs may be relatively low compared with background scattering from endogenous cellular components. Therefore, the cell level scattering imaging (especially for intracellular targets) requires a significant increase in the sensitivity and in the specificity, although without an increase of NP dimensions and laser fluence to avoid photodamage to the cell.

A further increase in the sensitivity of the imaging methods that use NPs as probes may be achieved by using the photothermal (PT) properties of NPs and the secondary phenomena of laser–NP interactions such as thermal diffusion, resulting in heating of the surrounding volume, pressure waves and bubble generation owing to media vaporization [16–18]. The combination of PT-imaging techniques [19–22] with the optical properties of metal NPs has shown promising results in optical microscopy, with a detection limit for probe size of several nanometers and a high signal-to-noise ratio [23,24]. However, optical refractive index gradients (even produced by heated metal NPs) are relatively small, and thus limit the sensitivity and temporal resolution of PT imaging.

future Medicine part of fsg

Furthermore the PT methods require increasing the laser-induced temperature for better sensitivity, and this may cause thermal damage to the probe (or target molecule, cell and organ), and also to collateral cells and tissues [25,26]. If the energy is concentrated in too short laser pulses, the risk of optical damage of the probe or cell also increases [27,28].

To be applied for the analysis of single living cells and even molecules, optical scattering methods require a significant increase in sensitivity, although they are attractive owing to their safety, speed and universal applicability. We have proposed a new imaging method based upon using vapor bubbles as optical cellular probes. This approach uses the most universal and natural PT and scattering processes through the amplification of optical scattering with vapor bubbles generated around light-absorbing NPs. The generation of PT bubbles (PTBs) in living tissues is a well-known phenomenon [29–33], but the bubbles were considered to be a damaging factor to the cells. Based on this the bubbles in living cells were detected optically to monitor cell damage [34–36]. As a result, laser-induced intracellular bubbles were not yet considered as cellular-imaging probes, despite their excellent optical scattering properties and high imaging potential, as was demonstrated in other applications [37–43]. Despite the inherent disruptive nature of the bubbles, it has been experimentally determined that optically or acoustically generated bubbles of a small size may not damage the cells [44–47].

In this article, we have used previous knowledge on the scattering imaging of cells, PTB generation around light-absorbing NPs and NP internalization by living cells to propose the new concept of optical cellular probes and scattering imaging. This concept is based on our hypothesis that the PTBs generated around a gold NP in a living cell may significantly amplify the optical scattering without damage to the host cell.

Methods & materials

□ Principle of nanocluster–PTB intracellular amplification of optical signals

The optical scattering signal (S) (Figure 1A) from metal NPs and their clusters is generated through plasmon resonance. The scattering-signal amplitude increases with the probe (NP) diameter to the sixth power. Clustering of small NPs inside the cell [48] increases the total diameter of the scattering probe and over-rides the biological limitation on the maximum diameter of NPs for intracellular delivery. Further amplification of scattering requires an increase in probe diameter and incident optical energy; both parameters are limited for living cells. For this reason, we suggest two mechanisms for increasing optical scattering from intracellular NP probes without damage to cells:

- Small NPs are delivered selectively to the target cells and are internalized through the mechanism of endocytosis, and are concentrated into

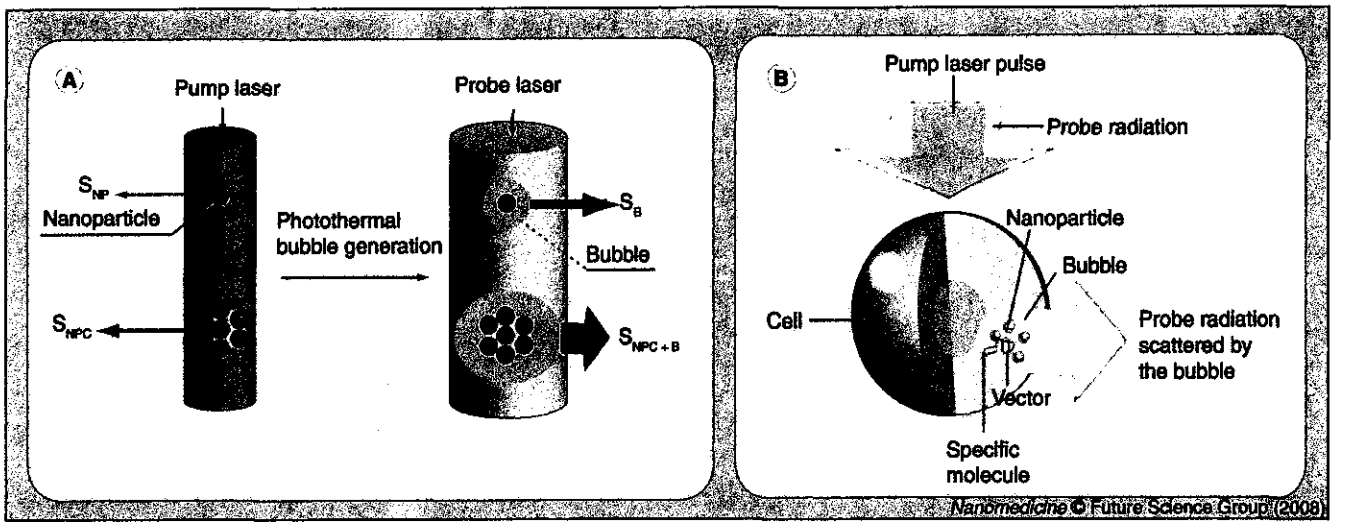

Figure 1. The principle of amplification of optical scattering and its application for cell imaging. (A) Nanoparticle (NP) cluster–photothermal bubble (PTB) mechanism of amplification of optical scattering from gold NPs: amplitude of optical S can be increased to S_{NPC} through formation of the NP cluster, and can be further increased to S_B through generating the transient vapor bubble around the NP or NP cluster, resulting in the maximal signal S_{NPC+B}. **(B)** The principle PTB imaging of living cells: short pump pulse induces a transient intracellular PTB around the molecule-associated NP cluster; scattering of probe laser beam by PTB forms an optical signal.
S: Signal.

the clusters in cellular endosomes. NP clustering as a result of endocytosis were previously studied by our group in detail [48–51]. Additionally, the formation of NP clusters during endocytosis was also experimentally verified by other researchers [52,53]. We define a cluster as a group of tightly packed NPs, with the dimensions spanning 2–50 times the size of the NP;

- Exposure of the cell containing NP clusters to a short laser pulse at the plasmon resonance wavelength of NPs would generate vapor PTBs with larger diameters than those of NP clusters and single NPs, and with high refractive index gradients at the vapor–liquid boundary, thus further increasing optical scattering.

We have previously verified that NP clusters provide more efficient generation of PTBs at lower levels of laser pulse fluencies [48–51,54,55]. For this reason, we do not consider the detailed mechanism of clustering, which is beyond the scope of this current work and can be found in the cited publications. Also, in our previous experimental experience, we have found that the pump wavelength for PT excitation of NP clusters does not differ dramatically from that for single NPs: clusters mainly broaden the absorbance spectrum rather than shift it. Apart from the pump laser beam that is used to generate PTBs, the auxiliary probe laser can be used for optical scattering. The wavelength of the probe laser can be optimized to enable the increase of probe laser fluence (and hence the amplitude of scattered light) without causing damage to the cell. This mechanism of optical amplification is universal, and depends on the properties of gold NPs and laser parameters. It depends less on the cell properties, so that PTB generation can be controlled precisely through the laser and NP parameters.

Optical intracellular amplification can be realized in any living cell where an NP cluster is formed (Figure 1B), with irradiation of the cell with pump and probe laser pulses at different wavelengths. The pump pulse generates the bubble and the probe laser provides the scattered signal. An additional advantage of the PTB is its 'on-demand' nature; it does not exist before or after the pump laser pulse. During its nano-to-microsecond lifetime, the PTB can be detected in specific time domains. This would allow the imaging of several PTBs with different lifetimes associated with different molecular targets, and would improve the signal-to-noise ratio relative to the *in vivo* background that may be highly scattering.

Samples: nanoparticles, cells & their targeting

We have used two types of gold NPs, because gold NPs are the safest for living cells among all nanomaterials and minimally disturb cell physiology. Previously, we have studied the cytotoxicity of gold NPs and their conjugates during NP internalization and endocytotic clustering, and no significant suppression of cell viability was found [48–50]. The nontoxic nature of gold NPs has also been confirmed in many independent studies. However, detailed study of this subject is beyond the scope of this current work, and can be found in several reviews [2,3]. Silica/gold nanoshells (NSs) with a diameter of 170 nm and absorption maximum in the near-infrared (760 nm) range were prepared as described in [56]. Gold spheres with a diameter of 30 nm and the peak absorbance at 530 nm were obtained from Ted Pella, Inc. (#15706, Redding, CA, USA). Extinction spectra of all used NPs were verified with a spectrophotometer (USB 650 Red Tide, Ocean Optics Inc., Dunedin, FL, USA). Three types of tumor cells were used: K562 (leukemia CD33-positive blast cells) and two solid tumor cells, Hep-2C and A549, highly expressing the EGF receptor. All those cells represent different cancers (leukemia, squamous cell carcinoma and lung cancer, respectively), and are of interest in terms of cancer diagnostics and treatment.

NP clusters were formed in cells through nonspecific binding of NPs to the cell membrane and nonspecific endocytotic concentration of the NPs in endosomal compartments. Internalization and clustering of gold NPs into large compact aggregates was previously studied by our group [48–50] and others [52,53]; therefore, we have previously verified clustering protocols. The cells were incubated in the media RPMI 1640 at 37°C for 60 min with 20% (volume) suspension of the NPs at a concentration of 10^9 NP/ml. This stimulated nonspecific endocytosis of the NPs, and their consequent clustering in endosomal compartments. After preparation, the samples were immediately used in the experiments at room temperature.

PTB generation & optical detection

We have used a PT microscope previously developed by our group [57] for the generation, imaging and measurement of PTBs in individual cells and in suspensions of NPs [48–51,58–61]. PTBs were generated with a single 10-ns focused laser pulse at 532 nm (Laser LS-2132, Lotis

TII, Minsk, Belarus). This pulse length was short enough compared with the characteristic time of thermal diffusion so that the bubbles could be generated effectively at a submicrometer scale, yet also long enough to ensure that no optical breakdown or two-photon optical absorption would occur. Our recent studies of the PT properties of gold nanorods, NSs and nanospheres have shown that this wavelength (532 nm) is efficient for the excitation of plasmon resonances in NPs under relatively high laser fluencies [62], which is required for PTB generation. In particular, for a gold NS, the laser fluence threshold of PTB generation was several times lower at 532 nm, compared with that at 760 nm. Pulse fluence was varied by rotating Glan prism in the path of a laser beam. Pulse fluence was obtained by measuring pulse energy with a calibrated meter (Ophir PE10-SH, Ophir Optronics, Ltd, Israel), and by measuring the actual pump beam diameter on the sample plane with a CCD image detector (Luca DL-658M, Andor Technology, Ireland). Each individual cell (100 cells for each sample) was irradiated one by one with a single focused laser pulse of the same fluence. PTB generation in NP suspensions was realized by sequential exposure to the laser pulse of the different areas of the suspension.

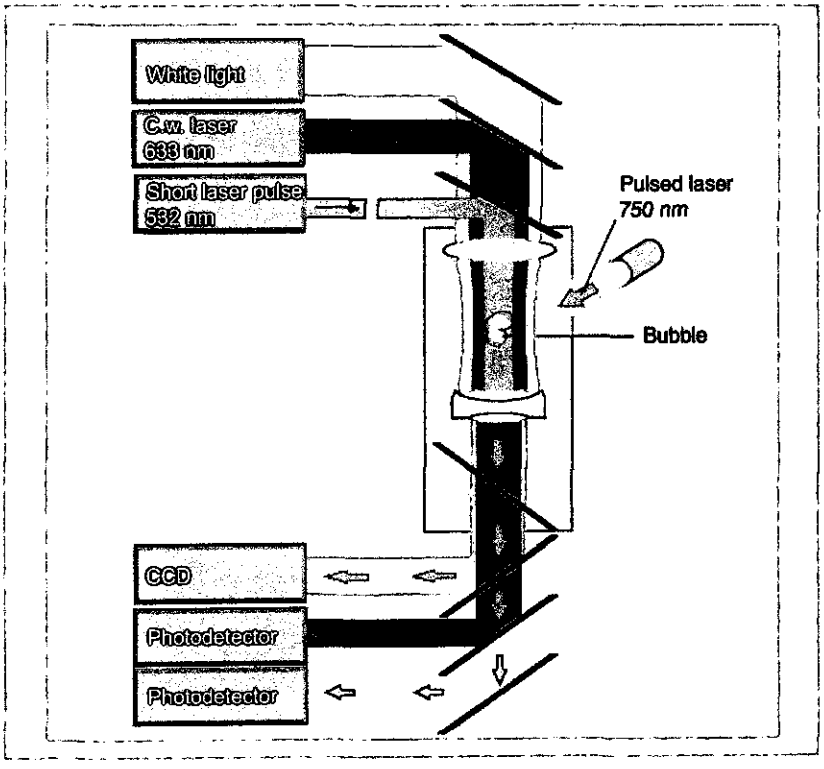

Figure 2. Block diagram of the experimental set-up: light delivery and collection. Bubble generation with laser pulse (532 nm), bubble detection with thermal lens method (continuous probe laser is registered with photodetector) and with side-scattering imaging: probe pulse was delivered though the optical fiber and was imaged with a digital camera and registered with a photodetector.
CCD: Charge-coupled camera; c.w.: Continuous wave laser.

PTBs were imaged with an optical side-scattering time-resolved technique, and were also independently monitored with the thermal lens method described by us previously [57,58]. Time–response of the PTB was registered with a continuous probe beam at 633 nm (FIGURE 2). This type of signal enables PTB dynamics to be monitored, and its lifetime to be measured. Any PTB-related change of the media's refractive index causes a shift of the probe beam phase that influences beam intensity in the input of the photodetector (PDA10A, Thorlabs Inc., Newton, NJ, USA). Electrical output of the photodetector was acquired as a time–response measurement by a high-speed digitizer (Bordo-211, Auris Ltd, Minsk, Belarus) and, in the case of the PTB, this response has a specific negative symmetrical pattern so that the PTB could be distinguished from other optical signals during sample irradiation with the pump laser pulse. Time-resolved side-scattering images of the PTBs were obtained with a pulsed probe laser beam with a wavelength of 750 nm and duration of 10 ns (LT-2211 Ti-Sa laser, Lotis TII). The low-fluence probe pulse was delayed relatively to the pump pulse for 150 ns, thus allowing the detection of the developed PTB (FIGURE 2). The probe beam was directed into the sample at an angle of approximately 80°, which was optimized to detect scattered signals from gold NPs. Probe pulse scattered by NPs, NP clusters or PTBs was collected with a 60× objective (NA 0.4), and was imaged with a CCD camera. The delay and duration of the probe pulse provided time-resolved imaging without the need for a high-speed camera.

Integral scattered light was also registered with an additional photodetector (PDA55, Thorlabs Inc.) so as to independantly measure the amplitude of the scattered light (FIGURE 2). The electrical output signal of the photodetector was acquired as a time–response measurement by a high-speed digitizer (Bordo-211, Auris Ltd, Minsk, Belarus), and its maximal amplitude was referred to as the amplitude of integral scattered optical signal.

Using these three optical techniques simultaneously enabled us to detect and monitor the generation of the PTB and to confirm that the main pump laser-induced phenomenon was, in fact, the generation of a vapor bubble around light-absorbing NPs.

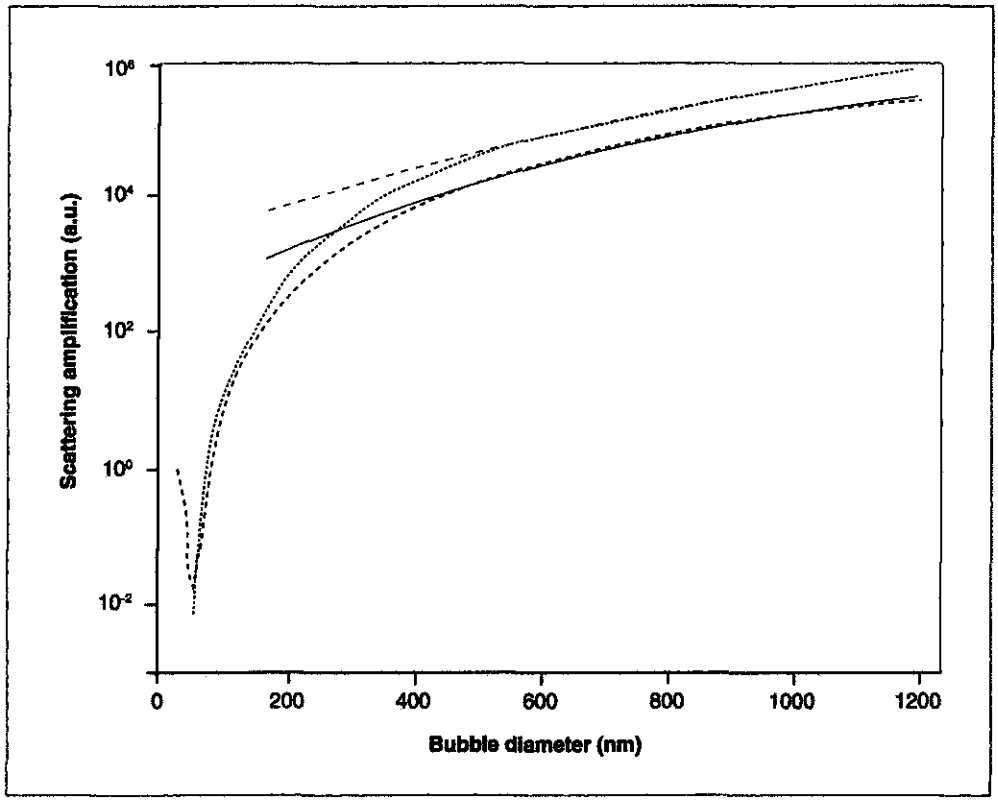

Figure 3. Theoretical modeling of the amplification of optical side scattering by the air bubble surrounding a 30-nm gold sphere and a 170-nm silica-gold shell as a function of the bubble diameter. The amplitudes of scattered light were normalized by those for a 30-nm gold sphere (without the bubble) so to demonstrate the bubble effect and are shown for 633 nm (short dash: for gold sphere; solid: for silica-gold nanoshell) and 750 nm (dot: for gold sphere; long dash: for silica-gold nanoshell).

Results

□ Modeling optical scattering from a bubble versus NP

The theoretical modeling of light scattering from bubbles generated around gold NPs is based on a Mie simulation code developed for multilayer concentric spheres. Subject to general limitations of Mie calculations, the assumptions made here are that NPs and bubbles are rigidly spherical in shape; bubbles are perfectly centered on NPs and the illumination is along a plane wave.

Owing to the nonabsorbent nature of the bubbles, the scattering cross-section (C_{sca}) is an effective figure of measurement for their optical properties. The differential scattering cross-section, $dC_{sca}/d\Omega$, is defined as the time-averaged energy projected into a unit solid angle, $d\Omega$, at a direction, $\hat{\Omega}$. It is expressed in terms of scattered *irradiance*, I_s, incident irradiance, I_i, and distance, r, from the center of the sphere to the detector:

$$\frac{dC_{sca}}{d\Omega} = r^2 \frac{I_s}{I_i}$$

By integrating over all solid angles, Ω, one obtains the C_{sca}, which, from the definition above, is also equal to the percentage of scattered power in all directions with respect to the incident power multiplied by r^2. Therefore, given C_{sca} and r, the percentage of total scattered power can be obtained. Based on Mie coefficients a_n and b_n derived from the aforementioned code, C_{sca} can be calculated by [47]:

$$C_{sca} = \frac{2\pi}{k^2} \sum_{n=1}^{\infty} (2n + 1)(|a_n|^2 + |b_n|^2)$$

where k is the wave number in the surrounding medium and n is the summation index terminated at some N_{max}. The detector r can be estimated from the experimental setup.

Figure 3 plots the relative levels of total scattered power for a gold sphere with a diameter of 30 nm and a silica–gold NS with an outer diameter of 170 nm and a gold-layer thickness of 8 nm, each NP surrounded by the single air bubble suspended in water. To demonstrate the amplification effect of the bubble, the data were normalized by that for a single 30-nm gold NP without a surrounding bubble. Of note is the general trend of increase in scattering against PTB radius. This can be understood qualitatively from Rayleigh scattering, which states that the scattering intensity

is proportional to d^6/λ^4, where d is the particle diameter and λ is the wavelength, provided that d is smaller than λ. Compared with the scattering from the NPs, PTBs could potentially produce many orders of magnitude amplification in scattering intensity. As air bubbles grow larger, the effect of the particles enclosed diminishes, as can be seen on the 30-nm NP curves versus the 170-nm NS curves. For example, the scattering from a 600-nm bubble that encloses a 30-nm gold NP, and a 600-nm bubble that encloses a 170-nm gold NS gives a nearly identical value of scattered signal. When the bubble becomes comparable to or larger than a particular wavelength, this growth slows down significantly.

The modeling results obtained predict better scattering efficacy of the bubble compared with NPs, mainly owing to the increased diameter of the bubble. A probe of such a large diameter (up to 1 µm) cannot be delivered into the cell without compromising its viability, although it can be temporally generated in the cell for a short time, and possibly without causing damage to the cell.

■ Experimental results for water suspensions of NPs

Clustering of 30-nm NPs in water after adding 20% acetone was verified by optical scattering microscopy (FIGURE 4), and by comparing the extinction spectra of the suspensions (not shown). Clustering of NPs has caused an apparent broadening of the spectrum compared with that of nonclustered (single) NP suspensions. NP clusters were resuspended in water before the study commenced. We have obtained images of optical probe pulses scattered by single NPs (FIGURE 4A) and by NP clusters (FIGURE 4B) in the suspensions, and have measured local pixel amplitudes (TABLE 1). Also, we measured the amplitudes of integral scattered signals using a photodetector in parallel with a CCD camera (FIGURE 4D & E). Clustering of NPs has increased the amplitude of scattered light, as can be seen by comparing the images and corresponding integral signals in FIGURE 4A & D (single NPs) and FIGURE 4B & E (NP clusters). The optical amplification effect was quantified by normalizing the averaged amplitude values of the NP clusters' scattered signals (TABLE 1) with values obtained from the suspension of single NPs. In our experiment, the clustering of NPs has amplified the scattering by a factor of 2.3–2.4, which can be explained by the increased diameter of the clusters relative to those of the single NPs (30 nm). The values obtained for optical amplification were relatively small compared with what was expected from cluster size versus NP size increase, and from the six-power dependence of the scattering cross-section of the NP upon its size. This discrepancy might have been caused by the spatial averaging of a scattered signal by the photodetector and image sensor over the sample area, which was larger than the cluster size. Because the registered signal delivers the cumulative effect from a specific

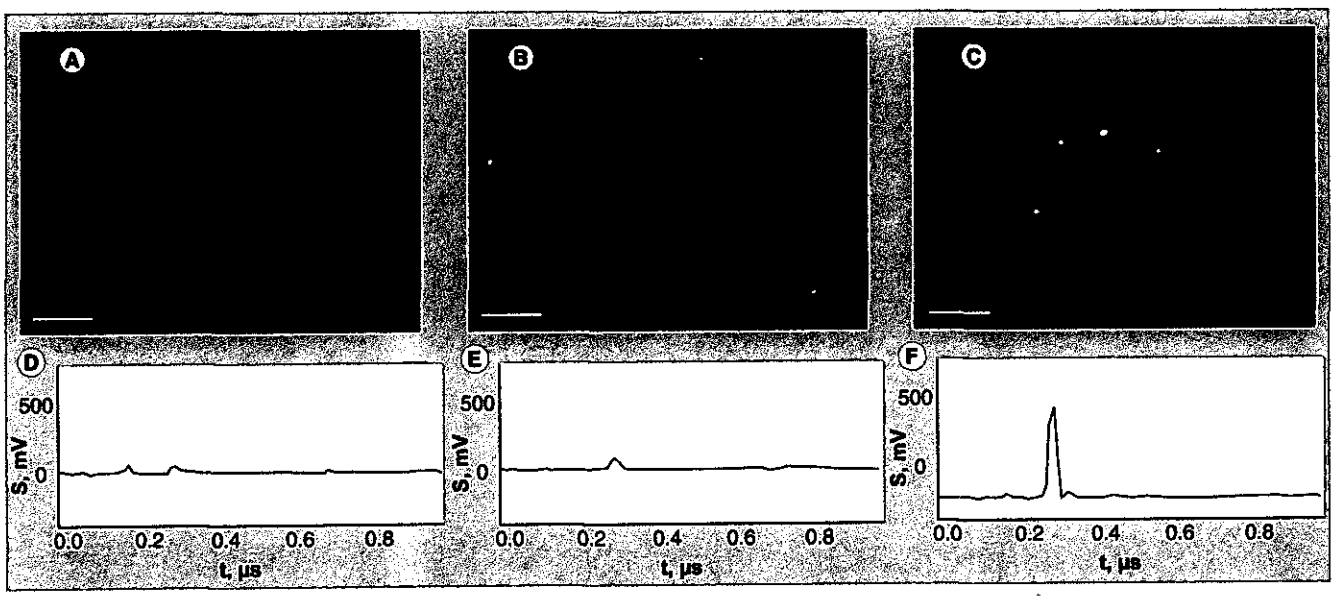

Figure 4. Optical detection of side scattering of the probe laser pulse by gold nanoparticles and photothermal bubbles. **(A–C)** Time-resolved images and **(D–F)** integral optical signals of the scattered probe pulse (750 nm, 10 ns). **(A & D)** Suspensions of 30-nm gold nanoparticles (NPs) with pump (532 nm, 10 ns) and probe laser pulses (at 150-ns delay time to pump pulse) applied (no photothermal bubbles were observed). **(B & E)** Suspension of the clusters of 30-nm gold NPs with no pump pulse applied or **(C & F)** with the pump pulse applied at a fluence of 0.45 J/cm². Scale bar: 10 µm.

Table 1. Averaged amplitudes of the scattered signals, obtained with a single probe optical pulse (750 nm, 10 ns) for a water suspension of 30-nm nanoparticles, their clusters and photothermal bubbles.

Source of optical scattered signal	Single NP suspension/ amplification factor	Suspension of NP clusters/ amplification factor	PTBs around single NPs/ amplification factor	PTBs around NP clusters/amplification factor
Image (pixel amplitude, counts)	231 ± 91/1.0	522 ± 289/2.3	220 ± 82/1.0 (no bubbles)	10780 ± 2876/47.6
Integral signal (mV)	21 ± 7/1.0	50 ± 12/2.4	20 ± 7/1.0 (no bubbles)	700 ± 120/33.3

NP: Nanoparticle; PTB: Photothermal bubble.

area (~2 μm² for the image sensor and 3–4 μm² for the integral scattering detector), the registered amplitudes of optical scattering increased more slowly than did the scattering from a cluster versus a single NP.

Next, the suspensions of NPs and their clusters were exposed to a single 10-ns pump laser pulse at 532 nm with a fluence of 0.45 J/cm². Exposure of the suspension of single nonclustered NPs to this laser pulse caused no change either in the scattered image (not shown) or in the integral signal. Figure 4D shows the two signals: the first peak is for the pump pulse and the second peak is for the probe pulse. The amplitude of the scattered probe pulse did not change (Table 1). When the suspension of NP clusters was exposed to the same pump pulse, we observed bright images of the PTBs (Figure 4C), with significantly increased image pixel amplitudes. The amplitude of the integral scattered signal has also increased (Figure 4F shows the pump- and probe-pulse signals). When considering a relatively rare spatial location of the clusters (their concentration was significantly lower than that for single NPs) and the single pump-pulse irradiation mode, we assume that single PTBs were generated and observed around single NP clusters. Comparing Figure 4B (clusters) with Figure 4C (PTBs), we have found far fewer PTBs (only four) than the clusters shown in Figure 4B. This can be explained by the strong dependence of PTB generation threshold fluence on cluster size: only the largest NP clusters have yielded PTBs. This is in line with our previous results in which the dependence of PTB generation threshold fluence on NP size and clustering was studied in detail [48–50]. Amplification of the scattered signal by PTBs after normalizing the image pixel amplitudes and the integral signal amplitude by the corresponding values obtained for single NPs was 47.6 (local amplification) according to images of individual bubbles, and 33.3 (averaged amplification) for the area probed with the photodetector (Table 1).

PTB generation was monitored independently and simultaneously with a thermal lens method. The signal detected (PT response) yielded a bubble-specific symmetrical shape (Figure 5B). PT response was obtained with an additional continuous probe laser at 633 nm, which was additionally registered by another photodetector. Its time course shows bubble expansion and collapse, and provides an estimation of bubble lifetime. In the case of NP cluster suspensions, we have detected a bubble-specific response (Figure 5B) with a duration of 250 ns. This bubble lifetime is longer than the delay of 150 ns of the probe pulse relative to the pump laser pulse, confirming that the images obtained with the delayed probe pulse (Figure 4C) were formed by PTBs. Also, the PT response obtained from the single-NP suspension (Figure 5A) under exposure to an equal pump-laser pulse showed no PTBs, which explains the absence of amplification of scattered light in single NP suspension. We gradually increased pump laser fluence until the PTBs were detectible in the single NP suspension; this level was approximately 17 J/cm². This fluence is significantly higher than the one applied to the NP clusters (0.45 J/cm²), which shows the difference between single NPs and their clusters in terms of PTB generation.

The results obtained clearly show that PTBs significantly amplify optical scattering, and that amplification with PTBs has a threshold nature: at a given fluence level of the pump laser pulse, no bubbles were generated around single NPs and there was no amplification of optical scattering from single NPs, while bubbles were generated around NP clusters at the same laser fluence. This demonstrated the selectivity of optical amplification with PTBs, which have provided almost 48-fold amplification of optical scattering amplitude around NP clusters only.

■ Scattering by PTBs in living cancer cells

The cluster–bubble mechanism of amplification of optical scattering was studied experimentally in three types of living cancer cells *in vitro*. NP

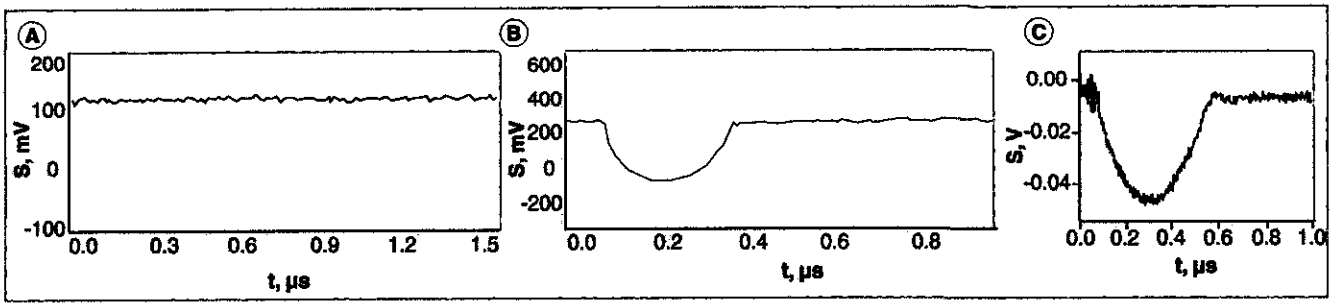

Figure 5. Photothermal responses obtained from gold nanoparticles and photothermal bubbles. Thermal lens signals (photothermal responses) obtained during exposure of the samples to a single 10-ns pulse at 532 nm: **(A)** suspension of 30-nm spherical gold nanoparticles (NPs; no bubble); **(B)** suspension of clusters of the same NPs; bubble duration 250 ns; **(C)** individual K562 cell treated with 30-nm gold NPs; bubble duration 380 ns.

clusters were formed in living cells by using nonspecific endocytosis. The suspensions (K562 leukemia-type cells) and monolayers (A549 and Hep-2C cells) of living cells were studied through the amplitude measurements of the integrally scattered signals from individual cells. Signals were obtained for intact, NP-treated and NP- and pump laser-treated cells. Gold 30-nm spheres were used in these experiments. All laser treatments and measurements were performed for individual cells and data were obtained for 150 cells in each population. Generation of the PTB in each individual cell was monitored simultaneously by the thermal lens method as in the aforementioned experiments with NP suspensions. This enabled the interpretation of the scattered signal for each cell during its exposure to the pump laser pulse: scattered signals were attributed to NP clusters when the PT response obtained independently from the same cell

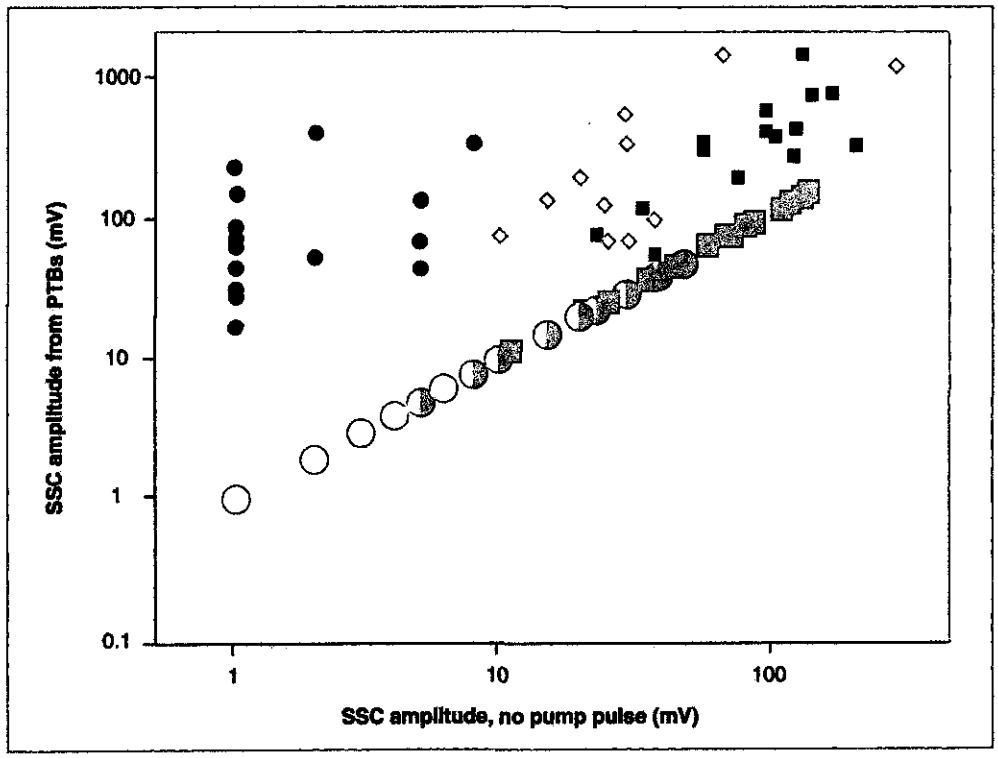

Figure 6. Optical side-scattering integral signals obtained from intracellular gold nanoparticles (X-axis) and from the photothermal bubbles (Y-axis). The amplitudes of integral scattering signals obtained from individual cancer cells, pretreated with 30-nm gold spherical NPs, and before and during exposure to a single pump laser pulse that generates PTBs around NP clusters in the living cells: Hep-2C with NP (large square), Hep-2C with PTB (small square), A549 with NP (large two-toned circle), A549 with PTB (small rhombus), K562 with NP (large circles) and K562 with PTB (small circle).
PTB: Photothermal bubble.

showed *no sign of* PTBs (X-axis, FIGURE 6), and the scattered signals were attributed to PTBs (Y-axis, FIGURE 6) when the PT response showed bubble-specific signals (FIGURE 5C). For each cell type, we have measured the amplitudes of the scattered probe pulse for the four samples: intact cells, intact cells exposed to the 10-ns pump laser pulse at 532 nm, NP-treated cells (cells with NP clusters) and NP-treated cells exposed to the pump laser pulse (TABLE 2). Optical amplification of PTBs was quantified relative to the scattering of NPs in the same cells.

During the experiments, we adjusted the fluence of the pump laser to the level at which PTBs were generated in 100% of NP-treated cells (TABLE 2). These fluencies varied slightly for the different types of cells; this may reflect differences in the efficacy of cluster formation (caused by the different efficacy of the endocytosis) in the different types of cells. For each individual cell, we registered a pair of amplitudes of integral scattering signal: before cell irradiation with a pump laser pulse (to characterize NP-related scattering) and during cell irradiation with a pump laser pulse having a fluence above the PTB generation threshold (to characterize PTB-related scattering). These two scattering signals were plotted in a diagram, in which each dot represents an individual cell (FIGURE 6). This diagram shows a distinct line for 'no PTB' cases. All dots that are above this line correspond to PTBs.

According to the results obtained for all three types of cells, NPs amplify the scattering, but not significantly relative to the scattering by intact cells (TABLE 2). Also, differences in the amplitudes of an integral scattering signal (X-axis, FIGURE 6) indicate the differences in cluster size among the three types of cells studied. The smallest signals were observed for K562 suspension-type cells, and the highest scattered signals were observed for the squamous carcinoma Hep-2C cells (FIGURE 6; TABLE 2). PTBs yielded a significant increase of scattered signal amplitudes in *all studied cells* (FIGURE 6; TABLE 2). Amplification factors were calculated by normalizing the measured amplitudes by those measured for the intact cells (TABLE 2). For some specific individual cells in the population, the amplification factor of the integral signal was more than 100 relative to NP scattering. Owing to the heterogeneous nature of cellular properties, the amplification effect was also rather heterogeneous. The higher the NP cluster-related signal, the higher the PTB-related signal. This correlation is in line with physical mechanisms that are involved in PTB generation: the larger the cluster, the larger the bubble.

The imaging potential of PTBs was evaluated in detail for A549 cells incubated with 170-nm NSs. We have *studied the influence* of PTBs on two main properties of the proposed imaging method: amplification of optical scattering and cell viability. This was achieved by registering and comparing the several optical images for each cell. Cell viability was evaluated optically with two standard microscopy techniques that monitor the integrity of the outer cellular membrane [63]. First, a white light transmittal image was obtained for the cell before and after its exposure to the pump pulse, and the difference between these two images was used to detect any PTB-induced cell shape changes. The coefficient of variation of pixel amplitude K_{wl} of the white light differential image indicated a significant alteration of cell shape and size (which *usually accompanies* a disruption of the cellular membrane) if its value deviated significantly from zero. Second, cell damage by PTB was detected by monitoring the cellular uptake of ethidium bromide (EtBr). Before the experiment, EtBr was added to the cell samples. This dye penetrates the membranes of compromised cells and produces red fluorescence; however, EtBr does not penetrate the membranes of

Table 2. Amplitude of the integral optical scattering signal (mV) averaged for cell populations (mV) for intact cells, nanoparticle-treated cells with 30-nm gold spheres and photothermal bubbles generated by a single short pulse (532 nm, 10 ns) in individual living cells.

Cancer cell types	Intact cells	Cells treated with single pump laser pulse	NP-treated cells	Cells treated with NPs & single pump laser pulse	Fluence of pump laser pulse (532 nm, 10 ns; J/cm²)
Hep2C (squamous carcinoma cell)	68.8 ± 41.6	61.5 ± 48.2/1.0	95.2 ± 62.8/1.4	454 ± 420/6.6	1.3
A549 (lung cancer cell)	20.8 ± 14.3	19.4 ± 12.6/1.0	36.8 ± 58.8/1.8	338 ± 465/17	1.3
K562 (acute leukemia cell)	2.4 ± 1.42	2.4 ± 1.85/1.0	2.4 ± 2.3/1.0	106 ± 111/44	1.9

NP: Nanoparticle.

living cells and hence produces no fluorescence for living cells. For excitation of the fluorescence, we used a single pump pulse (532 nm) with the fluence decreased by 20 times relative to PTB-generation level. Fluorescent images were obtained for each cell before and after PTB generation. Their pixel amplitude ratio was used to quantify the damage: any significant increase of the fluorescence amplitude in the time gap 50–100 *s* after the generation of PTBs was interpreted as cell damage.

Side-scattering images where obtained before and during the pump pulse with the pulsed probe laser at 750 nm. The former characterized scattering owing to NS, NS clusters and to cellular endogenous structures, and the latter characterized PTB-related scattering. A second scattering image was normalized by the first one and the pixel amplitude of the ratio image (K_{ssc}) was considered as the scattering amplification coefficient. It was applied to the image points where the PTBs were detected and was used to quantify the amplification of the scattering by PTBs relative to that related to NSs:

$$K_{ssc} = \frac{(A_{PTB} - B)}{(A_{cl} - B)}$$

where A_{PTB} and A_{cl} are the pixel image amplitudes obtained for the same cell in pulsed mode of scattering for the PTB (pump laser on) and NS (pump laser off), respectively, and B is the constant for the background amplitude. We used, in total, five experimental parameters for each cell: pump laser fluence, white light image ratio, fluorescent image ratio, side-scattering image ratio (as the PTB amplification measure) and the PT response duration (as the PTB lifetime measure).

Influence of the PTBs on optical scattering signal and cell viability is illustrated in Figure 7 & Table 3. The figures and table show data for the two A549 living cells that were exposed to single pump pulses with fluencies of 0.64 J/cm^2 (cell 1, top panel of Figure 7) and 0.48 J/cm^2 (cell 2, bottom panel of Figure 7). According to the scattering images (Figure 7C) and corresponding PT responses, both cells have yielded submicrometer-sized intracellular PTBs and with PTB durations of 250 ns for cell 2 and 70 ns for cell 1. Both cells have yielded single PTBs, which can be explained by inefficient nonspecific endocytosis of 170-nm NSs by those cells. In general, eight to ten PTBs in individual cells have been observed, and their number increased when pump laser fluence was increased. This was owing to the (aforementioned) dependence of the PTB threshold fluence on cluster size: the larger the cluster, the lower the PTB generation threshold. Cluster size, in turn, depends on the efficacy of endocytosis. Under the given fluence levels, these two cells only yielded a single PTB around the largest NS clusters. Laser-induced PTBs (Figure 7C) have caused an increase of optical scattering by almost three orders of magnitude

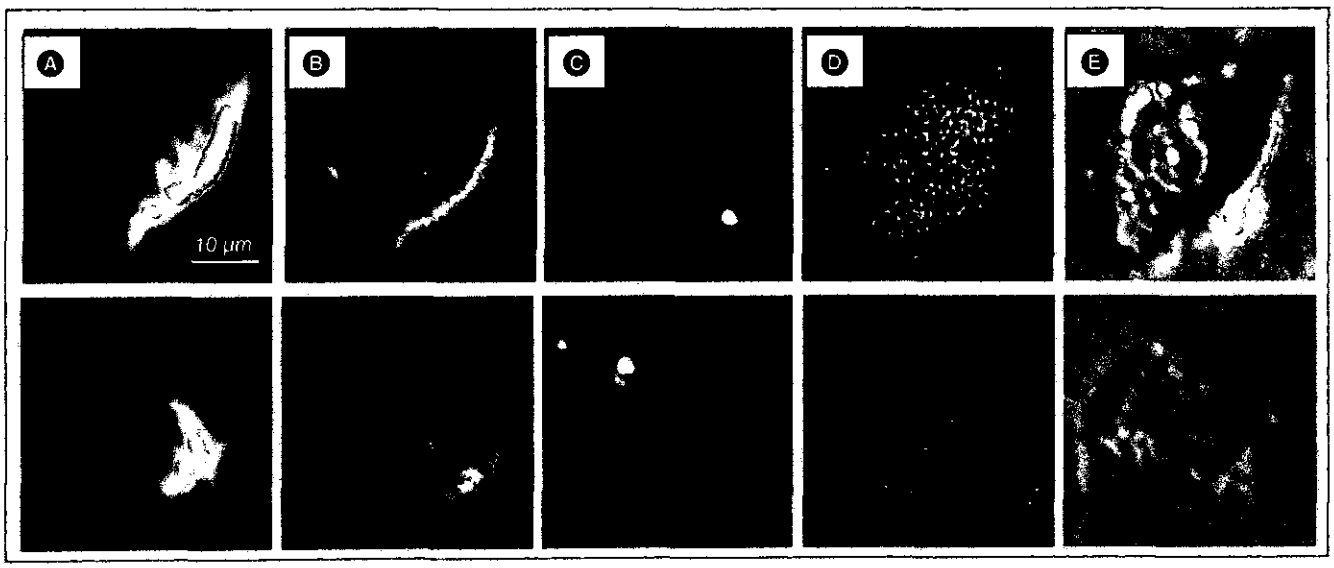

Figure 7. Images of damaged (top panel) and living (bottom panel) A549 cells after their incubation with 170-nm gold nanoshell and the follow-up exposure to a single pump laser pulse that induced photothermal bubbles. (A) White light image prior to exposure to pump laser pulse; **(B)** Side-scattering image prior to exposure to pump laser pulse shows nanoshell-related signals; **(C)** Side-scattering image during exposure to pump laser pulse shows photothermal bubbles; **(D)** Fluorescent image after the exposure to pump laser pulse shows ethidium bromide fluorescence; **(E)** Differential white light image shows the changes in the cell after exposure to a pump laser pulse.

Table 3. The ratios of the image pixel amplitudes for images of two individual A549 cells: damaged and living after incubation with gold nanoshells, and follow-up exposure to a single laser pulse (10 ns, 532 nm) that has generated photothermal bubbles in the cells.

Parameter	K_{ssc}	Relative change of pixel amplitude of ethidium bromide fluorescence	K_w
Source of the image	Side scattering	Fluorescence	White-light transmittance
Damaged cell	2886	3.4	0.46
Survived cell	1779	0.7	0.05

K_{ssc}: Coefficient of amplification of optical side scattering; K_w: Relative difference in pixel amplitudes of the transmitted optical images.

(TABLE 3) relative to the scattering of gold NSs in the same point of the image (FIGURE 7B). Analysis of fluorescent and white light images has shown that cell 1 was damaged by the PTB because its fluorescence has increased (FIGURE 7D, top), and its shape changed significantly (FIGURE 7E, top). Under the lower pump laser fluence, cell 2 survived the pump pulse and PTB: no increase in fluorescence (FIGURE 7D, bottom) nor change in cell shape (FIGURE 7E, top) was detected. PTB lifetime in the surviving cell was shorter than that for a damaged cell, and this difference shows that the maximal diameter of the PTB in the surviving cell was smaller than that for a damaged cell.

Of course, the viability of cells after generation of intracellular PTBs should be verified with a more sensitive method than EtBr staining. Also, the mechanism of selective NS cluster formation around single target molecules has to be studied for receptor-mediated endocytosis of the NPs preconjugated with cell-specific vectors (such as monoclonal antibody C225 for solid tumor cells). Nevertheless, the results obtained found that the cluster–bubble mechanism has provided amplification of optical scattering in living cells by more than 1000-times; PTBs have acted as noninvasive cellular optical probes.

Next, we studied the dependence of the image pixel amplitude of scattered light on the incident fluence of the pump laser pulse and the size of NPs (FIGURE 8). We incubated the A549 cancer cells with gold spheres with a diameter of 30 nm and with gold NSs with a diameter of 170 nm. We obtained the scattering amplification coefficient and PTB lifetimes as cell population-averaged values for several different laser fluences. Then, we analyzed the scattering amplification coefficient, K_{sc}, as a function of PTB lifetime. We consider that the bubble lifetime characterizes the PTB more precisely than pump pulse fluence. First, PTB lifetime is proportional to the maximal diameter of the PTB [58], which relates directly to the scattering efficacy of the PTB; second, the generation of the PTBs is provided by several factors, with laser fluence being only one of them. The other important factor that influences PTB diameter and lifetime is the clustering of NPs. The increase of pump laser fluence from 0.5 to 3.5 J/cm^2 has caused steady increase of PTB lifetime (not shown) and of the image pixel amplitude of the scattered signal. We plotted both parameters as cell population-averaged values (FIGURE 8). The increase of PTB lifetime (or maximal diameter) causes an increase in optical scattering. Also, experimental data presented in FIGURE 8 correlate with the results of theoretical modeling, as shown in FIGURE 3. Both theoretical and experimental results indicate that the amplification of optical scattering depends on PTB size (lifetime), and does not depend on NP size when the PTB diameter exceeds 300–400 nm or the PTB lifetime exceeds 200 ns. Thus, the NP diameter does not influence PTB scattering significantly, at least when PTB diameter significantly exceeds the size of the NPs. Additionally, a possible explanation for the absence of a significant difference between the amplitudes of optical scattering provided by 30-nm spheres and 170-nm shells is the clustering of those NPs in the cells: PTBs are generated mainly around the biggest NP clusters, which may be similar in size, although the sizes of the NS and NP are significantly different. It should be noted that the large diameter of gold NSs (170 nm) might not improve scattering owing to poor internalization (and hence clustering) of such large NPs by the cell. Much smaller spheres were better internalized (and clustered) by the cells. This resulted in the relatively similar scattering amplitudes obtained from the cells after their incubation with big NSs and small nanospheres. Therefore, we may conclude that PTB size, not NP size, is important for the amplification of optical scattering, and that NP clustering enables us to improve PTB diameter.

Discussion

■ Amplification of optical scattering with PTBs

There are several basic factors that influence the effect of optical amplification by PTBs. The *in vitro* experimental results have demonstrated

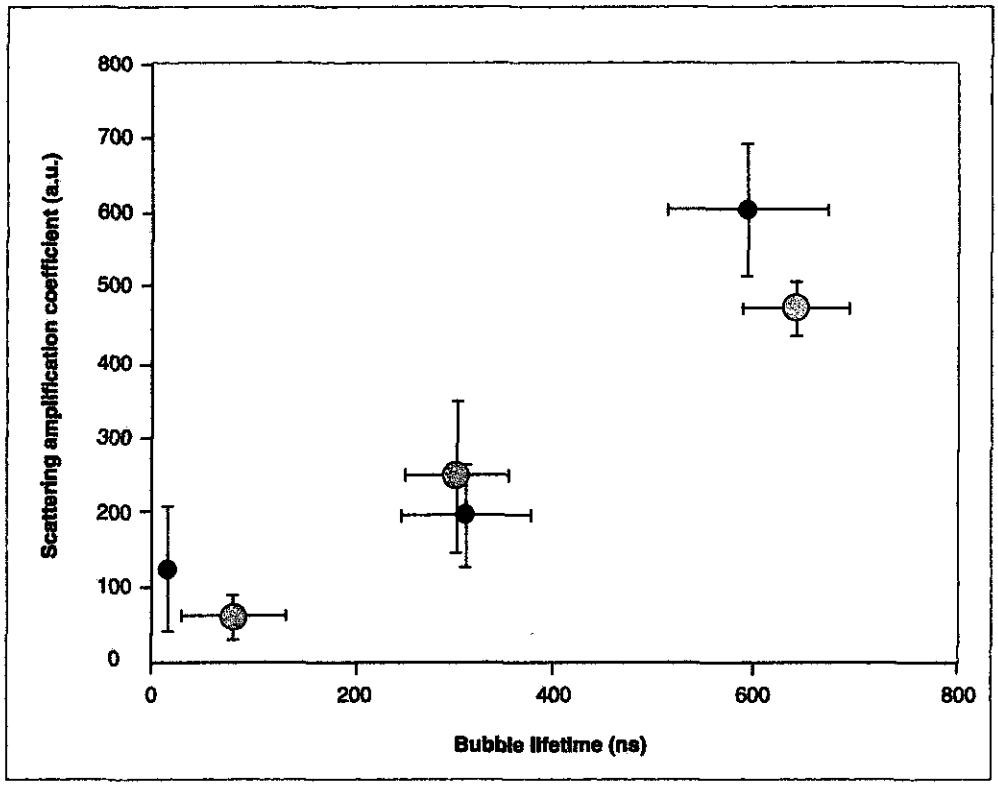

Figure 8. Influence of the photothermal bubble lifetime on the amplification of optical scattering. *Experimental dependence of optical scattering amplification coefficient* upon the lifetime of the intracellular photothermal bubbles: large circle for 30-nm gold spheres, small circle for 170-nm gold nanoshells. Population-averaged data are given for A549 cells exposed to a single 10-ns pump pulse at 532 nm.

that a NP cluster generates a much larger PTB than a single NP does under the same laser pulse fluence. This effect and its mechanisms were studied by us previously [48–50]. Under equal laser pulse fluence, the lifetime and maximum diameter of the PTB increase significantly with an increase in NP diameter [30,50]. The larger NPs have high absorbance cross-sections and release more thermal energy, thus expanding the PTB to a larger size. Thus, the increased optical absorbance and diameter of the NP cluster increase the maximum diameter of PTBs, and so contribute to an amplification of optical scattering. Next, for a given NP cluster, the increase of the pump laser fluence also increases the PTB diameter and lifetime (these two PTB parameters are proportional to each other [58]) owing to the increase of the initial laser-induced temperature of the NPs. Finally, scattering can be amplified through an increase of the probe laser fluence, providing that it is safe for the cell.

Besides these three factors that we have considered experimentally, there are several others that also influence PTB size and hence the optical scattering signal. The initial laser-induced temperature also depends on heat loss from the thermal diffusion of heated NPs and from the PTB nuclei. This heat loss into the surrounding media can be alleviated by shortening the length of the laser pulse (10 ns in our experiments). In experiments with picosecond laser pulses, the efficacy of PTB generation was higher compared with that of nanosecond pulses [64]. The initial laser-induced temperature and the laser fluence are limited by two damage thresholds: the threshold of thermal damage for the cell components and the threshold of thermal damage of the NP. Although the thermal damage threshold of cellular molecules may be much lower than the temperatures required for PTB generation, actual thermal damage to the cell can be minimized by localization of the PT effect to the size of the NP cluster and inside the PT bubble. There may be several independent ways of controlling the size and duration of PTBs: through NP properties (NP cluster diameter, absorbance cross-section of individual NPs and laser fluence threshold of NP damage), laser-pulse parameters (duration and fluence of a single laser pulse, and fluence, number and interval for the sequence [train] for several pulses [62]) and through the frequency and amplitude of ultrasound that is applied simultaneously with laser

irradiation. Experimental studies of the influence of these factors on the optical amplification is the subject of our ongoing and future work.

Cell imaging

When PTBs are generated in living cells, viability becomes the most significant factor, and the parameters of the PTB, laser and acoustic radiation must be below cell damage thresholds. This requirement limits the maximal amplitude of optical signal and leads to questions about the signal-to-noise ratio. The source of noise is the scattering from cellular components and tissues (when being carried out *in vivo*). The balance of sensitivity and safety depends not only on PTB-generation factors that were previously considered, but also on the optical scattering properties of specific cells, which is beyond the scope of this article. Nevertheless, the transient nature of the PTB significantly improves the signal-to-noise ratio: the scattered signal amplitude follows the dynamics of PTB radius and, therefore, the PTB can be recognized at specific time domains owing to the specific symmetrical time contour of the optical signal (Figure 5B & C), even in a highly scattering environment.

The generation of laser- and ultrasound-induced bubbles has already been studied in terms of the mechanical damage of cellular outer membranes [33,34]. A cell may repair its membrane if the maximal diameter of the bubble does not exceed 1–2 µm. Optical scattering of a vapor PTB of a 1-µm diameter is several orders of magnitude stronger than optical scattering of the gold NPs that can be delivered into cells (Figure 4). Recent results demonstrating the level of optical scattering from gold NPs in living and fixed cells have shown that scattering from gold NPs is detectable, although it may require many NPs [65–67]. These results, together with our present results, enable prediction of a considerable increase of the sensitivity of scattering imaging owing to PTBs.

When several different cells produce similar PTBs, all those cells viewed through PTB scattering will look alike. An additional way to increase the specificity of optical scattering and so enable differentiation of those cells is to detect an additional signal scattered by NP clusters before PTB generation. The difference in NP cluster scattering can be seen clearly for the three types of cancer cells presented in Figure 6. This difference is caused by different sizes of NP clusters in the three different cell types. However, without a pump laser pulse when no PTB is generated, the difference in cluster scattering is not sufficient, combined with the relatively low scattering signal, and does not provide reliable differentiation among the three groups of cells. Only when the PTB-related signal can be obtained does the difference among cell populations become clear. Therefore, sensitive and specific scatter imaging should combine the two images or the two optical signals. The first image is obtained with probe laser alone and the second image is obtained immediately after the first, by applying pump and probe pulses. With short nanosecond laser pulses, both signals can be acquired in 100 ns. Cluster signals and the second PTB signals can be registered with one photodetector and one probe laser.

The suggested method differs from current optical scattering methods by the double-signal principle. This method may also provide an increase in the signal-to-noise ratio when the target cell or molecule is located among a highly scattered background. The latter is typical for *in vivo* imaging, and thus the suggested method may also improve the efficacy of optical endoscopy. PTBs can be generated inside specific living cells and provide a maximal refractive index gradient that improves optical scattering. Small laser-induced PTBs generated around NP clusters may be safe for the cells, and can be used for the stimulated release of the molecular probes from endosomes and optical imaging of specific single molecules. PTB size can be much larger than that of a single molecule or the other cellular target. Nevertheless, the origin of the PTB can be linked to a specific target molecule through vector-based bonds between NPs that generate the PTB and the molecule. Thus, the suggested method may provide efficient imaging of single intracellular molecules in living cells. The size of the PTB image (up to one µm) may exceed the actual size of the target (the latter may be a size that is well below the diffraction limit), but the PTB would definitely help to detect the presence of such a target as the single molecule in a specific cell.

Our experimental results also suggests that PTB scattering can be applied in cytometry for detecting specific cells. Unlike fluorescent probes, the PTBs do not exist in the cell until after they are generated, and the gold NPs that are present in the cell are much less toxic than any fluorescent probes. Therefore, the influence of PTB imaging on physiological cell processes can be minimized. The threshold mechanism of PTB generation provides selectivity of optical signal, and thus increases the signal-to-noise ratio of imaging. PTBs can be activated with a specific wavelength and energy of a laser pulse,

otherwise they do not emerge in a cell, so they would not interfere with cellular processes and other measurements.

Conclusions

In this work, we have experimentally verified that:

- Optical scattering from metal light-absorbing NPs may be amplified by more than three orders of magnitude by generating PTBs around these NPs;
- Clustering of the NPs around specific molecular targets may significantly improve the specificity of scattering imaging;
- PTBs as cellular optical probes can be used without causing damage to the cell in which they are generated;
- Two-signal scattering method with time-domain detection of the PTBs may significantly enhance the specificity and sensitivity of the imaging of specific targets.

Future perspective

The universal nature of PTB probes and scattering imaging may enable their applications in microscopy, flow cytometry, endoscopy and other optical methods. Bubble-imaging methods can be applied for optical guidance of therapeutic processes, whereby the bubbles occur as primary or secondary phenomena (in particular, in laser and ultrasound methods). The nontoxic properties of gold NPs, an on-demand feature of the bubbles, may provide noninvasive monitoring and screening of living cells *in vitro* and *in vivo*.

Financial & competing interests disclosure

R Drezek acknowledges support from DOD W81XWH-07-1-0428, Welch C-1598, NSF EEC 0647452 and the John and Ann Doer Fund for Computational Biomedicine. D Lapotko has received support for part of this work from the Institute of International Education/SRF (NY, USA). The authors have no other relevant affiliations or financial involvement with any organization or entity with a financial interest in or financial conflict with the subject matter or materials discussed in the manuscript apart from those disclosed.

No writing assistance was utilized in the production of this manuscript.

Ethical conduct of research

The authors state that they have obtained appropriate institutional review board approval or have followed the principles outlined in the Declaration of Helsinki for all human or animal experimental investigations. In addition, for investigations involving human subjects, informed consent has been obtained from the participants involved.

Executive summary

- Laser-induced vapor microbubbles (photothermal bubbles) when being generated in a living cell with a short laser pulse and around gold nanoparticles (or their clusters) significantly improved the optical scattering (up to three orders of magnitude) relative to that of gold nanoparticles.
- Combination of the intracellular clustering of gold nanoparticles around specific target molecules with the ability of nanoparticle clusters to selectively generate on-demand microbubbles may enable highly sensitive and noninvasive imaging of specific cellular targets and events in living cells.

Bibliography

1 Hu M, Chen J, Li Z-Y *et al.*: Gold nanostructures: engineering their plasmonic properties for biomedical applications. *Chem. Soc. Rev.* 35(11), 1084–1094 (2006).

2 Oberdorster G, Oberdorster E, Oberdorster J: Nanotoxicology: an emerging discipline evolving from studies of ultrafine particles. *Environ. Health Perspect.* 113(7), 823–839 (2005).

3 Lewinski N, Colvin V, Drezek R: Cytotoxicity of nanoparticles. *Small* 4(1), 26–49 (2008).

4 Gelles J, Schnapp BJ, Sheetz MP: Tracking kinesin-driven movements with nanometre-scale precision. *Nature* 331(6155), 450–453 (1988).

5 Yguerabide J, Yguerabide EE: Light-scattering submicroscopic particles as highly fluorescent analogs and their use as tracer labels in clinical and biological applications. II. Experimental characterization. *Anal. Biochem.* 262(2), 157–176 (1998).

6 El-Sayed IH, Huang X, El-Sayed MA: Surface plasmon resonance scattering and absorption of anti-EGFR antibody conjugated gold nanoparticles in cancer diagnostics: applications in oral cancer. *Nano Lett.* 5(5), 829–834 (2005).

7 Loo C, Lowery A, Halas N, West J, Drezek R: Immunotargeted nanoshells for integrated cancer imaging and therapy. *Nano Lett.* 5(4), 709–711 (2005).

8 West JL, Halas NJ: Engineered nanomaterials for biophotonics applications: improving sensing, imaging, and therapeutics. *Annu. Rev. Biomed. Eng.* 5, 285–292 (2003).

9 Tkachenko AG, Xie H, Liu Y *et al.*: Cellular trajectories of peptide-modified gold particle complexes: comparison of nuclear localization signals and peptide transduction domains. *Bioconjug. Chem.* 15(3), 482–490 (2004).

10 Yang PH, Sun X, Chiu JF, Sun H, He QY: Transferrin-mediated gold nanoparticle cellular uptake. *Bioconjug. Chem.* 16(3), 494–496 (2005).

11 Farokhzad OC, Jon S, Khademhosseini A, Tran TNT, LaVan DA, Langer R: Nanoparticle-aptamer bioconjugates: a new approach for targeting prostate cancer cells. *Cancer Res.* 64(21), 7668–7672 (2004).

12 Sönnichsen C, Geier S, Hecker NE *et al.*: Spectroscopy of single metallic nanoparticles using total internal reflection microscopy. *Appl. Phys. Lett.* 77(19), 2949–2951 (2000).

13 Sokolov K, Follen M, Aaron J *et al.*: Real-time vital optical imaging of precancer using anti-epidermal growth factor receptor antibodies conjugated to gold nanoparticles, *Cancer Res.* 63(9), 1999–2004 (2003).

14 Siiman O, Gordon K, Burshteyn A, Maples J, Whitesell J: Immunophenotyping using gold or silver nanoparticle-polystyrene bead conjugates with multiple light scatter. *Cytometry* 41(4), 298–307 (2000).

15 Nammalvar V, Wang A, Drezek R: Enhanced gold nanoshell scattering contrast in cervical tissue using angled fiber probes. *Proc. SPIE* 6447, 64470H (2007).

16 Hartland G: Measurements of the material properties of metal nanoparticles by time-resolved spectroscopy. *Phys. Chem. Chem. Phys.* 6(23), 5263–5274 (2004).

17 Mohamed MB, Ahmadi TS, Link S, Braun M, El-Sayed MA: Hot electron and phonon dynamics of gold nanoparticles embedded in a gel matrix. *Chem. Phys. Lett.* 343(1–2), 55–63 (2001).

18 Link S, Hathcock DJ, Nikoobakht B, El-Sayed MA: Medium effect on the electron cooling dynamics in gold nanorods and truncated tetrahedral. *Adv. Mater.* 15(5), 393–396 (2003).

19 Rosencwaig A: High-resolution photoacoustic thermal-wave microscopy. *Appl. Phys. Lett.* 36(9), 725–727 (1980).

20 Tam AC: Photothermal investigation of solids and fluids. In: *Overview of Photothermal Spectroscopy.* Sell JA (Ed.). Academic Press, Boston, USA 1–34 (1988).

21 Shibata MM, Kitamori T, Sawada T: Application of coaxial beam photothermal microscopy to the analysis of a single biological cell in water. *Anal. Chim. Acta* 299(3), 343–347 (1995).

22 Cretin B, Daher N, Cavallier B: Thermoelastic modeling: application to superresolution in photothermal and thermoelastic microscopy. *Proc. SPIE* 3098, 466–475 (1997).

23 Boyer D, Tamarat P, Maali A, Lounis B, Orrit M: Photothermal imaging of nanometer-sized metal particles among scatterers. *Science* 297(5584), 1160–1163 (2002).

24 van Dijk MA, Tchebotareva AL, Orrit M *et al.*: Absorption and scattering microscopy of single metal nanoparticles. *Phys. Chem. Chem. Phys.* 8(30), 3486–3495 (2006).

25 Wang FS, Jay DG: Chromophore-assisted laser inactivation (CALI): probing protein function *in situ* with a high degree of spatial and temporal resolution. *Trends Cell. Biol.* 6(11), 442–445 (1996).

26 Seol Y, Carpenter A, Perkins T: Gold nanoparticles: enhanced optical trapping and sensitivity coupled with significant heating. *Optics Lett.* 31(16), 2429–2431 (2006).

27 Doukas AG, Flotte TJ: Physical characteristics and biological effects of laser-induced stress waves. *Ultrasound Med. Biol.* 22(2), 151–164 (1996).

28 Lee S, Anderson T, Zhang H, Flotte TJ, Doukas AG: Alteration of cell membrane by stress waves *in vitro*. *Ultrasound Med. Biol.* 22(9), 1285–1293 (1996).

29 Pitsillides CM, Joe EK, Wei X, Anderson RR, Lin CP: Selective cell targeting with light absorbing microparticles and nanoparticles. *Biophys. J.* 84(6), 4023–432 (2003).

30 Gerstman BS, Thompson CR, Jacques SL, Rogers ME: Laser-induced bubble formation in the retina. *Lasers Surg. Med.* 18(1), 10–21 (1996).

31 Jacques SL, McAuliffe DJ: The melanosome: threshold temperature for explosive vaporization and internal absorption coefficient during pulsed laser irradiation. *Photochem. Photobiol.* 53(6), 769–775 (1991).

32 Huttmann G, Birngruber R: On the possibility of high-precision optothermal microeffects and the measurement of fast thermal denaturation of proteins. *IEEE J. Select Topics Quant. Electron* 5, 954–962 (1999).

33 Anderson RR, Parrish JA: Selective photothermolysis: precise microsurgery by selective absorption of pulsed radiation. *Science* 220(4596), 524–527 (1983).

34 Roegener J, Brinkmann R, Lin CP: Pump-probe detection of laser-induced microbubble formation in retinal pigment epithelium cells. *J. Biomed. Opt.* 9(2), 367–371 (2004).

35 Lapotko D, Kuchinsky G, Romanovskaya T, Scoromnik H: Photothermal method for cell viability control. In: *Photoacoustica and Photothermal Phenomena.* Scudiery F, Bertolotti M (Eds). AIP, Rome, Italy 582–584 (1998).

36 Lapotko D, Shnip A, Lukianova E: Photothermal detection of laser-induced damage in single intact cells. *Lasers Surg. Med.* 33(5), 320–329 (2003).

37 Hansen GM: Mie scattering as a technique for the sizing of air bubbles. *Applied Optics* 24(19), 3214–3220 (1985).

38 Jeon J-S, Yang I-J, Karng S-W, Kwak H-Y: Radius measurement of a sonoluminescing gas bubble. *Jpn J. Appl. Phys.* 39(3A), 1124–1127 (2000).

39 Zhu Q, Chance B, Jenkins WT, Zhang Y: Enhanced optical scattering by microbubbles. *Proc. SPIE* 2979, 157–162 (1997).

40 Kozuka T, Hatanaka S, Yasui K, Tuziuti T, Mitome H: Simultaneous observation of motion and size of a sonoluminescing bubble. *Jpn J. Appl. Phys.* 41(5B), 3248–3249 (2002).

41 Auger JC, Barrera RG, Stou B: Optical properties of an eccentrically located pigment within an air bubble. *Prog. Organic Coatings* 49(1), 74–83 (2004).

42 Kokhanovsky AA: Optical properties of bubbles. *J. Opt. A Pure Appl. Opt.* 5(1), 47–52 (2003).

43 Yavas O, Leiderer P, Park HK: Optical reflectance and scattering studies of nucleation and growth of bubbles at a liquid-solid interface induced by pulsed laser heating. *Phys. Rev. Lett.* 70(12), 1830–1833 (1993).

44 Stevenson D, Agate B, Tsampoula X *et al.*: Femtosecond optical transfection of cells: viability and efficiency. *Optics Express* 14(16), 7125–7133 (2006).

45 Schlicher RK, Radhakrishna H, Tolentino TP, Apkarian RP, Zarnitsyn V, Prausnitz MR: Mechanism of intracellular delivery by acoustic cavitation. *Ultrasound Med. Biol.* 32(6), 915–924 (2006).

46 Ohl CD, Wolfrum B: Detachment and sonoporation of adherent HeLa cells by shock wave-induced cavitation. *Biochim. Biophys. Acta* 1624(1–3), 131–138 (2003).

47 Prentice P, Cuschieri A, Dholakia K, Prausnitz M, Campbell P: Membrane disruption by optically controlled microbubble cavitation. *Nat. Physics* 1(2), 107–110 (2005).

48 Lapotko D, Lukianova E, Potapnev M, Aleinikova O, Oraevsky A: Method of laser activated nanothermolysis for elimination of tumor cells. *Cancer Lett.* 239, 36–45 (2006).

49 Lapotko D, Lukianova-Hleb E, Oraevsky A: Clustering of nanoparticles during their interaction with living cells. *Nanomed.* 2(2), 241–253 (2007).

50 Lapotko D, Lukianova E, Oraevsky A: Selective laser nano-thermolysis of human leukemia cells with microbubbles generated around clusters of gold nanoparticles. *Lasers Surg. Med.* 38(6), 631–642 (2006).

51 Lapotko D, Lukianova-Hleb E, Hafner J: Nanocluster-bubble photothermal nanotechnology for anti-cancer applications. *Proc. SPIE* 6734, 67340E (2007).

52 Chan WCW, Chithrani BD, Ghazani AA: Determining the size and shape dependence of gold nanoparticle uptake into mammalian cells. *Nano Lett.* 6(4), 662–668 (2006).

53 Chan WCW, Chithrani BD: Elucidating the mechanism of cellular uptake and removal of protein-coated gold nanoparticles of different sizes and shapes. *Nano Lett.* 7(6), 1542–1550 (2007).

54 Lapotko D, Hleb E, Zhdanok S *et al.*: Photothermolysis by laser-induced microbubbles generated around gold nanorod clusters selectively formed in leukemia cells, *Proc. SPIE* 6856, 68560K (2008).

55 Lapotko D, Lukianova-Hleb E, Mitskevich P *et al.*: Photothermal and photoacoustic processes of laser activated nano-thermolysis of cells. *Proc. SPIE* 6437, 64370C (2007).

56 Loo C, Lowery A, Halas N, West J, Drezek R: Immunotargeted nanoshells for integrated cancer imaging and therapy. *Nano Lett.* 5(4), 709–711 (2005).

57 Lapotko D, Kuchinsky G: Optothermal microscope In: *Photoacoustica and Optothermal Phenomena*. Scudiery F, Bertolotti M (Eds). AIP, Rome, Italy 184–186 (1998).

58 Lapotko D, Lukianova K, Shnip A: Photothermal responses of individual cells. *J. Biomed. Opt.* 10(1), 014006 (2005).

59 Lapotko D, Lukianova E, Potapnev M, Aleinikova O, Oraevsky A: Elimination of leukemic cells from human transplants by laser nano-thermolysis. *Proc. SPIE* 6086, 135–142 (2006).

60 Lapotko D, Lukianova K: Laser-induced micro-bubbles in cells. *Int. J. Heat Mass Trans.* 48(1), 227–234 (2005).

61 Lapotko D: Laser-induced bubbles in living cells. *Lasers Surg. Med.* 38(3), 240–248 (2006).

62 Hleb E, Lapotko D: Photothermal properties of gold nanoparticles under exposure to high optical energies. *Nanotechnology* 19(35), 355702 (2008).

63 Rost FWD: Applications of microfluorometry. In: *Quantitative Fluorescence Microscopy*. Cambridge University Press, UK 250 (1991).

64 Francois L, Mostafavi M, Belloni J, Delaire J: Optical limitation induced by gold clusters: mechanism and efficiency. *Phys. Chem. Chem. Phys.* 3(22), 4965–4971 (2001).

65 Drezek R, Faupel M, Pitris C *et al.*: Optical imaging for the detection of cervical precancers *in vivo*. *Cancer* 98(Suppl. 9), 2015–2027 (2003).

66 Jain PK, El-Sayed IH, El-Sayed MA: Au nanoparticles target cancer. *Nano Today* 2(1), 18–29 (2007).

67 Sokolov K, Aaron J, Hsu B *et al.*: Optical systems for *in vivo* molecular imaging of cancer. *Techn. Cancer Res. Treat.* 2(6), 491–504 (2003).

Optical properties of gold-silica-gold multilayer nanoshells

Ying Hu,[1] **Ryan C. Fleming,**[1] **and Rebekah A. Drezek**[1,2]

[1]*Department of Bioengineering,* [2]*Department of Electrical and Computer Engineering, Rice University, Houston, TX 77005*

hooying@rice.edu

Abstract: The spectral and angular radiation properties of gold-silica-gold multilayer nanoshells are investigated using Mie theory for concentric multilayer spheres. The spectral tunability of multilayer nanoshells is explained and characterized by a plasmon hybridization model and a universal scaling principle. A thinner intermediate silica layer, scaled by particle size, red shifts the plasmon resonance. This shift is relatively insensitive to the overall particle size and follows the universal scaling principle with respect to the resonant wavelength of a conventional silica-gold core-shell nanoshell. The extra tunability provided by the inner core further shifts the extinction peak to longer wavelengths, which is difficult to achieve on conventional sub-100 nm nanoshells due to limitations in synthesizing ultrathin gold coatings. We found multilayer nanoshells to be more absorbing with a larger gold core, a thinner silica layer, and a thinner outer gold shell. Both scattering intensity and angular radiation pattern were found to differ from conventional nanoshells due to spectral modulation from the inner core. Multilayer nanoshells may provide more backscattering at wavelengths where silica-gold core-shell nanoshells predominantly forward scatter.

© 2008 Optical Society of America

OCIS codes: (290.4020) Mie theory; (240.6680) Surface plasmon; (350.4238) Nanophotonics and photonic crystals.

References and links

1. A. Gulati, H. Liao, and J. H. Hafner, "Monitoring gold nanorod synthesis by localized surface plasmon resonance," J. Phys. Chem. B **110**, 323–22, 327 (2006).
2. C. Nehl, H. Liao, and J. Hafner, "Optical properties of star-shaped gold nanoparticles," Nano Lett. **6**, 683–688 (2006).
3. F. Hao, C. L. Nehl, J. H. Hafner, and P. Nordlander, "Plasmon resonances of a gold nanostar," Nano Lett. **7**, 729–732 (2007).
4. R. Averitt, D. Sarkar, and N. Halas, "Plasmon resonance shifts of Au-coated Au2S nanoshells: Insight into multicomponent nanoparticle growth," Phys. Rev. Lett. **78**, 4217–4220 (1997).
5. R. Averitt, S. Westcott, and N. Halas, "Linear optical properties of gold nanoshells," J. Opt. Soc. Am. B **16**, 1824–1832 (1999).
6. L. Hirsch, A. Gobin, A. Lowery, F. Tam, R. Drezek, N. Halas, and J. West, "Metal nanoshells," Ann. Biomed. Eng. **34**, 15–22 (2006).
7. H. Wang, D. Brandl, F. Le, P. Nordlander, and N. Halas, "Nanorice: A hybrid plasmonic nanostructure," Nano Lett. **6**, 827–832 (2006).
8. H. Cang, T. Sun, Z. Li, J. Chen, B. Wiley, Y. Xia, and X. Li, "Gold nanocages as contrast agents for spectroscopic optical coherence tomography," Opt. Lett. **30**, 3048–3050 (2005).
9. E. Prodan and P. Nordlander, "Structural tunability of the plasmon resonances in metallic nanoshells," Nano Lett. **3**, 543–547 (2003).

#102141 - $15.00 USD Received 29 Sep 2008; revised 7 Nov 2008; accepted 8 Nov 2008; published 12 Nov 2008

10. M. Landsman, G. Kwant, G. Mook, and W. Zijlstra, "Light-absorbing properties, stability, and spectral stabilization of indocyanine green," J. App. Physiol. **40**, 575–583 (1976).
11. C. Loo, L. Hirsch, M.-H. Lee, E. Chang, J. West, N. Halas, and R. Drezek, "Gold nanoshell bioconjugates for molecular imaging in living cells." Opt. Lett. **30**, 1012–1014 (2005).
12. A. Lin, N. Lewinski, J. West, N. Halas, and R. Drezek, "Optically tunable nanoparticle contrast agents for early cancer detection: model-based analysis of gold nanoshells," J. Biomed. Opt. **10**, 315102 (2005).
13. V. Nammalvar, A. Wang, and R. Drezek, "Enhanced gold nanoshell scattering contrast in cervical tissue using angled fiber probes," in *Nanoscale imaging, spectroscopy, sensing and actuation for biomedical applications IV, Proceedings of SPIE*, A. N. Cartwright and D. V. Nicolau, eds., vol. 6447 (2007).
14. J. Park, A. Estrada, K. Sharp, K. Sang, J. A. Schwatz, D. K. Smith, C. Coleman, J. D. Payne, B. A. Korgel, A. K. Dunn, J. W. Tunnell,"Two-photon-induced photoluminescence imaging of tumors using near-infrared excited gold nanoshells," Opt. Express **16**, 1590-1599 (2008).
15. L. Bickford, J. Sun, K. Fu, N. Lewinski, V. Nammalvar, J. Chang, and R. Drezek, "Enhanced multi-spectral imaging of live breast cancer cells using immunotargeted gold nanoshells and two-photon excitation microscopy," Nanotechnology **19**, 315102 (2008).
16. A. R. Lowery, A. M. Gobin, E. S. Day, N. J. Halas, and J. L. West, "Immunonanoshells for targeted photothermal ablation of tumor cells," Int. J. Nanomed. **1**, 149–154 (2006).
17. M. Bikram, A. M. Gobin, R. E. Whitmire, and J. L. West, "Temperature-sensitive hydrogels with SiO2-Au nanoshells for controlled drug delivery," J. Control. Release **123**, 219–227 (2007).
18. S. Oldenburg, J. Jackson, S. Westcott, and N. Halas, "Infrared extinction properties of gold nanoshells," Appl. Phys. Lett. **75**, 2897–2899 (1999).
19. R. Weissleder, "A clearer vision for in vivo imaging," Nature Biotechnol. **19**, 316-317 (2001).
20. P. K. Jain and M. A. El-Sayed, "Universal scaling of plasmon coupling in metal nanostructures: Extension from particle pairs to nanoshells," Nano Lett. **7**, 2854–2858 (2007).
21. X. Xia, Y. Liu, V. Backman, and G. A. Ameer, "Engineering sub-100 nm multi-layer nanoshells," Nanotechnology **17**, 5435–5440 (2006).
22. K. Chen, Y. Liu, G. Ameer, and V. Backman, "Optimal design of structures nanoshperes for ultrasharp light-scattering resonances as molecular imaging multilabels," J. Biomed. Opt. **10**, 024005 (2005).
23. B. Khlebtsov and N. Khlebtsov, "Ultrasharp light-scattering resonances of structured nanospheres: effects of size-dependent dielectric functions," J. Biomed. Opt. **11**, 044002 (2006).
24. L. LizMarzan, M. Giersig, and P. Mulvaney, "Synthesis of nanosized gold-silica core-shell particles," Langmuir **12**, 4329–4335 (1996).
25. Y. Hu, T. A. Nieminen, N. R. Heckenberg, and H. Rubinsztein-Dunlop, "Antireflection coating for improved optical trapping," J. Appl. Phys. **103**, 093,119 (2008).
26. C. F. Bohren and D. R. Huffman, *Absorption and Scattering of Light by Small Particles* (John Wiley and Sons, 1983).
27. H. C. van de Hulst, *Light Scattering by Small Particles* (Dover Publications, 1981).
28. H. Wang, K. Fu, R. A. Drezek, and N. J. Halas, "Light scattering from spherical plasmonic nanoantennas: effects of nanoscale roughness," Appl. Phys. B-Lasers O. **84**, 191–195 (2006).
29. H. Wang, Y. Wu, B. Lassiter, C. L. Nehl, J. H. Hafner, P. Nordlander, and N. J. Halas, "Symmetry breaking in individual plasmonic nanoparticles," P. Natl. Acad. Sci. USA **103**, 10,856–10,860 (2006).
30. J. B. Lassiter, J. Aizpurua, L. I. Hernandez, D. W. Brandl, I. Romero, S. Lal, J. H. Hafner, P. Nordlander, and N. J. Halas, "Close encounters between two nanoshells," Nano Lett. **8**, 1212–1218 (2008).
31. P. B. Johnson and R. W. Christy, "Optical constants of the noble metals," Phys. Rev. B **6**, 4370–4379 (1972).
32. U. Kreibig and M. Vollmer, *Optical Properties of Metal Clusters* (Springer, 1995).
33. S. Berciaud, L. Cognet, P. Tamarat, and B. Lounis, "Observation of intrinsic size effects in the optical response of individual gold nanoparticles," Nano Lett. **5**, 515–518 (2005).
34. B. N. Khlebtsov, V. A. Bogatyrev, L. A. Dykman, and N. G. Khlebtsov, "Spectra of resonance light scattering of gold nanoshells: Effects of polydispersity and limited electron free path," Opt. Spectrosc. **102**, 233–241 (2007).
35. C. L. Nehl, N. K. Grady, G. P. Goodrich, F. Tam, N. J. Halas, and J. H. Hafner, "Scattering spectra of single gold nanoshells," Nano Lett. **4**, 2355–2359 (2004).
36. P. Jain, K. Lee, I. El-Sayed, and M. El-Sayed, "Calculated absorption and scattering properties of gold nanoparticles of different size, shape, and composition: Applications in biological imaging and biomedicine," J. Phys. Chem. B **110**, 7238–7248 (2006).
37. E. Prodan, C. Radloff, N. J. Halas, and P. Nordlander, "A hybridization model for the plasmon response of complex nanostructures," Science **302**, 419–422 (2003).
38. K. Fu, J. Sun, A. W. H. Lin, H. Wang, N. J. Halas, and R. A. Drezek, "Polarized angular dependent light scattering properties of bare and PEGylated gold nanoshells," Curr. Nanosci. **3**, 167–170 (2007).
39. P. K. Jain, W. Huang, and M. A. El-Sayed, "On the universal scaling behavior of the distance decay of plasmon coupling in metal nanoparticle pairs: A plasmon ruler equation," Nano Lett. **7**, 2080–2088 (2007).
40. Y. Wang, W. Qian, Y. Tan, and S. Ding, "A label-free biosensor based on gold nanoshell monolayers for monitoring biomolecular interactions in diluted whole blood," Biosens. Bioelectron. **23**, 1166–1170 (2008).

#102141 - $15.00 USD Received 29 Sep 2008; revised 7 Nov 2008; accepted 8 Nov 2008; published 12 Nov 2008

41. E. M. Larsson, J. Alegret, M. Käll, D. S. Sutherland, "Sensing characteristics of NIR localized surface plasmon resonances in gold nanorings for application as ultrasensitive biosensors," Nano Lett. **7**, 1256-1263 (2007).
42. M. A. van Dijk, A. L. Tchebotareva, M. Orrit, M. Lippitz, S. Berciaud, D. Lasne, L. Cognet, and B. Lounis, "Absorption and scattering microscopy of single metal nanoparticles," Phys. Chem. Chem. Phys. **8**, 3486–3495 (2006).
43. A. Agrawal, S. Huang, A. W. H. Lin, M.-H. Lee, J. K. Barton, R. A. Drezek, and T. J. Pfefer, "Quantitative evaluation of optical coherence tomography signal enhancement with gold nanoshells," J. Biomed. Opt. **11**, (2006).
44. Y. Han, J. Jiang, S. S. Lee, and J. Y. Ying, "Reverse microemulsion-mediated synthesis of silica-coated gold and silver nanoparticles," Langmuir **24**, 5842–5848 (2008).

1. Introduction

The human use of gold has been well documented throughout history. Observations have been long made on the unique optical properties of nano-sized particles composed of gold. The rapid development in controlled chemical synthesis and computational modeling has generated an extensive exploration on various gold-related nanostructures, ranging from nanorods [1] and nanostars [2, 3], to core-shell nanoshells [4–6], nanorice [7], and nanocages [8]. Silica-gold core-shell nanoshells have attracted particularly significant research attention due to agile optical tunabilities [4, 9] and absorption and scattering cross sections which can greatly exceed those of organic dyes [10, 11]. Superior photochemical stability in combination with excellent biocompatibility renders gold nanoshells highly attractive for biomedical imaging and spectroscopy applications, such as optical coherence tomography [12], reflectance spectroscopy [13], dark-field and two photon microscopy [11, 14, 15]. Gold nanoshells have also been investigated for photothermal therapy and controlled drug release [16, 17].

Extinction spectra of the core-shell nanoshell can be tuned by varying the gold-shell thickness scaled by particle size. The plasmon resonance of gold nanoshells is related to the interaction between plasmons supported on the inner and outer surface of the gold shell. The strength of their interaction is determined by the shell thickness scaled by particle size. As the gold shell decreases in thickness, a stronger plasmon interaction red shifts the resonance peak compared to that of a solid gold particle. This allows the tuning of nanoshell plasmon resonances into the near-infrared (NIR) region [18] where main biological absorption is minimal [19]. The universal dependence of red shifts upon shell thicknesses scaled by particle size was reported by Jain *et al* [20].

Here we examine the optical properties of gold-silica-gold multilayer nanoshells. Fig. 1. illustrates the structure of multilayer nanoshells and silica-gold core-shell nanoshells. Xia *et al*. were the first to report the synthesis of $\sim$50 nm multilayer nanoshells that may exhibit NIR absorption peaks [21]. Coating gold colloid with a thin layer of silica was achieved by a modified Stöber method in which silica growth was preceded by a sodium silicate (active silica) treatment in an aqueous solution with a controlled pH. The outer gold coating was produced similarly to the way conventional nanoshells are made. Due to the use of small gold colloids ($\sim$20 nm) and the relative ease of silica coating with various thicknesses, sub-100 nm multilayer nanoshells can be synthesized. While comparable in size with some solid gold spheres, a greater spectral tunability is expected for multilayer nanoshells due to the interaction of plasmons on interfaces between gold and dielectrics. Such nanoshells could also offer a smaller profile than their conventional counterparts, thus provide better vascular permeability and more efficient antibody conjugation owing to the larger surface-to-volume ratio [21].

Thus far, the optical properties of the multilayer nanoshell, composed of a metallic core and two alternating dielectric and metallic layers, have been investigated by Chen *et al*. to achieve ultrasharp resonant peaks across the spectrum for multiplexing applications [22]. In the study, the overall diameter of the nanoshell was kept at 10 nm and the layers were tailored with

#102141 - $15.00 USD Received 29 Sep 2008; revised 7 Nov 2008; accepted 8 Nov 2008; published 12 Nov 2008

subnanometer precision. The thin layers sparked some controversy over spectral broadening due to the intrinsic size effect on metal properties for nano-sized particle simulations [23].

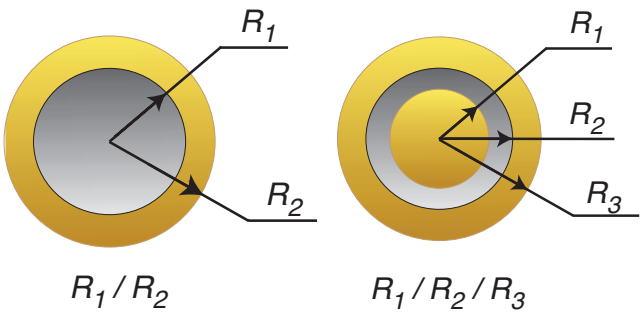

(a) Conventional nanoshell (CNS) (b) Multilayer nanoshell (MNS)

Fig. 1. Geometries of (a) silica-gold core-shell conventional nanoshells, and (b) gold-silica-gold multilayer nanoshells.

The goal of this paper is to examine the spectral and angular scattering properties of gold-silica-gold multilayer nanoshells in the size region where successful particle syntheses have been reported and can be achieved based on currently available protocols [21, 24]. The study is based on what has been done on conventional nanoshells, with the objectives of unveiling and understanding the similar and distinct optical properties of multilayer nanoshells, as well as investigating their potential for bioimaging applications.

2. Methodology

A Mie-based computation code has been developed to calculate light scattering from concentric spheres [25–27]. Boundary conditions at each inter-layer interface are expressed in term of vector spherical wave functions and unknown field coefficients. The tangential electric and magnetic fields are stored as alternating rows for each interface in a square matrix and the vector of unknown coefficients is resolved by a matrix division. This approach has a substantial computational advantage as it can handle subjects from spheres with stratification to spheres with gradient index profiles. Extinction, scattering and absorption coefficients were calculated based on Mie scattering coefficients obtained from the Mie code. Angular radiation was calculated for unpolarized light using the approach outlined by van de Hulst [27]. Details of the code can be found in [25].

In this study, plane-wave expansion coefficients are used for illumination. This assumes that particles are located far enough from the light source or that the particles are significantly smaller than the incident beam profile. Other assumptions include that the particles are rigidly spherical and the layers are concentric. It is to be noted that various factors, such as surface topology [28], core eccentricity [29] and interparticle distance [30] have been reported to affect the nanoshell spectra to various degrees.

For gold properties, data from Cristy and Johnson [31] are adapted for the simulation. While the spectral broadening effect from surface scattering in nano-sized particles has been proposed and observed on gold colloids [32,33], the current literature on intrinsic effects of the core-shell nanoshells has not been able to reach a consensus. Common practice at times adds an additional term to the bulk material dielectric constant to acount for the limited free electron path imposed by the thin gold shell [4]. Others propose that this modification is determined by the core radius to shell thickness ratio [34]. However, it was reported that intrinsic effects were not observed

#102141 - $15.00 USD Received 29 Sep 2008; revised 7 Nov 2008; accepted 8 Nov 2008; published 12 Nov 2008

on spectral measurement of single silica-gold nanoshells [35]. In light of controversies over this issue, intrinsic size corrections were not considered in this study. In addition, we attempt to construct gold layer geometries outside the region where intrinsic effects prevail.

In simulations presented, water is the surrounding medium unless otherwise noted. The dielectric constant for silica was set to 2.04 and that for water was 1.77. The Mie code was validated against published spectral results for gold particles [36], silica-gold nanoshells [36], and gold-silica-gold-silica nanoshells [37], as well as angular radiation patterns of silica-gold nanoshells [38].

3. Spectral properties

3.1. Tunability from the inner gold core

In this section, effects from the inner gold core are qualitatively explained by a plasmon hybridization model and quantitatively examined using Mie theory. The goal is to explore the possibilities of synthesizing multilayer nanoshells with enhanced optical properties in the NIR region.

Similar to conventional nanoshells (CNS), multilayer nanoshells (MNS) have tunable optical properties, as explained by plasmon hybridization theory [37]. Briefly stated, the tunability of a CNS is attributed to the interaction between plasmons that reside on the outer and inner surface of the gold shell, also known as the sphere and cavity plasmon. The interaction causes the plasmon to split into a low-energy bonding mode and a high-energy anti-bonding mode. The bonding mode is often visualized by the surface plasmon resonance peak of the nanoshell in the vis-NIR region. The peak can be tuned by varying the ratio of shell thickness to core radius, which essentially tunes the coupling strength between the two plasmons.

In contrast to CNS, MNS have an extra degree of tunability from the inner gold core. This optical tunability can be understood as an interaction between the CNS bonding mode $|BN\rangle$ and the gold core sphere mode $|rC\rangle$. The thickness of the intermediate silica layer determines the degree of interplay between the two modes. An increase in the inner gold core radius on an otherwise fixed geometry will decrease the intermediate silica layer thickness and increase the plasmon interaction. This is accompanied by a red shift of the spectrum that is in agreement with Mie calculation results, shown in Fig. 2 (Media 1).

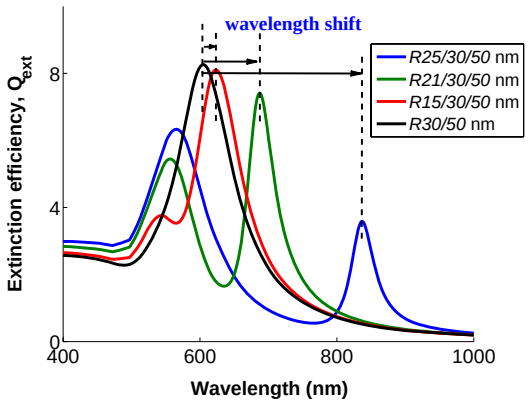

Fig. 2. Calculated spectra of CNS and MNS with various inner core radii while the silica and outer radius remain the same (Media 1). The red shift of MNS from CNS is indicated by lambda shift.

The extra tunability introduced by the inner gold core facilitates the synthesis of small MNS

#102141 - $15.00 USD Received 29 Sep 2008; revised 7 Nov 2008; accepted 8 Nov 2008; published 12 Nov 2008

with NIR extinction peaks. This is not an option for CNS. Near-infrared extinction is difficult to achieve on small CNS because extremely thin outer gold layers are required. The current coating process involves functionalizing the silica core surface with amine groups, then attaching small gold colloids (1–2 nm in size) to form nucleation sites for further reduction of gold to form a continuous layer [6]. However, for sub-10 nm coats, it is often difficult to achieve even layers and smooth surfaces, both of which are needed to avoid drastic deterioration in the overall integrity of the nanoshell spectrum [28, 29]. For MNS, these requirements are alleviated because extinction peaks can be further red shifted by having a larger inner gold core with a thin surrounding silica layer. The compromise is a damped peak owing to the increasing plasmon strength associated with the gold core mode $|rC\rangle$.

3.2. Universal scaling principle

Given that the plasmon coupling strength is qualitatively determined by the intermediate silica layer thickness, a quantitative analysis is desired to characterize the spectrum signature of MNS with various dimensions. Among recently reported observations is the universal scaling principle, which was first reported for metal particle pairs in which plasmon resonance is red shifted from that of an isolated metal sphere by moving the two particles closer together [39]. The shift exhibits a near-exponential decay with increasing interparticle distance. Jain et al. extended this theory to CNS where the gold shell thickness, scaled by particle size, is analogous to the interparticle gap and the two interacting plasmon modes act as a particle pair [20]. A similar exponential decay is observed independent of the overall nanoshell dimension. While MNS support more than two plasmons, their plasmon resonance is mainly determined by the interaction between the bonding mode of CNS and the sphere mode of the gold core. The CNS anti-bonding mode, however, has a very small dipole moment because the cavity plasmon is oppositely aligned with the sphere mode. For this reason, the CNS anti-bonding mode interaction with the core mode is small and becomes too damped to be visible in the spectra. The coupling strength between the two major-playing modes is determined by the intermediate silica layer thickness, scaled by the overall particle size. With R_2/R_3 ratio kept constant, a universal decaying curve is observed for MNS of different dimensions.

Figure 3 illustrates an exponential decay insensitive to the overall particle size at a constant ratio of $R_2/R_3 = 0.6$. Results (data not shown) indicate that both the R_2/R_3 ratio and the surrounding medium affect the rate of decay. In addition, larger MNS were found to retain the same exponential decay but at slightly different rates. This can be partially attributed to the fact that multiple resonant peaks start to emerge with broad widths and less well-defined shapes. Nevertheless, the universal scaling principle demonstrates that CNS plasmon resonant peaks can be further red shifted on MNS by reducing the silica layer thickness. For particles retaining their overall dimension and outer shell thickness, this translates to the use of large gold cores with thin silica coatings.

It is worth noting that when t is pushed to the zero limit where $R_1 = R_2$, thus the silica layer thickness approaches zero, the plasmon mode red shifts to zero energy. However, the spectral weight becomes negligible due to the cancellation of the dipole moments of the core and of the shell.

3.3. Sensitivity to the surrounding medium

The plasmon hybridization model can be used to explain the spectral sensitivity of MNS to the surrounding medium. MNS plasmons are resulted from the hybridization between CNS bonding modes $|BN\rangle$ and gold core sphere modes $|rC\rangle$, and since $|rC\rangle$ is not in direct contact with the outside, $|BN\rangle$ is the mode mainly affected by the surrounding medium. For instance, an increase in the refrative index of the medium does not directly affect $|rC\rangle$ but red shift $|BN\rangle$,

#102141 - $15.00 USD Received 29 Sep 2008; revised 7 Nov 2008; accepted 8 Nov 2008; published 12 Nov 2008

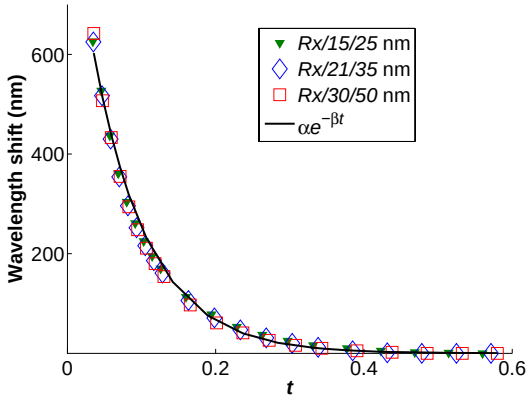

Fig. 3. Mie calculation results for wavelength shifts from the MNS ($R_1/R_2/R_3$) vis-NIR plasmon resonance peak relative to that of CNS (R_2/R_3) with the same silica and outer gold radius versus intermediate silica thickness scaled by particle size of MNS. $t = (R_2 - R_1)/R_3$, α = 972.43, β = 13.48.

contributing to an overall red shift as demonstrated in Fig. 4. This suggests that MNS may be used as sensors in various sensing applications based on detecting localized surface plasmon resonances (LSPRs).

While CNS and other nanostructure have been studied for sensing applications [40,41], MNS may offer some unique opportunities given multiple extinction peaks shifted in a synchronous fashion when the surrounding medium is perturbed. Moreover, the degree of shift of each peak was found to be particle-dependent. Table 1 tabulates the wavelength shift for two MNS with an identical size and gold shell thickness. Between the two, MNS2 bears a stronger plasmonic coupling between $|BN\rangle$ and $|rC\rangle$ than MNS1. It can be seen that MNS2 has a larger peak shift at the shorter wavelength and its inter-peak distance decreases with increasing medium indices. The opposite was found for MNS1. Also observed is that the shift of each peak of the MNS approximately adds up to that of the single SPR on an equivalent CNS.

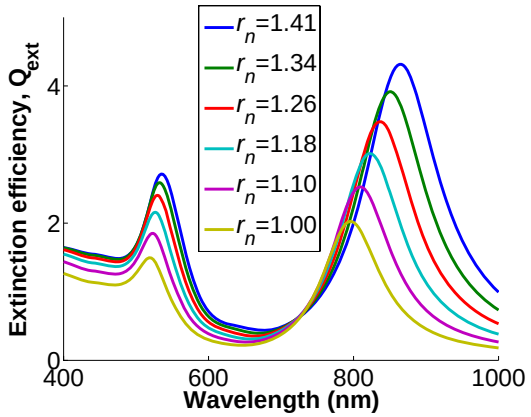

Fig. 4. Calculated extinction spectra of $R20/30/35$ nm MNS immersed in various media with distinct refractive indices.

#102141 - $15.00 USD Received 29 Sep 2008; revised 7 Nov 2008; accepted 8 Nov 2008; published 12 Nov 2008

Table 1. Surface plasmon resonance peak shift of $R20/35/50$ nm (MNS1), $R30/35/50$ nm (MNS2), and $R35/50$ nm (CNS) in different dielectric media ($\lambda_{p2} > \lambda_{p1}$).

	p1 shift (nm)		p2 shift (nm)		p2-p1 (nm)		p shift (nm)
refractive index	MNS1	MNS2	MNS1	MNS2	MNS1	MNS2	CNS
1.0	0	0	0	0	110	424	0
1.1	5	8	10	4	115	420	15
1.2	11	20	22	9	121	413	33
1.3	16	37	38	15	132	402	56
1.4	21	53	56	22	145	393	80
1.5	27	68	77	29	160	385	105

3.4. Tunability on scattering and absorption

Rayleigh criteria state that, for particles much smaller than the wavelength, the scattering intensity is proportional to R^6, where R is the particle radius [42]. However, absorption depends on particle volume, which is proportional to R^3 for a sphere. The higher order dependence on particle size makes scattering more sensitive to size variations than absorption. For instance, at 532 nm, 100 nm solid gold spheres have approximately the same absorption and scattering cross sections in water [42]. Scattering attenuates more drastically than absorption when particle size decreases, rendering gold colloids absorption-dominant. In contrast, increasing particle size enhances scattering much faster than absorption; thus, large particles are mainly scattering-based. For inhomogeneous spheres, such as silica-gold core-shell CNS, it has been demonstrated that the scattering-to-absorption ratio rises with increasing core size or outer shell thickness or both [12]. These observations provide very useful guidelines for synthesizing particles to match either scattering- or absorption-based applications at desired wavelengths [16,43].

The scattering and absorption behavior of concentric multilayer spheres can be studied similarly as functions of layer thickness to obtain insight into how changes in each layer affect the overall scattering and absorption. Due to the complexity in displaying results with concurrent variation in each of the three layers, simulations were adapted to geometries in which two layer thicknesses were changed while the third layer remained fixed. Three sets of runs were performed with three combinations of the two variable-layer thicknesses. At each dimension, the extinction, scattering, and absorption spectra were calculated from 400 to 1941 nm. Two plasmon resonance wavelengths λ_{max} were chosen at the extinction maxima. The scattering to extinction ratio was calculated at the longer of the two; the one associated with the MNS mode rather than the gold sphere mode. If only one maximum occurred in the wavelength range, then the calculation was performed at that wavelength. Since the resulting plots illustrate the scattering ratio at the longer plasmon resonant wavelengths, we expect the magnitude of the extinction peak to attenuate as it red shifts and it may become weaker than the resonance at shorter wavelengths.

3.4.1. Inner gold core radius fixed at 10 nm

This inner core radius was chosen based on the first experimental synthesis of MNS [21]. Figure 5(a) indicates that scattering increases with thicker silica layers or thicker outer gold shells or both. This behavior resembles that reported for CNS [12]. With a thin silica layer coating ($<$10 nm) [21, 24, 44], MNS exhibit more absorption than scattering. However, when the silica layer thickness is increased beyond 20 nm, MNS become mainly scattering at practical outer shell

#102141 - $15.00 USD Received 29 Sep 2008; revised 7 Nov 2008; accepted 8 Nov 2008; published 12 Nov 2008

thicknesses.

3.4.2. Intermediate silica layer fixed at 10 nm

For these calculations, Fig. 5(b) shows that the general trend still holds that thicker outer shells produce more scattering; however, the role of the inner gold core is less clear. Below 20 nm, an increase in the core radius slowly increases the scattering-to-extinction ratio, but this trend seems to reverse when the core radius goes above 20 nm. Another set of simulations on 20 nm silica layers (not shown here) indicate minimal effects from the gold core below 10 nm in radius and the scattering-to-extinction ratio became relatively insensitive to further increases in core radius. At thin silica layer thicknesses ($<$5 nm), MNS behavior is similar to solid gold colloids in that increasing the inner core radius gradually enhances scattering.

3.4.3. Outer shell fixed at 20 nm

Similar to the results in Fig. 5(a) and 5(b), Fig. 5(c) displays a profile in which absorption is dominant or equivalent to scattering for thin silica layers ($<$10 nm). Thicker silica layers ($>$10 nm) quickly turn MNS into scattering particles, with minimal impact from the inner gold core.

3.4.4. Outer shell and overall size fixed

To elucidate the core effect, the overall diameter and the outer shell thickness were kept fixed. The inner core radius was gradually increased to the point at which the core made contact with the outer shell. The absorption-to-extinction ratio was obtained at the plasmon resonance, as described above, and results are shown in Fig. 5(d).

Four different geometries with the same R_1/R_2 ratio are plotted in Fig. 5(d). As the core radius increases, the absorption component at the plasmon resonance also increases. This is counterintuitive since we expect large gold colloids to exhibit more scattering than absorption. The explanation lies in the interplay between the gold core and other layers of the MNS. For instance, an increasing core size results in a thinner silica coating in this otherwise fixed geometry, and according to Fig. 5(a)–5(c), thinner silica layers produce less scattering; this is consistent with the behavoir in Fig. 5(d). Furthermore, the discontinuities at large R_1/R_2 ratios reflect the region where the silica layer becomes so thin that the MNS resonant wavelengths lie outside the region of interest and the gold colloid resonance dominates. MNS demonstrate strong scattering characteristics associated with solid gold spheres. It can be seen that large particles (i.e. $Rx/80/100$ nm) produce more scattering than small particles (i.e. $Rx/24/30$ nm). Because one of the main advantages of MNS over CNS is their relatively small size owing to the use of small gold cores and the possibility of coating them with thin silica layers, sub-100 nm MNS are perceived as advantageous in absorption applications where NIR extinction is desired.

4. Angular radiation properties

To understand scattering enhancement by nanoshells in applications where detection angle and angular acceptance range may differ, angular properties need to be considered. Angular properties are commonly characterized by the overall radiation power and its directivity within certain angular ranges. The former is defined by the scattering cross section, C_{sca}, and the latter is often described by a single-value parameter: the anisotropy factor g, which is a cosine-weighted average over all values of the scattering angle. The scattering cross section is calculated from the Mie coefficients [27]. The anisotropy factor g is calculated as

$$g = \frac{\int_0^\pi S_{11}(\theta) cos\theta 2\pi sin\theta d\theta}{\int_0^\pi S_{11}(\theta) 2\pi sin\theta d\theta} \quad (1)$$

#102141 - $15.00 USD Received 29 Sep 2008; revised 7 Nov 2008; accepted 8 Nov 2008; published 12 Nov 2008

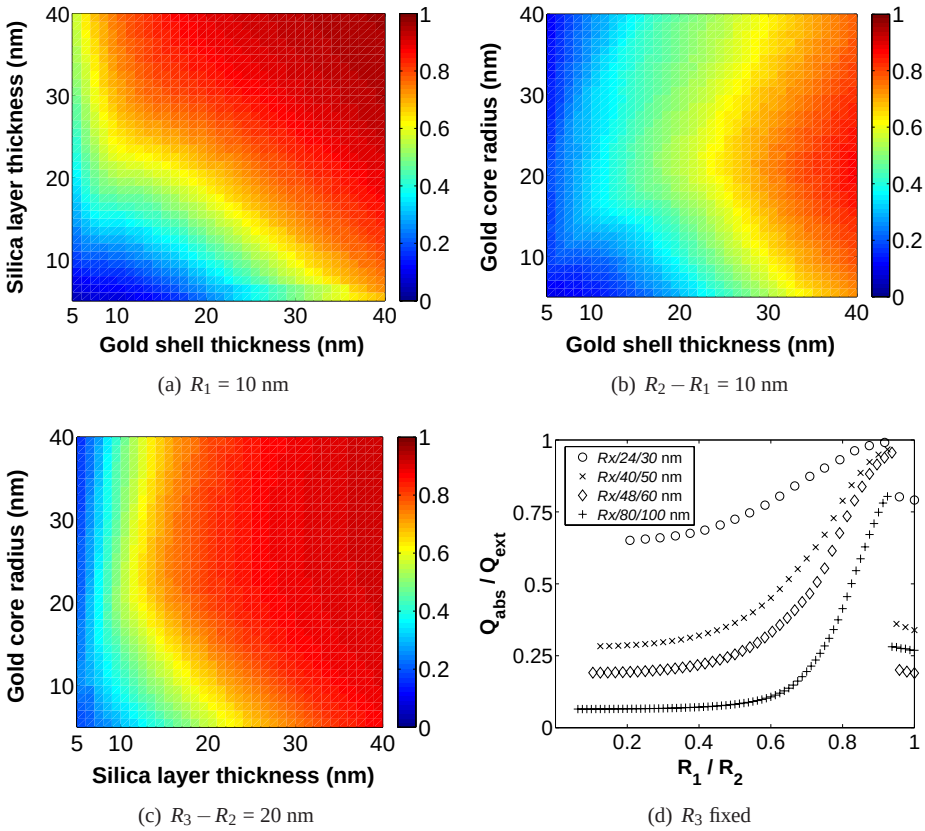

(a) R_1 = 10 nm (b) $R_2 - R_1$ = 10 nm

(c) $R_3 - R_2$ = 20 nm (d) R_3 fixed

Fig. 5. Scattering-to-extinction ratio at plasmonic resonant wavelengths of MNS with (a) inner gold core radius kept at 10 nm and varying the silica and outer gold layer thickness, (b) silica layer thickness kept at 10 nm and varying the inner gold core radius and outer gold layer thickness, (c) outer gold shell kept at 20 nm and varying the inner gold core radius and silica layer thickness. Absorption-to-extinction ratio (d) at plasmonic resonant wavelengths of MNS with the overall diameter and outer gold shell thickness fixed and varying the inner gold core radius and silica layer thickness.

where S_{11} is the angular radiation power of unpolarized light.

For strongly scattering nanoshells ($>$ 200 nm in size), the main extinction peak coincides with the scattering peak where the radiation pattern grows to an overall maximal level. Because MNS and CNS exhibit distinct spectra, as shown in Fig. 2, drastically different radiation patterns are expected at some wavelengths. Figure 6 (Media 2) compares the radiation patterns from MNS and CNS computed as the radiation power normalized to the incident power at one meter from the center of the particle. The radiation power was integrated over all azimuthal angles and plotted in logarithmic form: $\log_{10}(P_{rad}/P_{inc})$. Scattering cross sections are highlighted at selected wavelengths corresponding to the radiation pattern. The overall size and outer shell thickness were chosen so that the corresponding CNS are scattering-dominant.

It can be seen that $R90/125/140$ nm MNS scatters more at 550 nm [Fig. 6(a)], whereas $R125/140$ nm CNS radiates more at 755 nm [Fig. 6(b)] and 1145 nm [Fig. 6(c)]. At 1270 nm the two nanoshells scatter approximately the same [Fig. 6(d)]; this is also indicated by the nearly equivalent scattering cross sections [Fig. 6(e)]. Although optical cross sections give an

#102141 - $15.00 USD Received 29 Sep 2008; revised 7 Nov 2008; accepted 8 Nov 2008; published 12 Nov 2008

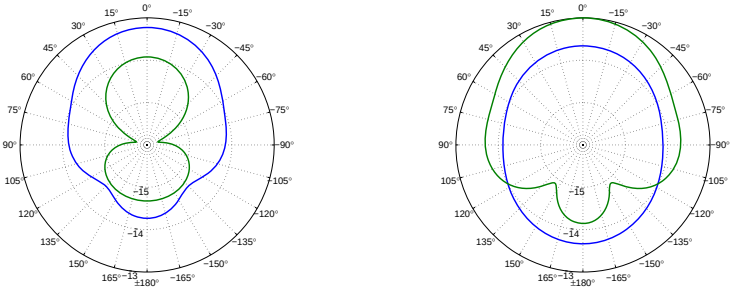

(a) λ =550 nm (b) λ =755 nm

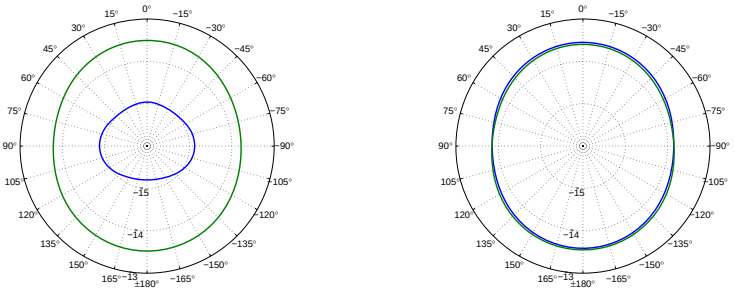

(c) λ =1145 nm (d) λ =1270 nm

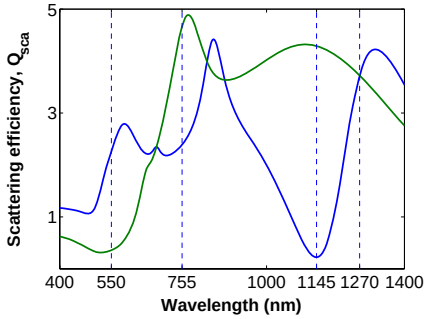

(e) Q_{sca}

Fig. 6. Angular radiation pattern of R90/125/140 nm MNS (blue) and R125/140 nm CNS (green) at (a) 550 nm, (b) 755 nm, (c) 1145 nm, (d) 1270 nm and (e) scattering spectra of MNS (blue) and CNS (green) (urlMedia 2). Nanoshells are located in the center of the plot, and the incident wave enters from the bottom (180°).

overall indication of the radiating power, they do not provide angular properties. For instance, despite an overall stronger radiation at 755 nm, $R125/140$ nm CNS does not project as much power in the back direction as $R90/125/140$ nm MNS. From the radiation patterns above, it can also be observed that $R125/140$ nm CNS is more forward-scattering (positive g) at shorter wavelengths and becomes isotropic ($g \sim 0$) and slightly back-scattering (negative g) at wavelengths longer than the resonance wavelengths. The $R90/125/140$ nm MNS, however, does not exhibit regularities that can be associated with spectral signatures.

To further consolidate this observation, spectral properties are plotted side by side with the anisotropy factor at different wavelengths for 200 nm CNS and MNS with various layer geome-

#102141 - $15.00 USD Received 29 Sep 2008; revised 7 Nov 2008; accepted 8 Nov 2008; published 12 Nov 2008

tries in Fig. 7. A well-defined border between large and near-zero g values is found to follow the general trend of CNS spectra. This suggests the plasmon resonant wavelength is a boundary beyond which CNS primarily scatter isotropically. Nevertheless, MNS seem to reach low g values at shorter wavelengths prior to the plasmon resonance. This may indicate a stronger back scattering profile compared to CNS, as already seen in Fig. 6(b).

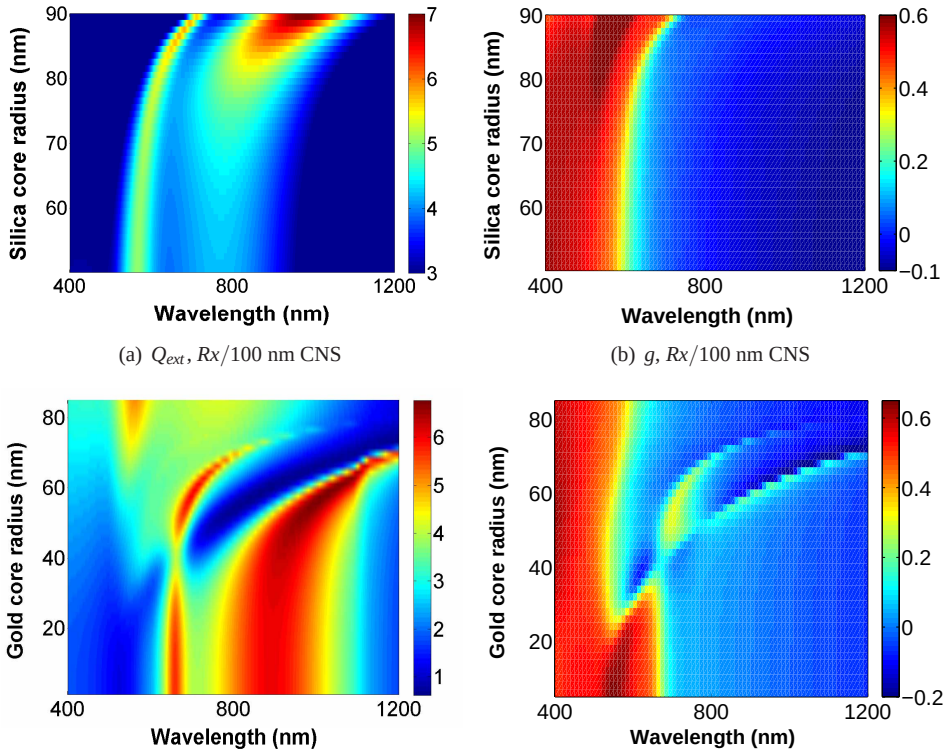

(a) Q_{ext}, $Rx/100$ nm CNS

(b) g, $Rx/100$ nm CNS

(c) Q_{ext}, $Rx/85/100$ nm MNS

(d) g, $Rx/85/100$ nm MNS

Fig. 7. (a) Extinction efficiency spectra for $Rx/100$ nm CNS with varying silica core radius x. (b) Anisotropy factor plot for corresponding CNS at different wavelengths. (c) Extinction efficiency spectra for $Rx/85/100$ nm MNS with varying gold core radius x. (d) Anisotropy factor plot for corresponding MNS at different wavelengths.

5. Summary

Both spectral and angular radiation properties of gold-silica-gold multilayer nanoshells have been studied using Mie theory. The plasmon hybridization model was employed to explain the spectral tunability due to inner gold core. While the plasmon coupling strength of CNS is known to be determined by a normalized gold shell thickness, that of the MNS was found to be determined by the normalized intermediate silica layer thickness. A thinner silica layer results in a red shift of the plasmon resonance. Furthermore, the MNS spectral shift from CNS without the gold core is characterized by an exponential curve that was found to be insensitive to the particle size, when the outer shell thickness-to-particle size is fixed. This confirms the universal scaling principle reported on particle pair systems and silica-gold core-shell CNS. MNS also demonstrate many characteristics that are similar to CNS. For instance, a thicker

#102141 - $15.00 USD Received 29 Sep 2008; revised 7 Nov 2008; accepted 8 Nov 2008; published 12 Nov 2008

silica layer and a thinner gold shell both red shift the MNS spectrum (results not shown) and produce more scattering at the plasmon resonance. MNS are sensitive to the external medium and their multiple extinction peaks with deep spectral valleys may prove valuable for improving the sensitivity and specificity of various biosensing and bioimaging modalities.

Scattering patterns from MNS differ from those of CNS due to the spectral modulation induced by the core. Trends in MNS angular radiation patterns are more intricate than those of CNS. While CNS predominantly forward-scatter at wavelengths shorter than the plasmon resonant wavelength, MNS may radiate more in the back and side directions at these wavelengths.

In summary, this study compares the optical properties of composite multilayer structures with those of CNS, whose properties are well understood. Fully exploiting the potential of MNS requires synthetic studies assessing independent control of each layer, morphological and topological features, size dispersity, and protocol repeatability. It is anticipated that such studies will lead to development of multilayer nanoshells, which, in turn, will accelerate the development of new applications.

Acknowledgment

This work is supported by the Welch Foundation grant (C-1598), DoD CDMRP (W81XWH-07-1-0428), the Gulf Coast Center for Computational Cancer Research, and the Center for Biological and Environmental Nanotechnology (NSF EEC-0118007 and EEC-0647452). The authors would like to thank Professor Peter Nordlander for his discussion on the plasmon hybridization model and the universal scaling principle, as well as Jim Haile for preparing the manuscript. The polar plots were made based on a modified program initially developed by D. D. Hanselman. Ying Hu is supported by DoE Computational Science Graduate Fellowship program.

#102141 - $15.00 USD Received 29 Sep 2008; revised 7 Nov 2008; accepted 8 Nov 2008; published 12 Nov 2008

Stabilization and Targeting of Surfactant-Synthesized Gold Nanorods

Betty C. Rostro-Kohanloo,[1] Lissett R. Bickford,[3] Courtney M. Payne,[1] Emily S. Day,[3] Lindsey J. E. Anderson,[1] Meng Zhong,[4] Seunghyun Lee,[2] Kathryn M. Mayer,[1] Tomasz Zal,[5] Liana Adam,[4] Colin P. N. Dinney,[4] Rebekah A. Drezek,[3] Jennifer L. West,[3] Jason H. Hafner[1,2]

[1]Dept. of Physics & Astronomy, 6100 Main St, Rice University, Houston, TX 77005

[2]Dept. of Chemistry, Rice University, 6100 Main St, Rice University, Houston, TX 77005

[3]Dept. of Bioengineering, Rice University, 6100 Main St, Rice University, Houston, TX 77005

[4]Dept. of Urology, MD Anderson Cancer Center, 1515 Holcombe Blvd, Houston, TX 77030

[5]Dept. of Immunology, MD Anderson Cancer Center, 1515 Holcombe Blvd, Houston, TX 77030

Short Title: Gold Nanorod Targeting

PACS: 87.85.Rs

ABSTRACT

The strong cetyltrimethylammonium bromide (CTAB) surfactant responsible for the synthesis and stability of gold nanorod solutions complicates their biomedical applications. The critical parameter to maintain nanorod stability is the ratio of CTAB to nanorod concentration. The ratio is approximately 740,000 as determined by chloroform extraction of the CTAB from a nanorod solution. A comparison of nanorod stabilization by thiol-terminal poly(ethylene glycol) (PEG) and by anionic polymers reveals that PEGylation results in higher yields and less aggregation upon removal of CTAB. A heterobifunctional PEG yields nanorods with exposed carboxyl groups for covalent conjugation to antibodies with the zero length carbodiimide linker EDC. This conjugation strategy leads to approximately 2 functional antibodies per nanorod according to fluorimetry and ELISA assays. The nanorods specifically targeted cells in vitro, and were visible with both two photon and confocal reflectance microscopies. This covalent strategy should be generally applicable to other biomedical applications of gold nanorods as well as other gold nanoparticles synthesized with CTAB.

*MANUSCRIPT TEXT

1. Introduction

Localized surface plasmon resonances (LSPR) of gold nanoparticles result in strong optical absorption and scattering at visible and near-infrared wavelengths.[1] These optical properties are of considerable interest for biomedical applications, since the plasmon resonance can affect localized heating and light scattering, and since gold nanoparticles are relatively inert in biological systems. Tunable gold nanoparticles have been recently investigated for applications in photothermal therapy, drug delivery, and diagnostic imaging.[2-8] Biomedical applications will ultimately rely on the ability to target the gold nanoparticles specifically to certain tissues or cell types with antibodies, aptamers, and peptides.[9] A variety of gold nanoparticle shapes have been fabricated and investigated, including spheres,[10] shells,[11] rods,[12-18] cages,[19, 20] and stars.[21] One nanoparticle synthesis that is particularly powerful and versatile is the growth of colloidal gold seeds in the presence of the surfactant cetyltrimethylammonium bromide (CTAB). This method produced gold nanorods at first in low yield,[22] and then later in high yield[23, 24] with resonances in the near-infrared. Gold nanorods are of particular interest for biomedical applications due to their small size and potentially improved permeation into tissue, relative to larger tunable gold nanoparticles. However, gold nanorods and other shapes synthesized with CTAB are also stabilized by this strong surfactant, which is thought to form a bilayer on the nanoparticle surface.[25] If the CTAB is removed from solution, the nanorods immediately aggregate.[17] Several strategies have been developed to modify the surface chemistry of nanorods, including polyelectrolyte wrapping to bind the CTAB layer,[26] displacement of the CTAB layer by a thiol terminal polyethylene glycol (PEG),[17] and displacement by alkanethiols[27] and

---

* Abbreviations: Ab = antibody; AF-Ab = Alexa Fluor labeled antibody; CCD = charge coupled device; CTAB = cetyltrimethylammonium bromide; EDC = 1-ethyl-[3-dimethylaminopropyl]carbodiimide; ELISA = enzyme linked immunosorbent assay; LSPR = localized surface plasmon resonance; MES = 2-(N-morpholino)ethanesuflonic acid (MES); NHS = N-hydroxysuccinimide; PBS = phosphate buffered saline; PEG = poly(ethylene glycol); PSS = poly(sodium 4-stryene-sulfonate); WGA = wheat germ agglutinin

lipids.[28] Even with these options, manipulation and targeting of nanorods has proven difficult, although there has been some recent success with polyelectrolyte wrapping.[9, 12, 29-37] This report describes progress on three aspects of biological targeting of CTAB-synthesized gold nanorods. First, the sensitivity of nanorod stability to CTAB concentration has been carefully characterized. Second, a simple chemical strategy has been developed to create nanorod-antibody conjugates based on strong gold-thiol and amide bonds that specifically target cells. Third, optical imaging modalities to detect nanorods in cells have been studied.

2. Materials and Methods

Nanorod Synthesis

Gold nanorods were prepared as described previously,[23, 24] but the procedure was scaled up to increase the quantity. All solutions were prepared fresh for each synthesis, except for the hydrogen tetrachloroaurate(III) (Sigma, #520918), which was prepared as a 28 mM stock solution from a dry ampule and stored in the dark. An aliquot of the stock solution was diluted to 10 mM immediately before use. Gold seed particles were prepared by adding 250 μL of 10 mM hydrogen tetrachloroaurate(III) to 7.5 mL of 100 mM cetyltrimethylammonium bromide (CTAB) (Sigma, #H9151) in a plastic tube with brief, gentle mixing by inversion. Next, 600 μL of 10 mM sodium borohydride (Acros, #18930) was prepared from DI water chilled to 2-8° C in a refrigerator and added to the seed solution *immediately* after preparation, followed by mixing by inversion for 1-2 min. The pale brown seed solution was stable and usable for several hours.

The nanorod growth solution was prepared by adding the following reagents to a plastic tube in the following order and then gently mixing each by inversion: 425 mL of 100 mM CTAB, 18 mL of 10 mM hydrogen tetrachloroaurate(III), and 2.7 mL of 10 mM silver nitrate (Acros, #19768). Next, 2.9 mL of 100 mM ascorbic acid (Fisher, #A61) was added and mixed by inversion, which changed the solution from brownish-yellow to colorless. To initiate nanorod growth, 1.8 mL of seed solution was added to

the growth solution, mixed gently by inversion, and left still for three hours. During this time, the color changed gradually to dark purple, with most of the color change occurring in the first hour.

Nanorod Stabilization

Nanorod solutions were heated to 30 C to melt CTAB crystals which form at room temperature, and therefore provide a known initial CTAB concentration of 100 mM. 5 mL aliquots were pelleted by centrifugation at 6000 rpm for 60 minutes. 4.5 mL of the clear supernatants were decanted, and the pellets were resuspended with water. The nanorod solutions were pelleted again at 6000 rpm for 60 minutes, and the clear supernatants were decanted. For anionic polymer stabilization, the nanorod pellets were resupsended with 4.5 mL of a solution containing 30 mg/mL poly(sodium 4-stryene-sulfonate) (PSS, Aldrich, #243051) and 1 mM NaCl. For PEGylation, the nanorod pellets were resuspended with 4.5 mL of a solution containing 200 μM K_2CO_3 and 10 μM mPEG-SH (Nektar Therapeutics, #2M4E0H01). For both stabilization methods, the nanorod solution was incubated overnight at room temperature. Subsequent rounds of sedimentation, decantation, and resuspension with water were then carried out as described above to lower the CTAB concentration.

CTAB Dilution

CTAB dilution was carried out by two methods. For the data in Figure 1, the CTAB was diluted by subsequent rounds of sedimentation, decantation, and resuspension with water as described in the preceding section, except that no stabilizing agent was applied. For the data in Figure 2, a 600 μL aliquot of nanorods diluted to 1.4 mM CTAB was put in a custom 9 mL cuvette for spectral analysis. The plasmon resonant spectral extinction was monitored as water was added to the solution at 20 μL/min with a pipette pump.

Chloroform Extraction

A separatory funnel was filled with 100 mL of chloroform and 10 mL of nanorod solution which contained 30 mM CTAB. The mixture was vigorously shaken and allowed to separate over night. The

aqueous nanorod solution was extracted and 500 μL aliquots were placed in test tubes. To these tubes were added increasing quantities of chloroform for a second extraction: 0, 50, 100, 150, 200, 250, and 300 μL. After vigorous mixing, these were allowed to separate over night. The aqueous nanorod solutions were then removed and analyzed.

Nanorod Bioconjugation

Nanorods were stabilized with the heterobifunctional linker α-thio-ω-carboxy poly(ethylene glycol) (Iris Biotech, #HOOC-PEG-SH) by the PEGylation method described above and resuspended in 100 mM 2-(N-morpholino)ethanesuflonic acid (MES) buffer (Sigma, #M-0164) at pH 6.1. The nanorods were concentrated by sedimentation to a volume of 100 μL with an absorbance value greater than 10 at the LSPR peak wavelength. 96 mg of 1-ethyl-[3-dimethylaminopropyl]carbodiimide (EDC, Sigma, #1769) and 29 mg of N-hydroxysuccinimide (NHS, Sigma, #1306762) were added to 10 mL of MES buffer, mixed, and then 10 μL of this solution was immediately added to the 100 μL nanorod solution. This mixture was allowed to sit for 15 minutes, during which 0.5 mL of 2-mercaptoethanol was diluted into 14.5 mL MES buffer. After the 15 minute incubation, 10 μL of the diluted 2-mercaptoethanol was added to the nanorod solution. This mixture was allowed to sit for 10 minutes, after which 400 μL of the antibody solution at 2 mg/mL in PBS pH 7.1 was added. This final 500 μL NR/Ab solution was incubated for 2 hours at room temperature. Finally, the NR-Ab conjugates were separated from excess reactants and byproducts by sedimentation at 10,000 rpm, decantation, and resuspension of the pellet in PBS buffer.

Fluorimetry

The procedure above was followed with an Alexa Fluor 488 labeled rabbit IgG (AF-Ab, Invitrogen, #A11059). Upon completion, the AF-Ab-NR conjugates were put through subsequent rounds of sedimentation, 90% decantation, and resuspension in PBS. The supernatants and the final AF-Ab-NR

conjugate solutions were analyzed in a Horiba Jobin-Yvon FluoroLog-3 fluorimeter with CW Xenon excitation. The free AF-Ab in the supernatants served as a standard curve to determine the concentration of AF-Ab bound to the nanorods.

Nanoparticle ELISA

Gold nanorods conjugated to mouse anti-human HER2 antibodies (NeoMarkers, #MS-301-PABX) were incubated with horseradish peroxidase-labeled anti-mouse IgG (Sigma, # A4416) for 1 hour. Nonspecific reaction sites were blocked with a 3% solution of bovine serum albumin. Nanorods were rinsed twice by sedimentation and resuspension in 3% bovine serum albumin to remove any unbound IgG. The HRP bound to the nanorod conjugates was developed with 3,3',5,5'-tetramethylbenzidine dihydrochloride (Sigma, #T3405) and compared with a HRP anti-mouse IgG standard curve by determining the absorbance at 450 nm with a spectrophotometer.

Nanorod Targeting

Anti-HER2 nanorod conjugates were incubated with two cell types: the HER2-overexpressing epithelial breast cancer cell line SK-BR-3 and the normal mammary epithelial cell line MCF10A (American Type Culture Collection). The SK-BR-3 cells were grown in McCoy's 5A medium supplemented with 10% fetal bovine serum and 1% penicillin-streptomycin and maintained at 37ºC in a 5% CO_2 atmosphere. The MCF10A cells were cultured in Mammary Epithelial Basal Medium supplemented with a BulletKit (Clonetics) and also maintained at 37ºC in 5% CO_2. Both cell lines were prepared for the experiment by putting 6 x 10^5 cells in chambered coverslips and allowing them 30 minutes to attach to the surface. The cells were rinsed once with PBS, then incubated with nanorod conjugates for 1 hour in 5% CO_2 at 37 C. The LSPR peak absorbance of the nanorod conjugate solutions was 1.5. After the incubation, cells were rinsed 3x with 1x PBS and then the appropriate cell media was added prior to imaging. The cells were imaged by two photon microscopy at 50X with 780 nm illumination and 400 – 700 nm detection.

The KU7 cells were grown in MEM medium supplemented with 10% fetal bovine serum and 1% penicillin-streptomycin and maintained at 37C in a 5% CO2 atmosphere. The cell line was prepared for the experiment by putting 4 x 10^5 cells on cover slips and allowing them 24 hrs to attach to the surface. Prior to the treatment, the cell media was changed to OptiMEM (Roche Biochemicals) and nanorod-C225 conjugates were added for 4 hours. After 4 hrs, the OptiMEM media was changed to MEM medium supplemented with 10% serum and incubated in 5% CO_2 at 37C atmosphere for another 20 hrs. Twenty-minutes prior to fixation, the cells were rinsed once with warm PBS, then incubated with 100 nM Alexa-488-wheat germ agglutinin (WGA) and left for 10 min in the cell incubator for WGA cellular internalization. After 10 min the cells were rinsed three times with warm PBS, fixed in 1:1 methanol:ethanol at 20C for 10 minutes, then washed three times with cold PBS and mounted on slides using Slow-Fade Antifade. All reagents were purchased from Molecular Probes. Imaging was carried out with a Leica SP5RS AOBS confocal microscope using a 63x/1.4 objective. Nanorods were detected with 633 nm illumination in reflection mode. WGA-AF488 was excited at 488 nm and detected at 495-530 nm.

3. Results

Nanorod Stability

In order to determine the critical CTAB concentration required for nanorod stability, nanorod solutions were heated to melt the CTAB crystals and provide a well-defined initial concentration of 100 mM. Aliquots of nanorods were then pelleted by sedimentation, 90% of the clear supernatant was removed, and the nanorod pellets were resuspended to their initial volume with water. In this way the CTAB concentration was reduced by a factor of 10 on each round of sedimentation. Note that the quantity of CTAB bound to the nanorod surfaces is a negligible fraction of this initial CTAB

concentration.[†] The LSPR peak wavelength, width, and height were recorded after each round of sedimentation and are plotted in Figure 1. There was essentially no nanorod aggregation, *i.e.,* no LSPR peak height reduction, broadening, or red shift, until the third round of sedimentation. Therefore, nanorod aggregation is expected to occur somewhere between 1 and 0.1 mM CTAB.

To further characterize the critical CTAB concentration, the LSPR spectrum of a nanorod solution was monitored during slow dilution with water (Figure 2). As expected, the LSPR peak absorbance decreased as the nanorod concentration was reduced. However, the LSPR peak wavelength and width were not affected, indicating that there was no aggregation, although the CTAB concentration was reduced to below 50 μM. This apparent inconsistency with the results of Figure 1 reveals that it is the ratio of CTAB concentration to nanorod concentration that determines stability, not the CTAB concentration alone, which is typical for surfactant-stabilized colloids. To further confirm this point, CTAB was removed from a nanorod solution without reducing the nanorod concentration by extraction with chloroform. As seen in Figure 3, there was a critical CTAB concentration at which aggregation occurred. Based on our own measurement of the distribution ratio for CTAB between water and chloroform, the aggregation occurred between 370 μM and 290 μM CTAB. Given that the nanorod concentration was 0.5 nM, the critical CTAB/nanorod concentration ratio was approximately 740,000. Note that this number of CTAB molecules per nanorod is much larger than the amount of CTAB needed to simply coat the nanorods with a surfactant bilayer (see footnote above), so the dynamic interactions between CTAB in solution and in the bilayer must be important for nanorod stability.

Nanorods were stabilized by displacement of the CTAB with a thiol-terminal polyethylene glycol (mPEG-SH), and by wrapping the CTAB bilayer with polystyrene sulfonate (PSS). The LSPR peak

---

[†] Consider the typical conditions of a nanorod solution with l = 5nm d = 15 nm nanorods at LSPR peak abosrbance of 1, which corresponds to a nanorod concentration of 0.2 nM. The nanorod surface area would be 3063 nm2. The CTAB bilayer packing area is 22 A2. Therefore, each nanorod would contain 14,000 CTAB molecules on its surface, taking up only 2.8 mM of the CTAB concentration.

wavelength, width, and height after successive rounds of sedimentation are displayed in Figure 1 to probe the effectiveness of these stabilizers. While the unstabilized nanorods aggregated after the third round of sedimentation as described above, both PEGylation and polyelectrolyte stabilization were effective. However, PEGylation maintained a narrower LSPR peak, indicating a reduced degree of aggregation relative to polyelectrolyte stabilization.

Nanorod Bioconjugation

To form stable nanorod bioconjugates, a heterobifunctional polyethylene glycol with thiol and carboxyl end groups (HOOC-PEG-SH) was applied. Nanorod stabilization with HOOC-PEG-SH yielded identical results to mPEG-SH in Figure 1. The carboxy-terminal nanorods were conjugated to antibodies using the zero-length crosslinker EDC stabilized by NHS.[38] Standard procedures for EDC protein crosslinking were followed,[39] with the following modifications for the unique properties of the carboxy-terminal nanorods. First, since the functionalized nanorod surfaces contain no amines, there is no chance of nanorod aggregation due to amide bond formation between nanorods, which minimizes the criticality of the initial EDC exposure. Second, to avoid the need for buffer exchange or sedimentation, the change in pH from 6.1 for activation to 7.1 for conjugation was accomplished by diluting the nanorods into a larger volume of antibody solution. Finally, sedimentation was performed (rather than buffer exchange) to remove excess reactants and products from the nanorod solution.

As a means to confirm the altered nanorod surface chemistry at various stages, zeta potential measurements (Malvern Zetasizer Nano) were performed on gold nanorods in the original CTAB, after stabilization with HOOC-PEG-SH, and finally after Ab conjugation. The results, presented in Table 1, are consistent with the cationic, anionic, and zwitterionic surface charges, respectively, associated with these three states of nanorods.

To characterize the final product, nanorods were conjugated to AF-Ab for fluorimetric analysis. After the steps described above, the nanorod conjugates were put through successive rounds of sedimentation,

90% decantation, and resuspension in buffer to dilute the unbound AF-Ab by factors of ten. Fluorimetry of unbound AF-Ab in the decants, shown in Figure 4, serves as a standard curve and reaches the background fluorescence noise floor by the 4th round at an AF-Ab concentration of 0.1 nM. Fluorimetry of the nanorod conjugates solution indicated a nanorod bound AF-Ab concentration of 1 nM, which yields approximately two antibodies per nanorod given a nanorod concentration of 0.5 nM based on the LSPR extinction peak.[17]

To further characterize the nanorod conjugates, a nanoparticle ELISA was performed.[40] This method is similar to a traditional ELISA except that the immunosorbent surface is that of the nanoparticles in solution. The nanoparticle ELISA yielded 2.28 +/- 0.05 antibodies per nanorod, in reasonable agreement with the fluorimetry results. A simultaneous ELISA on nanorods prepared with mPEG-SH, and therefore no capture antibodies, yielded 0.68 +/- 0.2 antibodies per nanorod. This signal may be an artifact due to chemisorption of the label antibody to available gold surface on the nanorods.

Nanorod Targeting and Imaging

Nanorod conjugate targeting was tested with two in vitro systems. First, nanorods were conjugated to anti-HER2 and also to rabbit IgG as a control. Each conjugate was incubated with both the HER2-overexpressing epithelial breast cancer cell line SK-BR-3 and the normal mammary epithelial cell line MCF10A for 30 minutes simultaneously and under identical conditions. The cells were washed and immediately imaged live by two photon luminescence, which highlights the presence of gold particles,[18] as well as phase contrast to show the cell locations. Figure 5 demonstrates that only the specific antibody/cell produced a significant level of nanorod binding to the cells. Figure 6 displays dark field images of targeted and control cells from the same sample. The nanorods were not visible. To gauge their visibility in dark field microscopy, isolated nanorods were deposited on glass substrates near alignment marks and easily visible spherical gold nanoparticles so that optical microscopy and

AFM could be performed on the same area (see Figure 7). The nanorod was not detectable on both high-sensitivity monochrome and color CCD cameras.

The conjugation method was also tested with C225 antibodies and human IgG antibodies as a control. In this case, the nanorod conjugates were incubated with the KU7 bladder cancer cell line, which overexpresses the receptor bound by C225. The nanorods were imaged by confocal reflectance and the cells were visualized with a fluorescent WGA label. The C225 conjugates were more strongly associated with KU7 cells than the control IgG conjugates, as seen in Figure 8.

4. Discussion

It is well known that the CTAB surfactant responsible for gold nanorod synthesis is also required to maintain colloidal stability. However, the CTAB concentration at which colloidal stability is lost has not been well characterized. This is due to several factors. First, to reduce the CTAB concentration in a nanorod solution, it is often removed by sedimentation of the nanorods into a pellet, decantation of the CTAB solution, and resuspension of the nanorod pellet in water. If this procedure is not performed analytically, the CTAB concentration is reduced by an unknown amount. Second, nanorod synthesis is carried out at 100 mM CTAB, which is above the saturation concentration at room temperature. Upon storage, some of the CTAB crystallizes, leaving an unknown concentration in the nanorod solution drawn from the solution phase. Finally, attempts at spectroscopic or other analyses of the CTAB concentration are hindered by micellization and association with gold and silver ions in solution.

That the nanorods were found to be entirely stable to a CTAB concentration below 1 mM may confound the development of methods to stabilize nanorods, since the CTAB may stabilize the nanorods when it is thought to be removed. Nanorod stabilization outside of CTAB solution is further complicated by several factors. First, the aggregation occurs quite suddenly when the CTAB concentration falls below the critical value, as seen in Figure 3. Second, the fact that it is the ratio of

CTAB to nanorod concentrations that determine stability, rather than the CTAB concentration alone, means that the critical CTAB concentration for a given sample will depend on the nanorod concentration. Third, since CTAB forms a bilayer on the nanorod surface, it is likely that the available nanorod surface area is critical for stability rather than the nanorod concentration. Therefore, the critical CTAB concentration for a given sample also depends on nanorod size. This significant variability of the critical CTAB concentration between samples may in part account for reproducibility issues in stabilizing gold nanorods and forming bioconjugates.

We previously described a strategy to stabilize gold nanorods with a thiol-terminal polyethylene glycol (mPEG-SH) which displaces the CTAB bilayer so that CTAB can be reduced to an arbitrarily low concentration and the nanorods remain in solution.[17] Nanorods can also be stabilized by wrapping them with anionic polymers which are attracted to the cationic CTAB bilayer, as well as by forming multiple polyelectrolyte layers.[26] Figure 1 displays a comparison of the effectiveness of these methods for stabilizing nanorods. Interestingly, after the first and second rounds of sedimentation, the sample with no stabilizing treatment maintained the best spectrum, although aggregation occurred rapidly thereafter. The data demonstrate that upon removal of CTAB, PEGylation via the thiol-gold bond results in higher yields and a narrower LSPR linewidth than electrostatic stabilization. This spectroscopic result is in agreement with previously reported microscopic characterizations of nanorod substrates. PEGylated nanorod solutions yield highly monodisperse nanorods when deposited on glass substrates,[17] while electrostatic wrapping leads to aggregated nanorods.[26]

Most gold nanorod targeting experiments to date have been carried out by stabilizing the CTAB-capped gold nanorods with polyelectrolytes, then non-covalently binding antibodies or other targeting agents to the nanoparticles by simply mixing them together.[12, 29, 31-33, 35, 36] This is similar to the original strategies developed to bind antibodies to citrate capped gold nanoparticles for immunoelectron microscopy.[41] The binding is likely due to weak electrostatic and hydrophobic interactions between

the nanoparticles and antibodies. To create more stable nanorod bioconjugates, the strategy described here relies on an amide bond between the linker and antibody, and a strong gold-thiol bond[42] between the linker and nanorod. In some cases polyelectrolytes with exposed carboxyl groups for amide bond formation with antibodies have been employed.[30, 37] In one case an alkanethiol was used in a similar manner to the bifunctional PEG describe here.[43] While alkanethiols are more readily available, their low solubility in aqueous solutions required hours of sonication at elevated temperature to achieve sufficient concentration to displace the CTAB bilayer. Although more complicated, conjugates based on gold-thiol and covalent bonds will likely be more stable for in vivo applications. Furthermore, we have found the methods described here to be quite reproducible despite the strength of the original gold-CTAB interaction.[12] Tests of the nanorod zeta potential follow the intended surface chemistry, with a negative potential for carboxy-terminated nanorods, and a near neutral potential for the zwitterionic protein conjugates. The fluorimetric assay yields approximately two antibodies per nanorod, and the ELISA assay demonstrates that a large fraction of these antibodies are active. Finally, figures 5 and 8 demonstrate successful targeting in two cell types with different antibodies.

We have also investigated the effectiveness of different imaging modalities to visualize nanorods in and around cells. As described previously,[18] the images based on two photon luminescence in Figure 5 clearly reveal nanorods in the specific sample. Dark field microscopy is a much simpler modality that can yield striking images of plasmon resonant nanoparticles.[44] However, the optical scattering which provides dark field contrast is a strong function of nanoparticle size. Furthermore, the size range at which nanoparticles become visible by dark field is 10's of nanometers, similar to the range of nanoparticles that have been pursued for biomedical applications. Issues of visibility are also sensitive to the illumination and imaging numerical apertures, spectral range, nanoparticle aggregation, and background scattering from cells. Therefore, one must be cautious when interpreting nanoparticle targeting results by dark field microscopy. For example, the dark field images from Figure 6 reveal no

evidence of scattering by the nanorods, even though the two-photon images from Figure 5 confirm the presence of nanorods in the same sample. In this case the single nanorods do not scatter sufficiently to be visible against the scattering from cells. To further confirm this point, dark field images of a single nanorod on a glass substrate are displayed in Figure 7. Although the location of a single gold nanorod relative to a larger spherical particle and alignment marks was confirmed by atomic force microscopy, the nanorod was not visible in the dark field images taken with either a color CCD camera or a back-illuminated electron multiplying CCD camera. If the single nanorods are not visible in dark field microscopy on a flat glass substrate, it is not surprising that can be invisible in the higher background dark field images of cells in Figure 6. These results suggest that the successful targeting results of Figure 5, detected by two photon luminescence, must represent individual or very small clusters of nanorods not detectable by dark field microscopy. There are many methods to increase the nanorod imaging signal and contrast without resorting to two-photon luminescence, such as spectrally filtering the scattered light, exciting with monochromatic illumination at the plasmon resonant wavelength, and using a higher numerical aperture condensers and objectives. Figure 8 reveals that confocal reflectance microscopy, with monochromatic illumination at the LSPR wavelength and reduced background signal, is sufficient to detect targeted nanorods in KU7 cells. An important future study will be to quantitatively compare two photon and confocal reflectance nanorod contrast in identical cell samples.

5. Conclusions

To maintain colloidal stability, it is the ratio of CTAB to nanorod concentration that must be maintained. Here, the critical CTAB:nanorod ratio was found to be approximately 740,000:1. The CTAB layer can be displaced by thiol terminal PEG, or wrapped by polyelectrolytes. However, gold-thiol PEGylation results in higher yields and more monodisperse nanorod samples when the CTAB is removed. A bifuncitonal PEG with thiol and carboxyl end groups results in carboxy-terminal

PEGylated nanorods which can be conjugated to antibodies via a carbodiimide linking agent. Fluorimetry and ELISA assays reveal approximately two antibodies per nanorod. The nanorod conjugates demonstrated specific targeting in two different antibody/cell systems. Two photon luminescence and confocal reflectance microscopies successfully imaged the nanorods in cells.

Acknowledgements

Hafner acknowledges support from the National Science Foundation's Nanoscale Science and Engineering Initiative under award no. EEC-0647452, the U.S. Army Research Office under grant no. W911NF-04-1-0203, and the Welch foundation under grant C-1556. Hafner and Adam acknowledge support from the Department of Defense grant W81XWH-06-2-0067 to UTHSC. Anderson acknowledges support from the NSF-funded Integrative Graduate Research and Educational Training program DGE-0750842. Drezek acknowledges support from the Department of Defense grant W81XWH-07-1-0428.

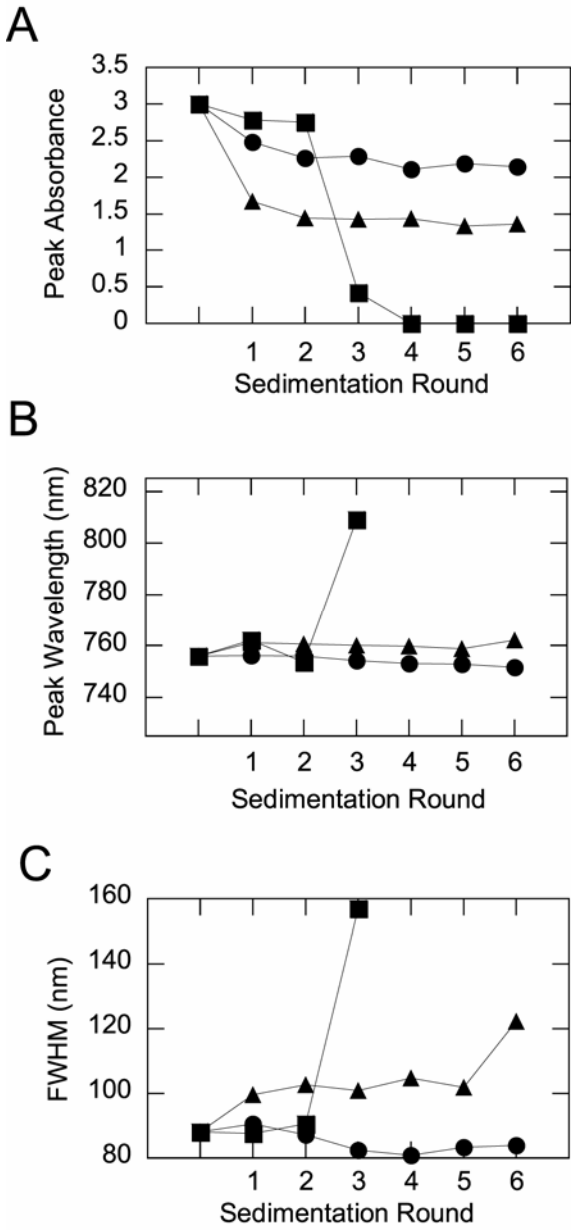

Figure 1. The evolution of the plasmon resonant peak of nanorod solutions after reduction of the CTAB concentration by sedimentation. The absorbance peak height (A), peak wavelength (B), and peak width (C) for CTAB stabilized gold nanorods (■), anionic polymer stabilized gold nanorods (▲), and PEGylated nanorods (●).

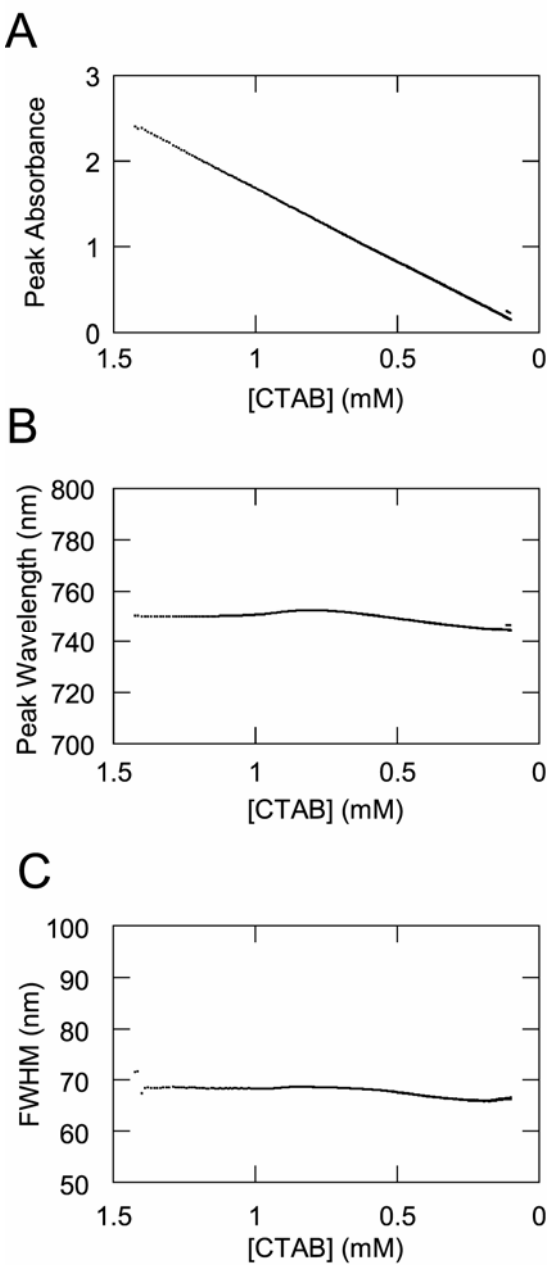

Figure 2. The evolution of the plasmon resonant peak height (A), wavelength (B), and width (C) of a nanorod solution during dilution with water (all graphs display individual data points).

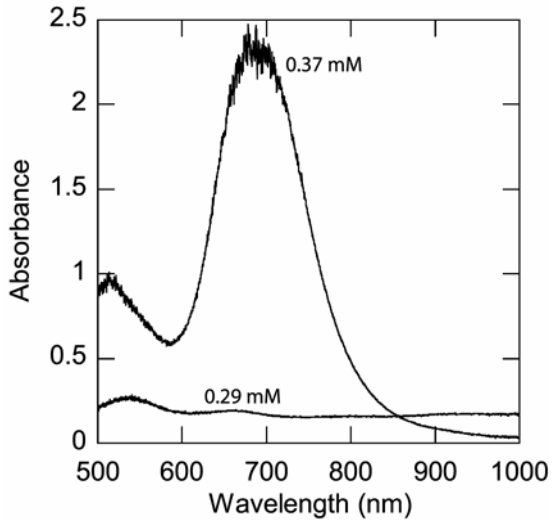

Figure 3. The plasmon resonant extinction spectra of nanorod solutions at two CTAB concentrations achieved by chloroform extraction. The nanorod concentration was 0.5 nM.

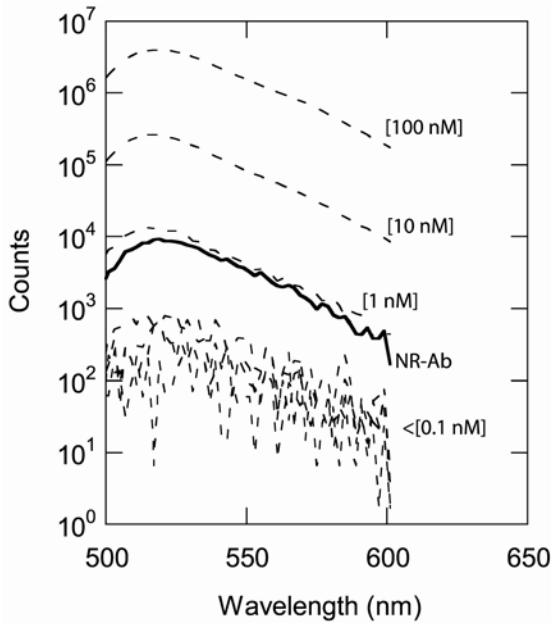

Figure 4. Fluorimetric analysis of gold nanorod conjugates. The dashed curves display the signal from free labeled antibodies in solution at the stated concentrations. The solid curve displays the signal from nanorod conjugates.

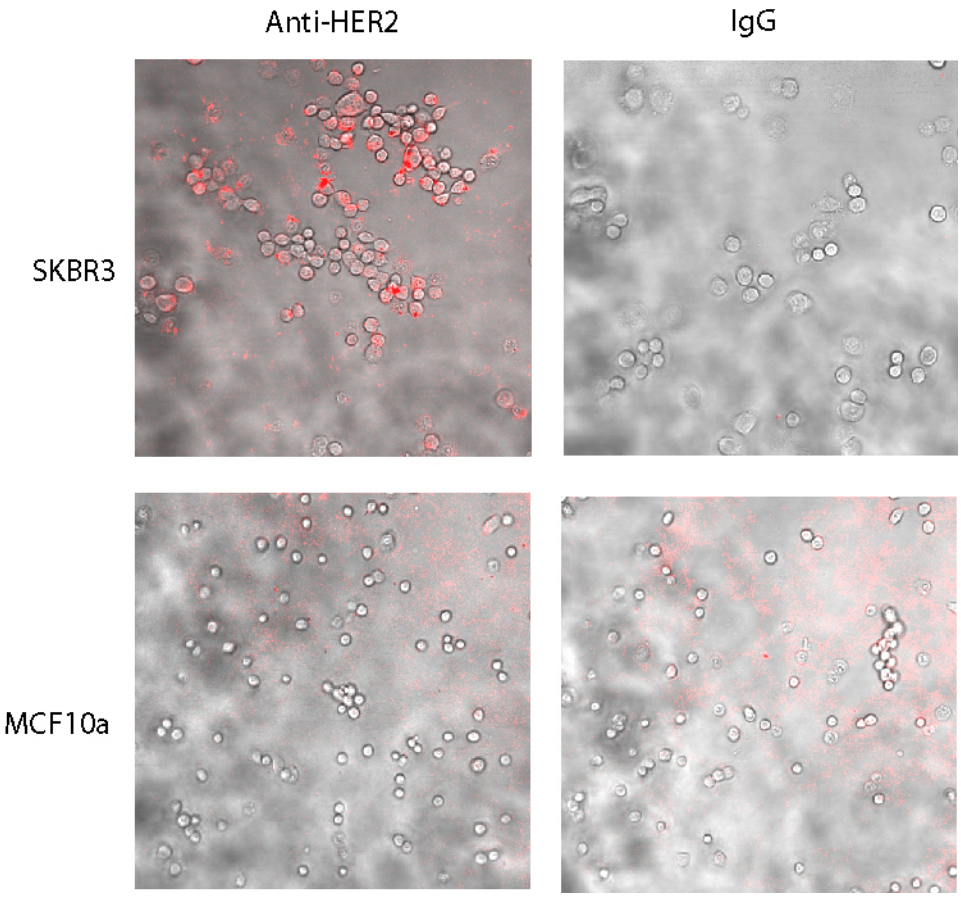

Figure 5. Nanorod conjugate targeting. Phase contrast shows the cell locations in grayscale, and two photon luminescence is displayed in red. Binding was only observed for the Anti-HER2 conjugates and SKBR3 cells.

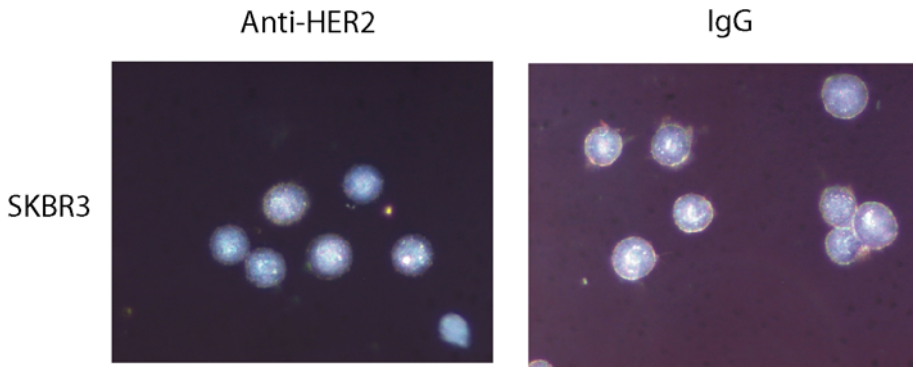

Figure 6. Dark field microscopy images of the same samples as in Figure 5.

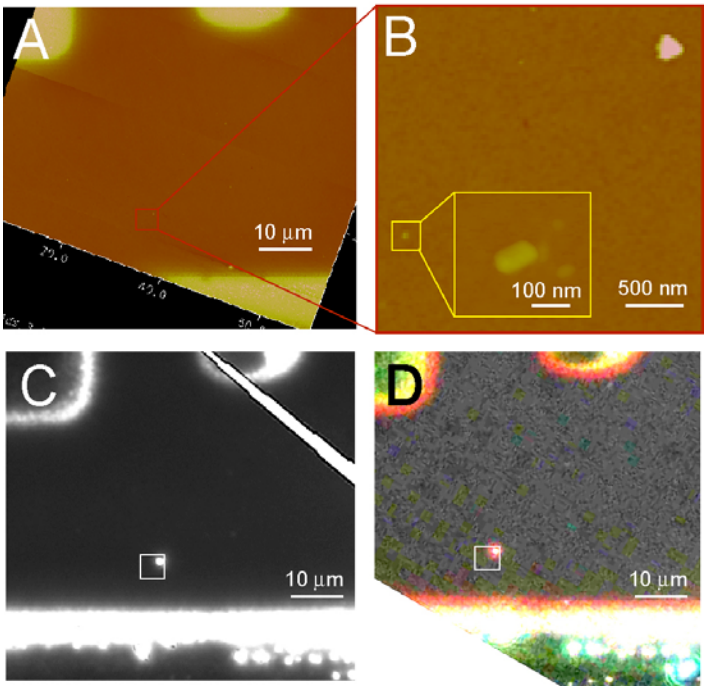

Figure 7. Dark field microscopy images of a single gold nanorod on glass. The first AFM image (A) shows a region near alignment marks that are also visible in the optical images (C and D). A zoomed AFM image (B) reveals a large nanosphere in the upper right (triangular shape is a tip artifact) and a nanorod in the lower left. The nanorod is clearly revealed in the inset. Its size is exaggerated by the tip. The true size is approximately 50 nm length and 15 nm width. Dark field images captured with a high sensitivity CCD (C) and color CCD (D) clearly show the nanosphere, but show no sign of the nanorod in the expected region, even with significant contrast enhancement. The inset boxes in A, C, and D are all shown at the same size and position.

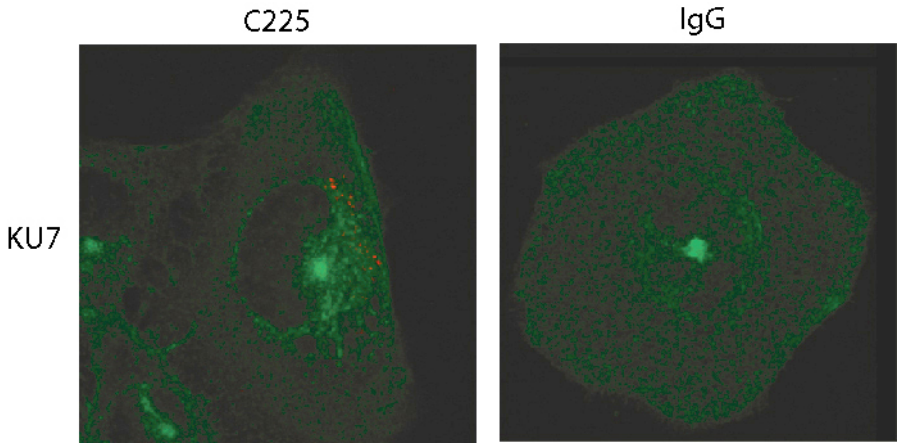

Figure 8. In vitro nanorod imaging by confocal reflectance. WGA-AF488 fluorescence shows the cell location in green, and confocal reflectance at 633 nm is shown in red. Nanorod binding is only observed for the specific C225 conjugates and KU7 cells.

TABLES.

Nanoparticle	**ZP (mV)**
NR-CTAB	+83
NR-S-PEG-COOH	-19
NR-S-PEG-Ab	-6

Table 1. Zeta Potential measurements to confirm surface chemistry modification.

REFERENCES.

1. Link, S.; El-Sayed, M. A., Spectral Properties and Relaxation Dynamics of Surface Plasmon Electronic Oscillations in Gold and Silver Nanodots and Nanorods. *Journal of Physical Chemistry B* **1999,** 103, 8410-8426.
2. Liao, H.; Nehl, C. L.; Hafner, J. H., Biomedical applications of plasmon resonant metal nanoparticles. *Nanomedicine* **2006,** 1, (2), 201-208.
3. Jain, P. K.; Huang, X. H.; El-Sayed, I. H.; El-Sayed, M. A., Noble Metals on the Nanoscale: Optical and Photothermal Properties and Some Applications in Imaging, Sensing, Biology, and Medicine. *Accounts of Chemical Research* **2008,** 41, (12), 1578-1586.
4. Murphy, C. J.; Gole, A. M.; Stone, J. W.; Sisco, P. N.; Alkilany, A. M.; Goldsmith, E. C.; Baxter, S. C., Gold Nanoparticles in Biology: Beyond Toxicity to Cellular Imaging. *Accounts of Chemical Research* **2008,** 41, (12), 1721-1730.
5. Lal, S.; Clare, S. E.; Halas, N. J., Nanoshell-Enabled Photothermal Cancer Therapy: Impending Clinical Impact. *Accounts of Chemical Research* **2008,** 41, (12), 1842-1851.
6. Bikram, M.; West, J. L., Thermo-responsive systems for controlled drug delivery. *Expert Opinion on Drug Delivery* **2008,** 5, (10), 1077-1091.
7. Tong, L.; Wei, Q. S.; Wei, A.; Cheng, J. X., Gold Nanorods as Contrast Agents for Biological Imaging: Optical Properties, Surface Conjugation and Photothermal Effects. *Photochemistry and Photobiology* **2009,** 85, (1), 21-32.
8. Hleb, E. Y.; Hu, Y.; Drezek, R. A.; Hafner, J. H.; Lapotko, D. O., Photothermal bubbles as optical scattering probes for imaging living cells. *Nanomedicine* **2008,** 3, (6), 797-812.
9. Pirollo, K. F.; Chang, E. H., Does a targeting ligand influence nanoparticle tumor localization or uptake? *Trends in Biotechnology* **2008,** 26, (10), 552-558.
10. Sokolov, K.; Follen, M.; Aaron, J.; Pavlova, I.; Malpica, A.; Lotan, R.; Richards-Kortum, R., Real-time vital optical imaging of precancer using anti-epidermal growth factor receptor antibodies conjugated to gold nanoparticles. *Cancer Research* **2003,** 63, (9), 1999-2004.
11. Loo, C.; Lowery, A.; Halas, N.; West, J.; Drezek, R., Immunotargeted Nanoshells for Integrated Cancer Imaging and Therapy. *Nano Letters* **2005,** 5, (4), 709-711.
12. Javier, D. J.; Nitin, N.; Roblyer, D. M.; Richards-Kortum, R., Metal-based nanorods as molecule-specific contrast agents for reflectance imaging in 3D tissues. *Journal of Nanophotonics* **2008,** 2, -.
13. Yu, C. X.; Nakshatri, H.; Irudayaraj, J., Identity profiling of cell surface markers by multiplex gold nanorod probes. *Nano Letters* **2007,** 7, (8), 2300-2306.
14. Eghtedari, M.; Oraevsky, A.; Copland, J. A.; Kotov, N. A.; Conjusteau, A.; Motamedi, M., High sensitivity of in vivo detection of gold nanorods using a laser optoacoustic imaging system. *Nano Letters* **2007,** 7, (7), 1914-1918.
15. Huff, T. B.; Hansen, M. N.; Zhao, Y.; Cheng, J. X.; Wei, A., Controlling the cellular uptake of gold nanorods. *Langmuir* **2007,** 23, (4), 1596-1599.
16. Chen, C. C.; Lin, Y. P.; Wang, C. W.; Tzeng, H. C.; Wu, C. H.; Chen, Y. C.; Chen, C. P.; Chen, L. C.; Wu, Y. C., DNA-gold nanorod conjugates for remote control of localized gene expression by near infrared irradiation. *Journal of the American Chemical Society* **2006,** 128, (11), 3709-3715.
17. Liao, H.; Hafner, J., Gold nanorod bioconjugates. *Chemistry of Materials* **2005,** 17, (18), 4636-4641.

18. Wang, H.; Huff, T. B.; Zweifel, D. A.; He, W.; Low, P. S.; Wei, A.; Cheng, J.-X., In vitro and in vivo two-photon luminescence imaging of single gold nanorods. *Proceedings of the National Academy of Sciences of the United States of America* **2005,** 102, (44), 15752-15756.
19. Cang, H.; Sun, T.; Li, Z. Y.; Chen, J. Y.; Wiley, B. J.; Xia, Y. N.; Li, X. D., Gold nanocages as contrast agents for spectroscopic optical coherence tomography. *Optics Letters* **2005,** 30, (22), 3048-3050.
20. Skrabalak, S. E.; Chen, J.; Au, L.; Lu, X.; Li, X.; Xia, Y., Gold nanocages for biomedical applications. *Advanced Materials* **2007,** 19, (20), 3177-3184.
21. Nehl, C. L.; Liao, H. W.; Hafner, J. H., Optical properties of star-shaped gold nanoparticles. *Nano Letters* **2006,** 6, (4), 683-688.
22. Jana, N. R.; Gearheart, L.; Murphy, C. J., Wet chemical synthesis of high aspect ratio cylindrical gold nanorods. *Journal of Physical Chemistry B* **2001,** 105, (19), 4065-4067.
23. Sau, T. K.; Murphy, C. J., Seeded high yield synthesis of short Au nanorods in aqueous solution. *Langmuir* **2004,** 20, (15), 6414-6420.
24. Nikoobakht, B.; El-Sayed, M. A., Preparation and growth mechanism of gold nanorods (NRs) using seed-mediated growth method. *Chemistry of Materials* **2003,** 15, (10), 1957-1962.
25. Nikoobakht, B.; El-Sayed, M. A., Evidence for bilayer assembly of cationic surfactants on the surface of gold nanorods. *Langmuir* **2001,** 17, (20), 6368-6374.
26. Gole, A.; Murphy, C. J., Polyelectrolyte-coated gold nanorods: Synthesis, characterization and immobilization. *Chemistry of Materials* **2005,** 17, (6), 1325-1330.
27. Sun, Z. H.; Ni, W. H.; Yang, Z.; Kou, X. S.; Li, L.; Wang, J. F., pH-controlled reversible assembly and disassembly of gold nanorods. *Small* **2008,** 4, (9), 1287-1292.
28. Niidome, Y.; Honda, K.; Higashimoto, K.; Kawazumi, H.; Yamada, S.; Nakashima, N.; Sasaki, Y.; Ishida, Y.; Kikuchi, J., Surface modification of gold nanorods with synthetic cationic lipids. *Chemical Communications* **2007,** 2007, 3777-3779.
29. Tong, L.; Zhao, Y.; Huff, T. B.; Hansen, M. N.; Wei, A.; Cheng, J. X., Gold nanorods mediate tumor cell death by compromising membrane integrity. *Advanced Materials* **2007,** 19, (20), 3136-+.
30. Popovtzer, R.; Agrawal, A.; Kotov, N. A.; Popovtzer, A.; Balter, J.; Carey, T. E.; Kopelman, R., Targeted Gold Nanoparticles Enable Molecular CT Imaging of Cancer. *Nano Letters* **2008,** 8, (12), 4593-4596.
31. Huang, X. H.; El-Sayed, I. H.; Qian, W.; El-Sayed, M. A., Cancer cells assemble and align gold nanorods conjugated to antibodies to produce highly enhanced, sharp, and polarized surface Raman spectra: A potential cancer diagnostic marker. *Nano Letters* **2007,** 7, (6), 1591-1597.
32. Huang, X. H.; El-Sayed, I. H.; Qian, W.; El-Sayed, M. A., Cancer cell imaging and photothermal therapy in the near-infrared region by using gold nanorods. *Journal of the American Chemical Society* **2006,** 128, (6), 2115-2120.
33. Hu, R.; Yong, K. T.; Roy, I.; Ding, H.; He, S.; Prasad, P. N., Metallic Nanostructures as Localized Plasmon Resonance Enhanced Scattering Probes for Multiplex Dark-Field Targeted Imaging of Cancer Cells. *Journal of Physical Chemistry C* **2009,** 113, (7), 2676-2684.
34. Hauck, T. S.; Ghazani, A. A.; Chan, W. C. W., Assessing the effect of surface chemistry on gold nanorod uptake, toxicity, and gene expression in mammalian cells. *Small* **2008,** 4, (1), 153-159.
35. Durr, N. J.; Larson, T.; Smith, D. K.; Korgel, B. A.; Sokolov, K.; Ben-Yakar, A., Two-photon luminescence imaging of cancer cells using molecularly targeted gold nanorods. *Nano Letters* **2007,** 7, (4), 941-945.
36. Ding, H.; Yong, K. T.; Roy, I.; Pudavar, H. E.; Law, W. C.; Bergey, E. J.; Prasad, P. N., Gold nanorods coated with multilayer polyelectrolyte as contrast agents for multimodal imaging. *Journal of Physical Chemistry C* **2007,** 111, (34), 12552-12557.

37. Agarwal, A.; Huang, S. W.; O'Donnell, M.; Day, K. C.; Day, M.; Kotov, N.; Ashkenazi, S., Targeted gold nanorod contrast agent for prostate cancer detection by photoacoustic imaging. *Journal of Applied Physics* **2007,** 102, (6), -.
38. Grabarek, Z.; Gergely, J., Zero-Length Crosslinking Procedure with the Use of Active Esters. *Analytical Biochemistry* **1990,** 185, (1), 131-135.
39. Hermanson, G. T., *Bioconjugate Techniques*. 1st ed.; Academic Press: 1996; p 785.
40. Lowery, A. R.; Gobin, A. M.; Day, E. S.; Halas, N. J.; West, J. L., Immunonanoshells for targeted photothermal ablation of tumor cells. *International Journal of Nanomedicine* **2006,** 1, (2), 149-154.
41. Geoghegan, W. D.; Ackerman, G. A., Adsorption of Horseradish-Peroxidase, Ovomucoid and Antiimmunoglobulin to Colloidal Gold for Indirect Detection of Concanavalin-a, Wheat-Germ Agglutinin and Goat Antihuman Immunoglobulin-G on Cell-Surfaces at Electron-Microscopic Level - New Method, Theory and Application. *Journal of Histochemistry & Cytochemistry* **1977,** 25, (11), 1187-1200.
42. Nuzzo, R. G.; Zegarski, B. R.; Dubois, L. H., Fundamental-Studies of the Chemisorption of Organosulfur Compounds on Au(111) - Implications for Molecular Self-Assembly on Gold Surfaces. *Journal of the American Chemical Society* **1987,** 109, (3), 733-740.
43. Eghtedari, M.; Liopo, A. V.; Copland, J. A.; Oraevslty, A. A.; Motamedi, M., Engineering of Hetero-Functional Gold Nanorods for the in vivo Molecular Targeting of Breast Cancer Cells. *Nano Letters* **2009,** 9, (1), 287-291.
44. Mock, J. J.; Barbic, M.; Smith, D. R.; Schultz, D. A.; Schultz, S., Shape effects in plasmon resonance of individual colloidal silver nanoparticles. *Journal of Chemical Physics* **2002,** 116, (15), 6755-6759.

Nanotechnology **19** (2008) 315102 (6pp) doi:10.1088/0957-4484/19/31/315102

Enhanced multi-spectral imaging of live breast cancer cells using immunotargeted gold nanoshells and two-photon excitation microscopy

Lissett Bickford[1,3], Jiantang Sun[1,3], Kun Fu[1,2], Nastassja Lewinski[1], Vengadesan Nammalvar[1], Joseph Chang[1] and Rebekah Drezek[1,2,4]

[1] Department of Bioengineering, Rice University, Houston, TX 77005, USA
[2] Department of Electrical and Computer Engineering, Rice University, Houston, TX 77005, USA

E-mail: drezek@rice.edu

Received 18 April 2008, in final form 29 May 2008
Published 24 June 2008
Online at stacks.iop.org/Nano/19/315102

Abstract

We demonstrate the capability of using immunotargeted gold nanoshells as contrast agents for *in vitro* two-photon microscopy. The two-photon luminescence properties of different-sized gold nanoshells are first validated using near-infrared excitation at 780 nm. The utility of two-photon microscopy as a tool for imaging live HER2-overexpressing breast cancer cells labeled with anti-HER2-conjugated nanoshells is then explored and imaging results are compared to normal breast cells. Five different imaging channels are simultaneously examined within the emission wavelength range of 451–644 nm. Our results indicate that under near-infrared excitation, superior contrast of SK-BR-3 cancer cells labeled with immunotargeted nanoshells occurs at an emission wavelength ranging from 590 to 644 nm. Luminescence from labeled normal breast cells and autofluorescence from unlabeled cancer and normal cells remain imperceptible under the same conditions.

(Some figures in this article are in colour only in the electronic version)

1. Introduction

Accurate cancer diagnosis through its multi-stage progression is critical for developing effective and selective cancer treatments. In order to provide clinicians with functional diagnostic results, knowledge of the molecular signatures of carcinogenesis is necessary. Due to their overexpression during the development of cancer, several biomarkers have been identified as a biological means of characterizing these signatures [1]. Although the acquisition of molecular-specific data is typically associated with gene arrays and proteomics [2], there is an opportunity to use such biomarkers as tools for both *in vitro* and *in vivo* diagnostic evaluations of tissue specimens, such as during surgery, in order to identify malignant cells among heterogeneous tissue.

Silica-based gold nanoshells, which are advantageous for several biological applications due to their unique optical tunability and potential as multi-modal agents, have previously demonstrated enhanced diagnostic imaging potential of carcinogenesis at the microscopic scale through the use of extracellular biomarkers [3–6]. By manipulation of the size of their silica cores and gold outer shells, nanoshells can be optically tuned to absorb or scatter light from wavelengths ranging from the visible to the near-infrared, allowing for both imaging and therapy applications [7]. Achieving optimal contrast of gold nanoshells for biological diagnostics includes

[3] These authors contributed equally to this work, listed alphabetically by last name.
[4] Address for correspondence: Department of Bioengineering, Rice University, 6100 Main Street, MS-142, Houston, TX 77005, USA.

 © 2008 IOP Publishing Ltd Printed in the UK

a combination of developing nanoshells that are tuned to scatter or absorb light in the near-infrared (NIR), where biological chromophores absorb minimal light, and the use of NIR-based imaging systems.

Although several optical devices have been used to validate applications of gold nanoshells as viable contrast agents [3–15], none have focused on evaluating the effectiveness of using immunotargeted nanoshells as contrast agents for cell surface biomarkers using nonlinear excitation microscopy. Nonlinear optics has been used extensively for analyzing fluorescent signals in animal models and tissue samples [16–20]. By using a femtosecond pulsed laser, two photons can be used simultaneously to excite tissue molecules similar to the excitation generated by a single photon, but with twice the energy. Only the molecules at the focus of the femtosecond laser will be excited, resulting in greater resolution than that achievable with single-photon systems, such as conventional confocal microscopy. Additionally, unlike conventional confocal microscopy, a pinhole is not required to reject out-of-focus light and the inherent excitation at only the focal plane means that biological tissue undergoes less photodamage [20]. Although multi-photon microscopy has frequently been used for enhancing fluorescent signals [16, 20], studies have demonstrated that metal particles display photoluminescence as a result of excitation by such multi-photon systems [21, 22]. This photoluminescence is induced by a significant field enhancement that occurs upon multi-photon excitation of the metallic molecules [21]. Thus far in the literature, metallic nanoparticles analyzed for two-photon imaging potential have included gold colloid spheres [23, 24], gold nanorods [25–29], and gold nanoshells [14]. A recent publication on the use of two-photon microscopy for evaluating nanoshell contrast focused on potential dual imaging and therapy applications where unlabeled nanoshells were delivered to murine tumors through extravasations due to the presence of leaky vasculature [14]. However, since nanoshell dimensions are fundamentally variable [7], it is important to further elucidate and confirm the two-photon properties of these highly tunable nanoparticles despite differences in size. Furthermore, since cancer undergoes a multi-stage progression, the ability to track molecular signatures through the overexpression of biomarkers is crucial in obtaining functional and accurate diagnostic results. Therefore, the goal of our study was to demonstrate the nonlinear properties of very different-sized nanoshells and validate the proof of concept that immunotargeted nanoshells can be used to enhance the contrast of malignant human cells *in vitro* through nonlinear excitation prior to our evaluation of this system in excised tissue specimens. Additionally, through the use of two-photon excitation and multi-spectral imaging, the simultaneous acquisition of images at different emission wavelengths was obtained to ascertain the optimal imaging parameters for this system.

We demonstrate the two-photon luminescence properties of two different sizes of gold nanoshell designed with a similar plasmon resonance in the near-infrared. We evaluate the enhanced contrast by comparing HER2-overexpressing breast cancer cells to normal breast cells with and without targeted anti-HER2-bioconjugated gold nanoshells at five different emission wavelength ranges: 451–483, 483–515, 515–547, 558–579, and 590–644 nm. By evaluating imaging results under different ranges, we explore the broad emission properties of silica-based gold nanoshells under two-photon induced luminescence. The anti-HER2 antibody was selected as a model for surface tumor targeting due to the association of HER2-overexpression with more aggressive breast cancers seen in 15–25% of all breast cancer cases [30]. Additionally, studies in our laboratory have previously demonstrated the effectiveness of using immunotargeted nanoshells as diagnostic imaging agents for HER2-overexpressing cancer cells [3, 5, 6, 13]. We show that for immunotargeted nanoshells with a silica core diameter of 254 nm and a gold shell thickness of 19 nm imaged with our specific system, the optimal emission wavelength for observing enhanced contrast of HER2-overexpressing breast cancer cells occurs between 590 and 644 nm at 10% of maximum excitation power. Under similar conditions, normal breast cells are not detectable.

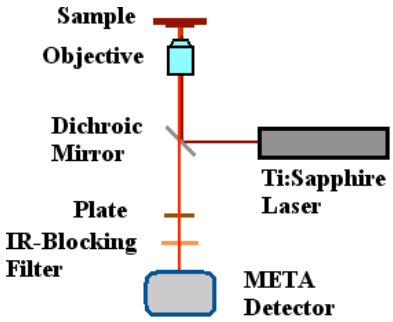

Figure 1. Schematic of Zeiss LSM 510 META multi-photon system configuration.

2. Method

2.1. Multi-photon imaging system

A Zeiss laser scanning microscope (LSM) 510 META multi-photon system was used in conjunction with a Coherent Chameleon femtosecond mode-locked Ti:sapphire laser to collect two-photon data (figure 1). The wavelength of the polarized output laser beam was tunable between 720 and 950 nm with pulse width of 140 fs at a repetition rate of 90 MHz. A short-pass dichroic mirror (KP700/488, Zeiss) was used to reflect the incident NIR excitation light onto the sample through a 20× or 63× objective and to collect the two-photon-induced luminescence data. To further eliminate the background signal of the excitation light, a wave plate and an IR-blocking filter (BG39, Zeiss) were placed in front of the META detector. The Zeiss LSM META system allowed simultaneous multi-spectral imaging and recording of up to eight emission channels. The maximum output power of the Chameleon femtosecond laser was around 1640 mW for excitation at 780 nm. Based on data from the manufacturer, less than 10% of this power was incident on the sample. The excitation wavelength of 780 nm was chosen as it was within 10 nm of the extinction peak for both nanoshell sizes.

2.2. Nanoshell fabrication

Nanoshells were developed as described in previous publications [3–5]. First, the Stöber method was used to create silica cores by reducing tetraethyl orthosilicate (Sigma Aldrich) in ammonium hydroxide and pure ethanol [31]. Aminopropyltriethoxysilane (APTES) was then added in order to terminate the silica core surfaces with amine groups, which formed functionalized particles. The two different-sized groups of silica particles were measured by scanning electron microscopy (SEM) to obtain the average silica core diameters of 130 and 254 nm. The gold shell overlay on the silica cores was also created using previously described methods [3–5]. First, using procedures outlined by Duff *et al* [32], gold colloid of 1–3 nm in diameter was developed and then aged under refrigeration for two weeks. The colloid was then concentrated using a Rotovap and added to the functionalized silica particles mentioned above. By interacting with the functionalized amine group surfaces of the silica particles, the gold colloid was adsorbed, forming surfaces with partial gold coverage. Addition of more gold completed the formation of the shell through catalysis of formaldehyde with hydrogen tetrachloroaurate trihydrate ($HAuCl_4 3H_2O$) and potassium carbonate. Two groups of nanoshells were fabricated and both were spectrally analyzed using a Varian Cary 300 UV–vis spectrophotometer (figure 2). The final sizes of the nanoshells were determined using SEM imaging (figure 2, inset) and confirmed using Mie theory simulation for multi-layer spheres. The smaller nanoshells had an average gold shell thickness of 21 nm. The larger nanoshells had an average shell thickness of 19 nm. The nanoshells were stored in deionized water at 4 °C until further use.

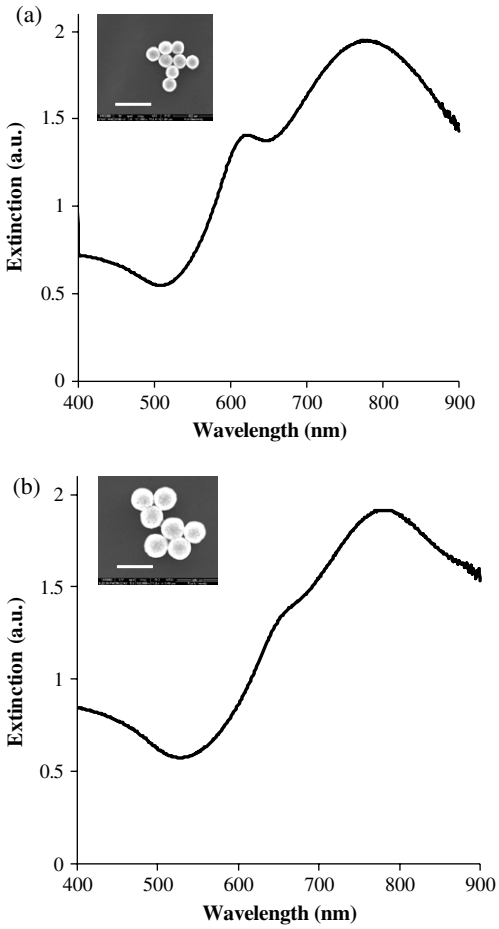

Figure 2. Measured extinction spectra of nanoshells. (a) Nanoshells of average core diameter 130 nm and average shell thickness of 21 nm. (b) Nanoshells of average core diameter 254 nm and average shell thickness of 19 nm. The insets depict corresponding images from scanning electron microscopy. Scale bars represent 450 nm.

2.3. Nanoshell surface modification and bioconjugation

For live cell imaging, the larger nanoshells were used and targeted to HER2-overexpressing cells through conjugations with anti-HER2 antibodies. In order to prepare the immunotargeted nanoshells, a heterobifunctionalized polyethylene glycol linker (orthopyridyl-disulfide-PEG-N-hydroxysuccinimide ester, OPSS-PEG-NHS, MW = 2 kD, CreativeBiochem Laboratories) was first conjugated to anti-HER2 antibodies (C-erbB-2/HER-2/neu Ab-4, Lab Vision Corporation) through amide linkages that joined the amidohydroxysuccinimide group (NHS) of the PEG linker to the antibodies. This reaction proceeded at a 3:1 molar ratio in sodium bicarbonate (100 mM, pH 8.5) on ice overnight. Aliquots of the 'PE-Gylated' antibodies, at a concentration of 0.4 mg ml^{-1}, were stored at −80 °C until use. Conjugation of the nanoshells to the PEGylated antibodies was then carried out through sulfur linkages between the gold nanoshell surfaces and the remaining OPSS group of the heterobifunctional PEG linker. This was performed by incubating the nanoshells, at a concentration of 1.6×10^9 particles ml^{-1}, with the PEGylated antibodies for 1 h under refrigeration (4 °C). In order to block vacant adsorption sites, the nanoshells were further incubated with a 10 μM polyethylene glycol-thiol cocktail (PEG-SH, MW = 5kD, Nektar) for two additional hours under refrigeration. Unbound antibodies were then removed by centrifugation and the immunotargeted nanoshells were then resuspended in deionized water. Prior to incubation with cells, the immunotargeted nanoshell solution was further modified by the addition of bovine serum albumin (BSA) and phosphate-buffered saline (PBS) to a final concentration of 1% each.

2.4. Cell preparation

SK-BR-3 cells (American Type Culture Collection, ATCC) were grown at 37 °C in a 5% CO_2 atmosphere using McCoy's 5A growth medium supplemented with 1% antibiotics and 10% fetal bovine serum (FBS). MCF10A cells (ATCC) were also grown at 37 °C in a 5% CO_2 atmosphere using Mammary Epithelial Basal Medium (MEBM) supplemented with a BulletKit (Clonetics) and 1% antibiotics. Both cell lines were grown in 25 cm^2 culture flasks until confluent, rinsed once with 1 × PBS, and incubated with trypsin-EDTA for 5 min at 37 °C in a 5% CO_2 atmosphere. The trypsin-EDTA was then neutralized with the appropriate culture medium and the cells were subsequently counted using a hemacytometer. For each cell line, an estimated 6×10^5 cells were placed in each of two 15 ml conical tubes and then centrifuged at 115 × *g* for 3 min. One cell pellet was resuspended in the immunotargeted

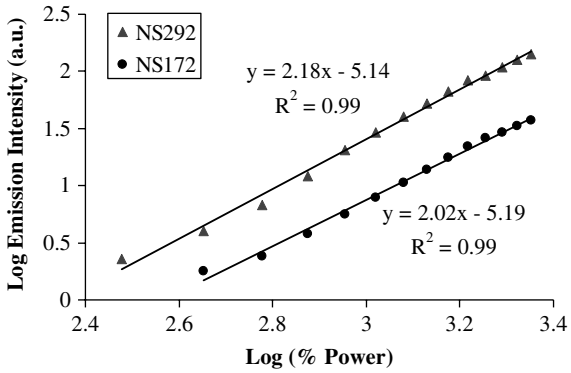

Figure 3. Quadratic dependence of luminescence intensity on excitation power at 780 nm for two different-sized nanoshells. Nanoshells of core diameter of 130 nm and shell thickness of 21 nm are designated as NS172. Nanoshells of core diameter of 254 nm and shell thickness of 19 nm are designated as NS292. Data were recorded with a 20× objective.

nanoshell solution and the other pellet was resuspended in an equal volume of 1 × PBS. The cells were then incubated at 37 °C in a hybridization chamber (VWR International) and rotated under a motor speed of 7 rpm for 10 min. Post incubation, the cells were centrifuged at 115 × *g* for 3 min, the supernatant was removed, and the cells were rinsed once with 1 × PBS. Following rinsing, the cells were resuspended in 10% glucose in 1 × PBS in order to maintain cell viability during imaging. The cell suspensions were then placed on chambered coverglasses (Fisher Scientific) prior to two-photon imaging.

3. Results and discussion

By manipulation of the core-to-shell ratio, nanoshells can be designed to strongly absorb or scatter light upon near-infrared excitation. In order to validate the two-photon characteristics of silica-based gold nanoshells, we designed two different sizes of nanoshell with a similar peak surface plasmon resonance in the near-infrared. After fabrication of two different-sized silica cores, their average diameters were confirmed through scanning electron microscopy (SEM) as 130 and 254 nm. Once the gold shell was added, the nanoshells were measured by SEM and their optical properties were assessed by UV–vis spectroscopy. The smaller nanoshells had an average diameter of 172 nm and a peak surface plasmon resonance at 772 nm; for the larger nanoshells, the average diameter was 292 nm, with a peak surface plasmon resonance occurring at 778 nm (both shown in figure 2). The two-photon luminescence properties of the gold nanoshells were then observed using a Zeiss LSM 510 META multi-photon system with the configuration shown in figure 1. The two-photon properties were verified by evaluating the dependence of increasing logarithmic emission intensity on increasing logarithmic excitation power. Aliquots of both sizes of bare nanoshell suspended in deionized water were well dispersed with sonication and separately placed on chambered coverglasses (Fisher Scientific). Data were recorded at an excitation wavelength of 780 nm, which corresponded to the peak plasmon resonance of the nanoshells for both sample sizes. The excitation power was varied from 2% to 15% of the maximum laser power with a detection spectral band of 494–634 nm. By using the image processing software inherent in the LSM 510 META system, the average intensities of the nanoshell suspensions were obtained. The dependence of luminescence intensity on excitation power at 780 nm for both smaller- and larger-sized nanoshells was determined (figure 3). The slopes of the fitted linear curves are estimated as 2.02 and 2.18 for the smaller and larger nanoshells, respectively, in accordance with the characteristic two-photon-induced quadratic dependence of emission intensity on excitation power [14, 16, 20]. Specifically, Wang *et al* demonstrated that the dependence of luminescence intensity on excitation power for gold nanorods ranged from 1.97 to 2.17 [27]. This disparity was attributed to possible nanoparticle melting after increasing the power on the nanorod sample and, subsequently, decreasing the power on the same sample. However, in our study, since a difference in quadratic dependence exists for two sizes of gold nanoshell treated under the same conditions, we believe that the nanoshells may actually undergo photophysics which are not yet fully elucidated.

In order to demonstrate the enhanced two-photon optical signatures of breast cancer cells labeled with immunotargeted nanoshells, the HER2-overexpressing epithelial breast cancer cell line, SK-BR-3, was analyzed and compared to the normal breast epithelial cell line, MCF10A, which does not overexpress HER2. For this component of the study, the cells were incubated with the larger nanoshells which were conjugated to anti-HER2 antibodies. Images were taken of the SK-BR-3 cancer cells under three conditions: labeled with nanoshells at 10% of maximum laser power, unlabeled at 10% of maximum laser power, and unlabeled at 100% of maximum laser power. An excitation wavelength of 780 nm was used for all images and five different emission wavelength ranges were analyzed: 451–483, 483–515, 515–547, 558–579, and 590–644 nm. Additionally, images were taken of the MCF10A normal cells under the same labeling and imaging conditions. As shown in figure 4(a), bright two-photon luminescence signals from nanoshells targeted to cell surface receptors provided clear visualization of the SK-BR-3 cancer cells under only 10% of maximum laser power. However, under the same power, unlabeled cancer cells were not perceivable (data not shown due to lack of detectable signal). By increasing the laser power to 100%, the spectral-resolved two-photon-induced autofluorescence is evident at emission wavelengths ranging from 451 to 547 nm (figure 4(b)). However, this autofluorescence, which is only visible at the maximized power, cannot be discerned beyond an emission wavelength of 547 nm. With regard to the normal MCF10A cells labeled with immunotargeted nanoshells under 10% of maximum laser power, clear visualization of the cells is not possible and only a few targeted cell surface receptors can be distinguished (figure 4(c)). Due to the differences in HER2 cell surface receptor expression, which is approximately 8×10^5 receptors per SK-BR-3 cancer cell [33] and about 1×10^4 receptors per normal MCF10A cell [34], the contrast was dramatically increased in the cancer cells due to the overexpression of HER2. Similar to the unlabeled

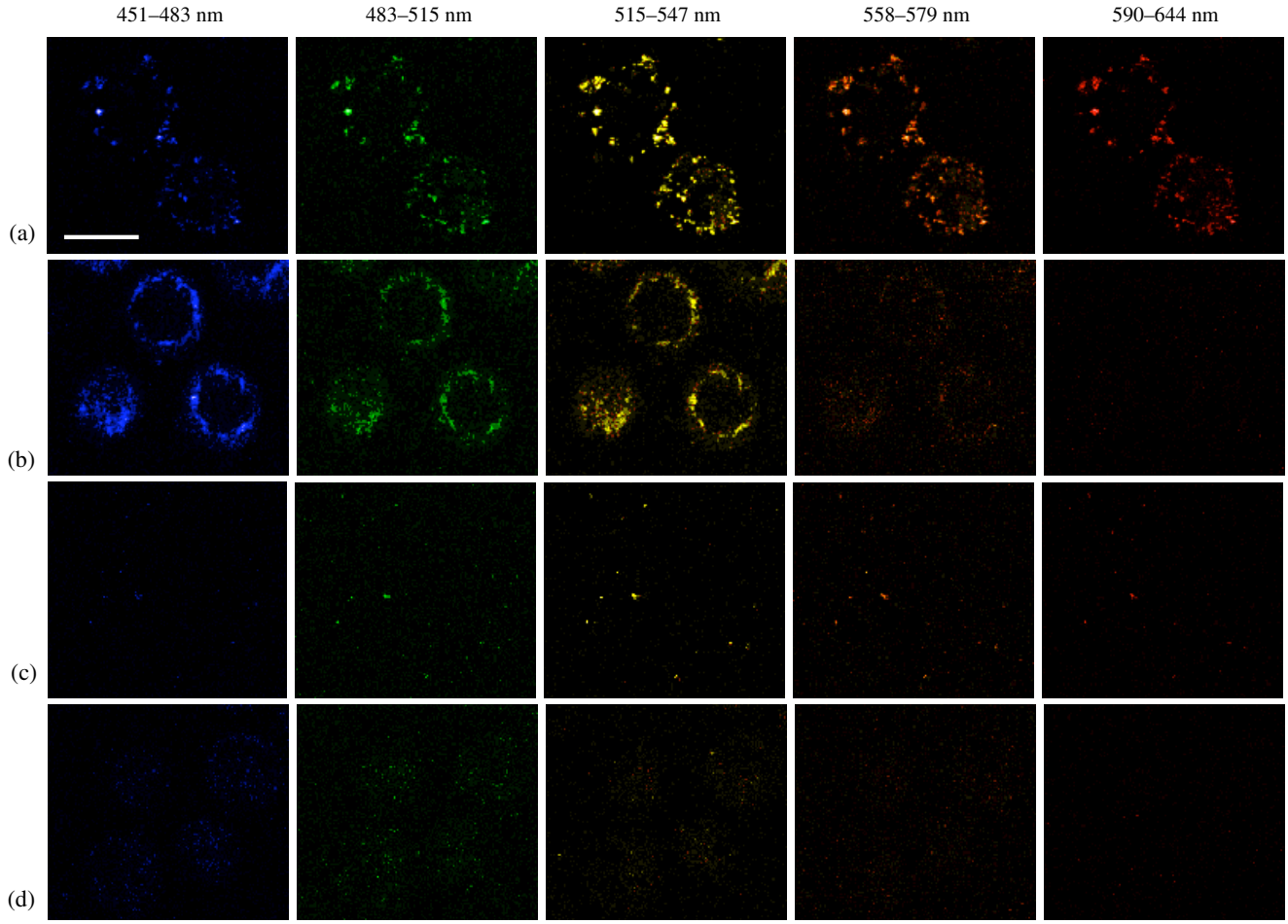

Figure 4. Two-photon images (pseudo color) of live SK-BR-3 cancer cells and MCF10A normal cells in suspension taken at different emission wavelengths. (a) Cancer cells labeled with larger nanoshells at 10% of maximum excitation power. (b) Unlabeled cancer cells at 100% of maximum excitation power. (c) Normal cells labeled with larger nanoshells at 10% of maximum excitation power. (d) Unlabeled normal cells at 100% of maximum excitation power. Images taken at 63×. The scale bar represents 20 μm.

SK-BR-3 cancer cells, unlabeled MCF10A cells imaged at 10% of maximum laser power were not detectable (data not shown due to lack of detectable signal). Furthermore, images collected at 100% of maximum laser power demonstrated that the MCF10A cells exhibited low levels of two-photon-induced autofluorescence (figure 4(d)). Wang *et al* [27] and Durr *et al* [29] have previously shown two-photon imaging results using gold nanorods. However, the images collected were taken over a single emission wavelength range from 400 nm to approximately 700 nm. Based on spectral-resolved image acquisition, however, the unique widely spanning luminescence properties of gold nanoshells demonstrate great flexibility in selecting the emission wavelengths necessary to minimize the influence of background autofluorescence. Photobleaching was also not observed under the two-photon-induced nanoshell luminescence. Based on a comparison of live cell bright-field images observed before and after laser exposure, morphological changes were not detected as a result of the aforementioned laser conditions and, in particular, all cell membranes remained visible and intact.

4. Conclusion

Two-photon microscopy is a powerful tool for diagnostic research applications. With advancements in gold-based contrast agent development and flexibility in two-photon excitation wavelength selection readily achieved through tunable laser sources, the potential to use multi-photon imaging for assessment of molecular signatures of malignancy is substantial. In this study, we demonstrate the first use of immunotargeted gold nanoshells as *in vitro* contrast agents for biomarkers of disease using two-photon microscopy. We additionally confirm broad luminescence from gold nanoshells using multi-spectral images to visualize the optical contrast provided by anti-HER2-nanoshells targeted to live HER2-overexpressing breast cancer cells. Our study identifies an additional application of immunotargeted nanoshells and suggests their potential future use as multi-functional probes for molecular imaging.

Acknowledgments

We thank Dr Robert Raphael for expert technical assistance using a Zeiss LSM META 510 system. We acknowledge

support from a Department of Defense Era of Hope Scholar Award to Rebekah Drezek, the Beckman Young Investigator Program, the Welch Foundation (C-1598), and the Center for Biological and Environmental Nanotechnology (EEC-0118007 and EEC-0647452).

References

[1] Hawk E, Viner J L and Lawrence J A 2000 *Curr. Oncol. Rep.* **2** 242–50
[2] Weinberg R A 2007 *The Biology of CANCER* (New York: Taylor and Francis) pp 727–32
[3] Loo C, Hirsch L, Lee M H, Chang E, West J, Halas N and Drezek R 2005 *Opt. Lett.* **30** 1012–4
[4] Lowery A R, Gobin A M, Day E S, Halas N J and West J L 2006 *Int. J. Nanomed.* **1** 149–54
[5] Loo C, Lowery A, Halas N, West J and Drezek R 2005 *Nano Lett.* **5** 709–11
[6] Fu K, Sun J, Bickford L R, Lin A W H, Halas N J, Yu T K and Drezek R A 2008 *Nanotechnology* **19** 045103
[7] Hirsh L R, Gobin A M, Lowery A R, Tam F, Drezek R A, Halas N J and West J L 2006 *Ann. Biomed. Eng.* **34** 15–22
[8] Gobin A M, Lee M H, Halas N J, James W D, Drezek R A and West J L 2007 *Nano Lett.* **7** 1929–34
[9] Wu C, Liang X and Jiang H 2005 *Opt. Commun.* **253** 214–21
[10] Zaman R T *et al* 2007 *IEEE J. Sel. Top Quantum Electron.* **13** 1715–20
[11] Fournelle M, Maass K, Fonfara H, Welsch H J, Hewener H, Günther C and Lemor R 2007 *IEEE Ultrason. Symp.* **1051-0117/07** 2417–20
[12] Agrawal A, Huang S, Lin A W H, Lee M H, Barton J, Drezek R A and Pfefer T J 2006 *J. Biomed. Opt.* **11** 041121
[13] Loo C 2006 *PhD Thesis* Rice University, Houston, Texas
[14] Park J *et al* 2008 *Opt. Express* **16** 1590–9
[15] Wang Y, Xie X, Wang X, Ku G, Gill K L, O'Neal D P, Stoica G and Wang L 2004 *Nano Lett.* **4** 1689–92
[16] Zipfel W R, Williams R M and Webb W W 2003 *Nat. Biotechnol.* **21** 1369–77
[17] Denk W, Strickler J H and Webb W W 1990 *Science* **248** 73–6
[18] Hell S W, Booth M, Wilms S, Schnetter C M, Kirsch A K, Arndt-Jovin D J and Jovin T M 1998 *Opt. Lett.* **23** 1238–40
[19] Lewis M K, Wolanin P, Gafni A and Steel D G 1998 *Opt. Lett.* **23** 1111–3
[20] Piston D W 1999 *Cell Biol.* **9** 66–9
[21] Boyd G T, Yu Z H and Shen Y R 1986 *Phys. Rev.* B **33** 7923–36
[22] Mooradian A 1969 *Phys. Rev. Lett.* **22** 185–7
[23] Huang X, Qian W, El-Sayed I H and El-Sayed M A 2007 *Lasers Surg. Med.* **39** 747–53
[24] Nagesha D, Laevsky G S, Lampton P, Banyal R, Warner C, DiMarzio C and Sridhar S 2007 *Int. J. Nanomed.* **2** 813–9
[25] Bouhelier A, Bachelot R, Lerondel G, Kostcheev S, Royer P and Wiederrecht G P 2005 *Phys. Rev. Lett.* **95** 267405
[26] Imura K, Nagahara T and Okamoto H 2005 *J. Phys. Chem.* B **109** 13214–20
[27] Wang H, Huff T B, Zweifel D A, He W, Low P S, Wei A and Cheng J X 2005 *Proc. Natl Acad. Sci.* **102** 15752–6
[28] Huff T B, Hansen M N, Zhao Y, Cheng J X and Wei A 2007 *Langmuir* **23** 1596–9
[29] Durr N J, Larson T, Smith D K, Korgel B A, Sokolov K and Ben-Yakar A 2007 *Nano Lett.* **7** 941–5
[30] National Comprehensive Cancer Network 2007 *Breast Cancer Treatment Guidelines for Patients* Version IX http://www.nccn.org
[31] Stöber W, Fink A and Bohn E 1968 *J. Colloid Interface Sci.* **26** 62–9
[32] Duff D G, Baiker A and Edwards P P 1993 *Langmuir* **9** 2301–9
[33] Hayes D F, Walker T M, Singh B, Vitetta E S, Uhr J W, Gross S, Rao C, Doyle G V and Terstappen L W M M 2002 *Int. J. Oncol.* **21** 1111–7
[34] Kornilova E S, Taverna D, Hoeck W and Hynes N E 1992 *Oncogene* **7** 511–9

Nanobiotechnol
DOI 10.1007/s12030-008-9010-4

Evaluation of Immunotargeted Gold Nanoshells as Rapid Diagnostic Imaging Agents for HER2-Overexpressing Breast Cancer Cells: A Time-based Analysis

Lissett R. Bickford · Joseph Chang · Kun Fu · Jiantang Sun · Ying Hu · André Gobin · Tse-Kuan Yu · Rebekah A. Drezek

© Humana Press Inc. 2008

Abstract Biomedical nanotechnology offers superior potential for diagnostic imaging of malignancy at the microscopic level. In addition to current research focused on dual-imaging and therapeutic applications in vivo, these novel particles may also prove useful for obtaining immediate diagnostic results in vitro at the patient bedside. However, translating the use of nanoparticles for cancer detection to point-of-care applications requires that conditions be optimized such that minimal time is needed for diagnostic results to become available. Thus far, no reports have been published on minimizing the time needed to achieve acceptable optical contrast of cancer cells incubated with nanoparticles. In this study, we demonstrate the use of gold nanoshells targeted to anti-HER2 antibodies that produce sufficient optical contrast with HER2-overexpressing SK-BR-3 breast cancer cells in only 5 min. This work validates the proof of concept that nanoshells targeted to extracellular biomarkers can be used to enhance cancer diagnostic imaging for use in point-of-care applications.

Keywords nanoshells · point-of-care diagnostics · optical imaging · cancer diagnosis

T.-K. Yu and R.A. Drezek contributed equally to this work.

L. R. Bickford · J. Chang · K. Fu · J. Sun · Y. Hu · R. A. Drezek (✉)
Department of Bioengineering, Rice University,
6100 Main St., MS-142,
Houston, TX 77005, USA
e-mail: drezek@rice.edu

K. Fu · T.-K. Yu
Department of Radiation Oncology,
The University of Texas M.D. Anderson Cancer Center,
Houston, TX 77030, USA

A. Gobin
Department of Bioengineering, University of Louisville,
Louisville, KY 40292, USA

R. A. Drezek
Department of Electrical and Computer Engineering,
Rice University,
Houston, TX 77005, USA

Introduction

Several nanoparticles have been explored for potential applications in cancer diagnosis, including nanoshells [1–4], gold colloid [5, 6], quantum dots [7, 8], carbon dots [9], nanorods [10–12], and nanocrystals [13]. For in vivo applications, several steps will need to be taken to ensure the safe delivery of nanoparticles before they can be used in a clinical setting. However, several opportunities still exist for in vitro applications in which the cytotoxicity of nanoparticles is immaterial. Numerous in vitro technologies that have shown promise for point-of-care diagnostic testing may allow clinicians to provide user-friendly, cost-effective, and rapid results at the patient bedside. Currently, these technologies involve analyzing biological fluids to detect DNA or protein amplification through the use of microarrays or biochip devices [14–16]. In addition to fluid-based modalities, these microscopic advancements can also be used to analyze larger biological components, such as excised tumor specimens, for cancer screening and diagnosis. One particular area of application is the diagnosis of cancer from biopsy samples. For example, after a breast biopsy, the specimen is sent to a pathology laboratory where it is processed and examined microscopically for morphological abnormalities and sometimes analyzed for the presence of molecular biomarkers of

disease, such as hormone receptor expression [17]. This process can take up to several days, during which the patient must cope with the fear of an unknown diagnosis and the potential of treatment delay. Mojica et al. [18] showed that delays between initial breast cancer symptoms and treatment are associated with lower survival rates. Consequently, delays in breast cancer diagnosis top the list of liability claims made against physicians [19].

Another area of opportunity for advancement in point-of-care microscopic analysis of tumor specimens involves the assessment of intraoperative tumor margins. During a lumpectomy, for instance, the surgeon removes the suspected cancerous lesion with a margin of normal tissue. Judgment of the width of this margin is largely based on tactile sensation and visible, macroscopic abnormalities. In advanced hospital systems, the sample is excised and immediately subjected to pathologic analysis to ensure the surgical margins are tumor-free before the procedure is completed. The need to achieve negative margins is critical in minimizing cancer recurrence and progression, particularly for patients undergoing breast conservation therapy [20]. The presence of a positive surgical margin has been associated with lower rates in patient survival [18]. Due to residual cancer cells being left in many patients that undergo breast conservation therapy, as many as 40% of patients have experienced local breast cancer recurrence near the site of the original tumor [21]. Positive margins in a surgical specimen, therefore, necessitate the resection of additional tissue until the margins do not contain tumor. Even if the specimens are examined immediately, this extends the period of anesthesia and hence increases both the cost and risk to the patient. Furthermore, many county hospitals must, by necessity, process tissue samples after the surgery is completed. In that case, the identification of positive surgical margins requires that the patient undergo another surgical procedure to excise the remaining tissue, which further delays the start of adjuvant treatment and increases the risk of cancer recurrence and subsequent patient mortality.

With the expansion of nanotechnology-driven research, opportunities for the use of fast and accurate diagnostic tests outside of the hospital laboratory are likely to increase. To realistically use nanoparticles as a point-of-care tool for the immediate assessment of key cancer gene signatures in excised tissue samples, the time needed to achieve optical contrast must be minimized. Thus far, few published reports have focused on minimizing the time needed to achieve suitable contrast of cancer cells incubated with nanoparticles. Previous studies demonstrating the effectiveness of using gold-based nanoparticles targeted to extracellular cancer biomarkers have involved incubation times ranging from 30 to 90 min [1, 3, 5, 6, 10–12]. The objective of this study was to demonstrate the feasibility of using gold nanoshells targeted to anti-HER2 antibodies to achieve sufficient optical contrast in a HER2-overexpressing breast cancer cell line (SK-BR-3) after a series of incubation times. Overexpression of the HER2 receptor is associated with greater cancer progression and is seen in approximately 15–25% of all breast cancer cases [17]. The nanoshells, made of dielectric silica particles covered with a thin gold shell, were fabricated to scatter strongly in the near-infrared spectrum through manipulation of the silica core/gold shell ratio. We compared the contrast that could be achieved by incubating the nanoshells with both normal and cancerous cells. Our results demonstrate that gold nanoshells targeted to this cell-surface marker can produce enhanced contrast after only 5 min of incubation. This proof of concept supports the initial feasibility of using gold nanoshells for potential point-of-care diagnostic applications.

Materials and Methods

Nanoshell Fabrication

Nanoshells were developed and bioconjugated by using previously reported procedures [22]. First, silica cores were prepared with the Stöber method [23], in which tetraethyl orthosilicate (Sigma Aldrich) is reduced in ammonium hydroxide and pure ethanol. Next, aminopropyltriethoxysilane was used to functionalize the particles by terminating the silica core surface with amine groups. The silica particles were then measured by scanning electron microscopy (SEM) to obtain the average silica core diameter of 254 nm.

To create the gold shell overlap for the silica cores, gold colloid of 1–3 nm in diameter was fabricated based on procedures documented by Duff et al. [24]. The gold colloid solution was stored at 4 °C for 2 weeks and subsequently concentrated with a Rotovap. After aging and concentration, the gold colloid solution was added to the aforementioned functionalized silica particles, forming ‘seeds’ in which the gold colloid is adsorbed to the amine groups of the silica cores. To complete nanoshell fabrication, a cocktail of hydrogen tetrachloroaurate trihydrate ($HAuCl_4$) and potassium carbonate was added to the seeds along with formaldehyde to catalyze the formation of the shells. The spectrum of the completed nanoshells was analyzed with a UV-vis spectrophotometer (Varian Cary 300). The relationship between the extinction spectrum obtained by UV-vis spectroscopy and that obtained by application of the Mie scattering theory can be used to approximate the size of the nanoparticles in solution (Fig. 1). Subsequently, Mie Theory can be used to derive the absorption, scattering, and extinction coefficients for nanoparticles of a specific size, and a standard known

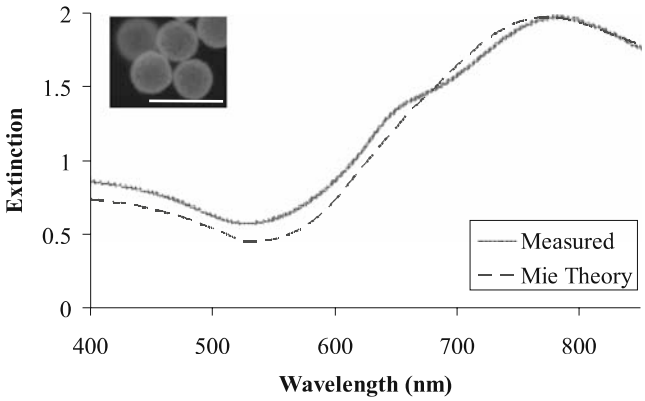

Fig. 1 Measured spectra of nanoshells (core radius, 127 nm; shell thickness, 19 nm) as compared with that estimated using the Mie scattering theory; the *insert* depicts the corresponding image from scanning electron microscopy. *Scale bar* represents 500 nm.

concentration can be acquired for a particular optical density. In addition to using Mie scattering theory for multilayer spheres, we also used SEM to confirm the size of the nanoshells. The nanoshells used in this study had an average diameter of 292 nm, a peak surface plasmon resonance at 778 nm and a concentration of approximately 1.6×10^9 particles/ml.

Nanoshell Surface Modification

To target the prepared nanoparticles to molecular markers associated with HER2-overexpression, antibodies were first prepared by methods previously described by Hirsch et al. [22]. Briefly, anti-HER2 antibodies (C-erbB-2/HER-2/*neu* Ab-4, Lab Vision Corporation) were conjugated to the heterobifunctionalized polyethylene glycol linker orthopyridyl-disulfide-PEG-*N*-hydroxysuccinimide ester (OPSS-PEG-NHS, MW=2 kD, CreativeBiochem Laboratories) by reaction at a molar ratio of 1:3 in sodium bicarbonate (100 mM, pH 8.5) overnight on ice. Aliquots were stored at −80 °C. The amidohydroxysuccinimide group (NHS) enables conjugation of the PEG linker to the antibodies through amide linkages; the remaining end of the PEG linker, OPSS, allows binding to the nanoshell gold surfaces through sulfur groups. The nanoshells (1.6×10^9 particles/ml) were incubated with the prepared anti-HER2-PEG solution (0.4 mg/ml) for 1 h at 4 °C. The newly conjugated nanoshells were subsequently incubated with a 10 μM polyethylene glycol-thiol solution (PEG-SH, MW=5 kD, Nektar) for 2 additional hours at 4 °C, which stabilized the nanoshells by blocking any unoccupied adsorption sites. The nanoshells were then centrifuged to remove unbound antibodies, resuspended in ultrapure water, and stored at room temperature until use. Before being incubated with cells, the nanoshell solution was supplemented with bovine serum albumin and phosphate-buffered saline (PBS) at final concentrations of 1% each.

Preparation of Cells

Two cell types were analyzed for this study: the HER2-overexpressing epithelial breast cancer cell line SK-BR-3 and the normal mammary epithelial cell line MCF10A (American Type Culture Collection). The SK-BR-3 cells were grown in McCoy's 5A medium supplemented with 10% fetal bovine serum and 1% penicillin-streptomycin and maintained at 37 °C in a 5% CO_2 atmosphere. The MCF10A cells were cultured in Mammary Epithelial Basal Medium (MEBM) supplemented with a BulletKit (Clonetics) and also maintained at 37 °C in 5% CO_2. Both cell lines were grown in 25-cm^2 culture flasks until confluent. At that time, cells were rinsed once with 1× PBS and incubated with trypsin-ethylenediaminetetraacetic acid for 5 min at 37 °C to detach the cells from the substrate, after which trypsin was neutralized with the appropriate medium and the cells were counted. Approximately 6×10^5 cells were placed in each of four conical tubes per cell line for each time point under investigation. The cells were then centrifuged at 115×*g* for 3 min. For each cell line and each time point of interest, three cell pellets were resuspended in the bioconjugated nanoshell solution, and one was resuspended in an equal amount of PBS as a control. The nanoshell–cell suspensions and controls were then incubated in a hybridization chamber (VWR International) at 37 °C and a motor speed of 7 rpm for 5, 10, 30, or 60 min. After incubation, the suspensions were centrifuged at 115×*g* for 3 min, and the unbound nanoshells were collected with a pipette. Cells were then rinsed once with 1× PBS, centrifuged, and the unbound nanoshells were again collected. A small volume (5 μl) of 10% glucose mixed with PBS was added to the remaining cell pellets to prevent cell death during imaging. Approximately 7 μl of each pellet was placed on a glass slide and coverslipped for immediate microscopic analysis.

Darkfield Imaging and Processing

Images of the two cell types incubated with nanoshells were obtained with a Zeiss Axioskop 2 darkfield microscope outfitted with a color camera (Zeiss AxioCam MRc5). Darkfield microscopy depends on light scattering to achieve contrast. All images were taken under the same lighting conditions and magnification (×20). Optical intensity was quantified by using a Matlab code. Based on this code, an image with a value of 0 was designated pure black and that with a value of 255 pure white. An increase in intensity, therefore, corresponded to an image with a higher numerical value. Average intensity values for each time point and each cell line were calculated from ten independent cell samples that were devoid of scattering influences from neighboring cells and unbound nanoshells. Sample normality was assessed by using Minitab to evaluate the error

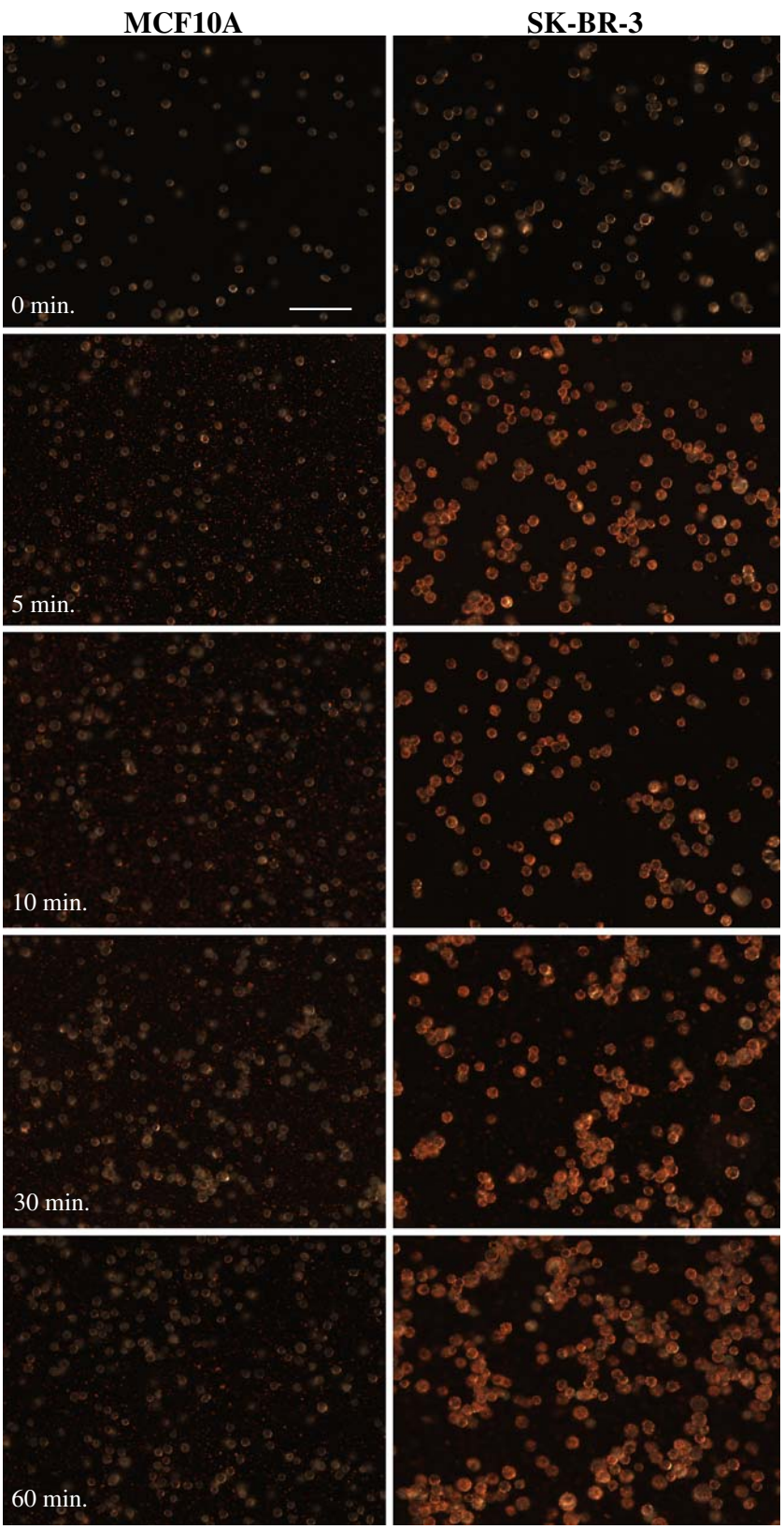

Fig. 2 Darkfield images of MCF10A and SK-BR-3 cells incubated with bioconjugated nanoshells for the indicated times. Images were obtained at ×20. *Scale bar* represents 125 μm.

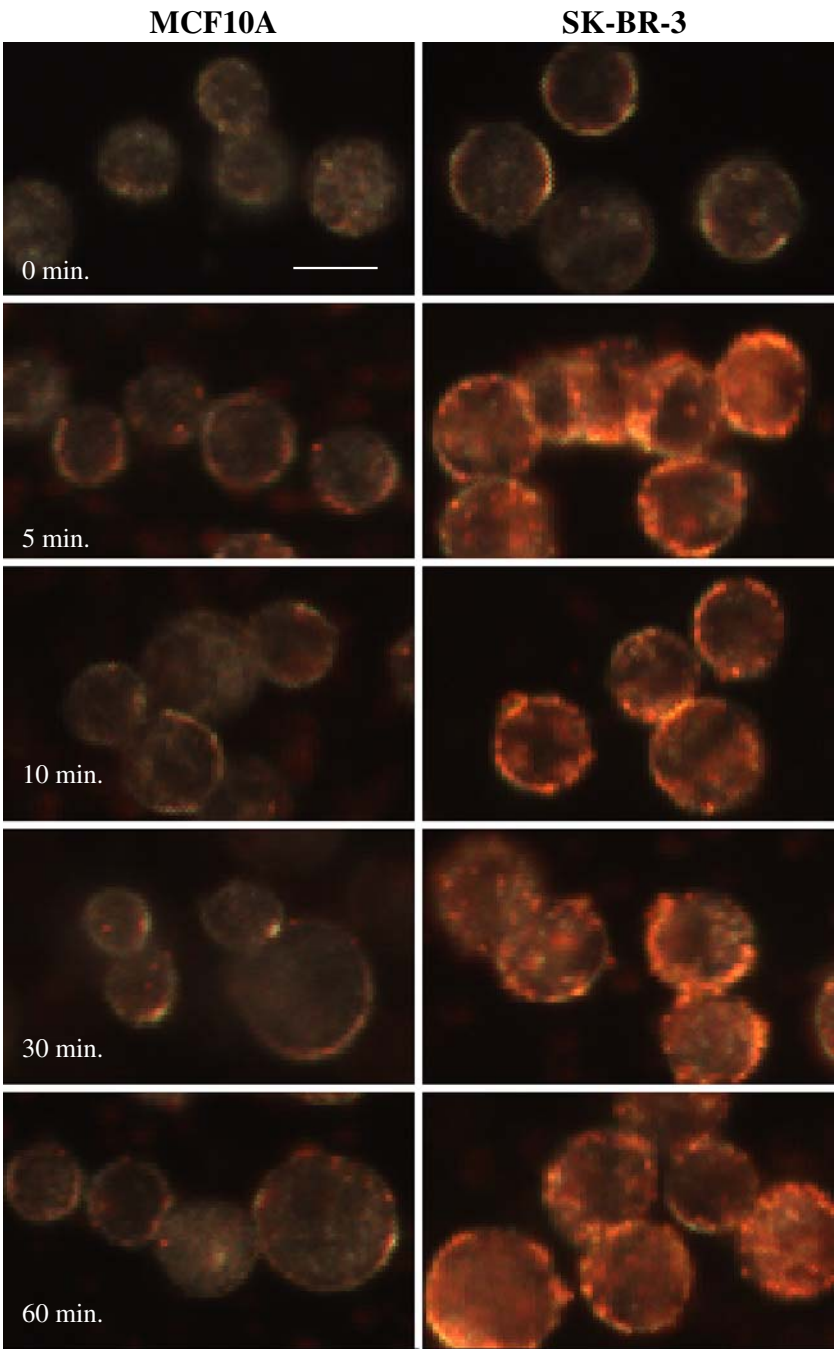

Fig. 3 Enlarged darkfield images of MCF10A and SK-BR-3 cells incubated with the bioconjugated nanoshells for the indicated times. Original images taken at ×20. *Scale bar* represents 20 μm.

distribution for all data points. A normal probability plot of the residuals verified that the samples followed a normal distribution (data not shown). *F* tests were also used to determine the equality of variance before applying two-tailed paired Student's *t* tests to evaluate significance.

Derivation of Bound Nanoshell Concentration using Spectroscopy

According to the Beer–Lambert law, the absorbance of particles in solution is directly related to the concentration of those particles in that solution. To validate the ability of spectroscopy to predict the concentration of a solution of nanoshells of known size, we used linear regression analysis. Nanoshells of known concentration, based on the Mie Theory calculations, were serially diluted and, the corresponding peak absorbance values were measured. We considered a concentration of approximately 2.0×10^9 particles/ml (optical density=2.4) as a 100× concentration. From this analysis, an equation relating the peak absorbance (independent variable) to each known nanoshell concentration (dependent variable) was used to approxi-

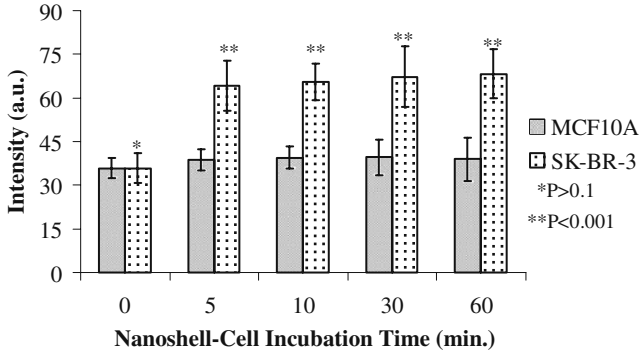

Fig. 4 Mean quantitative intensity values for samples of MCF10A and SKBR3 cells incubated with nanoshells for the indicated times. Differences between cell types incubated without nanoshells were not statistically significant ($P>0.1$, $n=10$). Differences between cell types incubated with nanoshells were statistically significant at all time points ($P<0.001$, $n=10$). *Error bars* indicate standard deviations.

mate the number of nanoparticles in subsequent solutions of unknown concentration. This derivation was necessary to calculate the approximate number of bound nanoparticles per cell at the different time points.

To determine and compare the number of nanoshells bound after 5 min and 60 min of incubation, the collected unbound nanoshells were centrifuged at 255×*g* for 20 min, resuspended in ultrapure water, transferred to cuvettes and sonicated briefly before being measured with a UV-vis spectrophotometer. The spectrum was recorded and the peak absorbance documented for each sample. Based on the original concentration of nanoshells, the number of cells used, and the concentration of the collected unbound nanoshells, the approximate number of nanoshells bound to each cancer cell was derived. An *F* test was also used to determine the equality of variance before applying a two-tailed paired Student's *t* test to evaluate significance.

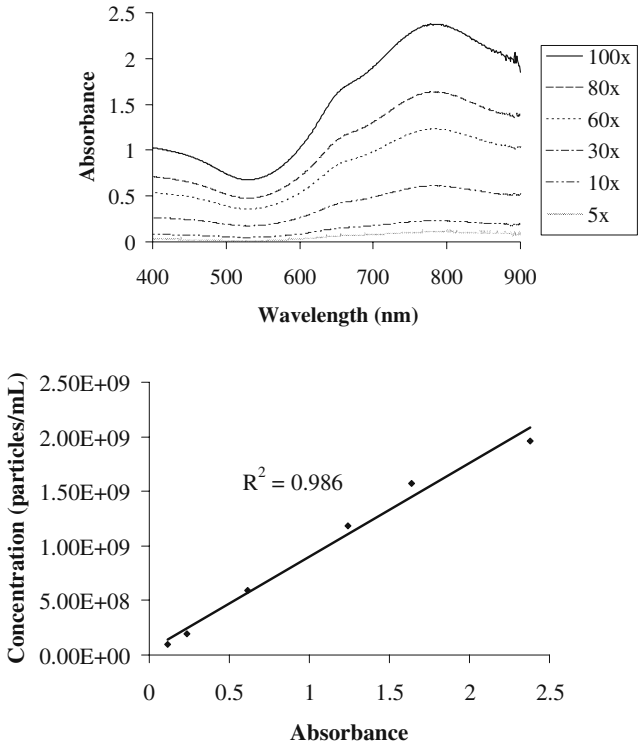

Fig. 5 *Top* Spectra of serial dilutions of known nanoshells concentrations in suspension. *Bottom* Linear regression analysis of known nanoshell concentrations vs. the corresponding peak absorbance values.

Results/Discussion

We evaluated the contrast that could be achieved by incubating nanoshells targeted to HER2 receptors with normal breast epithelial cells (MCF10A) or breast cancer cells (SK-BR-3) for four intervals: 5, 10, 30, and 60 min. All procedures were done with triplicate samples and included a control condition (cells to which no nanoshells had been added). Figures 2 and 3 illustrate original and enlarged images obtained at all four time points for both cells lines and for cells incubated without nanoshells (designated as 0 min). Because the optical peak resonance for the fabricated nanoparticles occurred at 778 nm, the nanoshells scattered strongly in the near-infrared range and could be visualized under darkfield illumination as red particles. Qualitative assessment of the imaging results revealed that the MCF10A cells showed little enhanced scattering at any period of incubation with the bioconjugate–nanoshell solution compared with both controls or the cancer cells. However, the SK-BR-3 cancer cells showed enhanced contrast after as little as 5 min of incubation. Typically, SK-BR-3 cells express about 8×10^5 receptors per cell and normal MCF10A cells about 1×10^4 [25, 26]. The targeted bioconjugated nanoshells apparently bound to cell surface receptors on both cell types; however, because the cancer cells had higher numbers of receptors, the contrast that could be achieved was considerably greater with those HER2-overexpressing cells. Other evidence of the superior contrast achieved with the SK-BR-3 cells was apparent from the difference in the numbers of unbound nanoshells between the two cell types. In the images of the

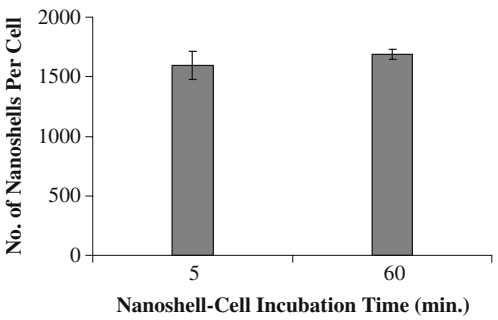

Fig. 6 Number of nanoshells bound per SK-BR-3 cell after 5 and 60 min of incubation. Values shown are the means of triplicate measurements. *Error bars* indicate standard deviations.

MCF10A cells, several unbound nanoshells could be seen between cells despite our attempts at removing unbound nanoshells by rinsing the cells. Considerably fewer such nanoshells were present in the SK-BR-3-nanoshell images (Fig. 2).

To quantitatively assess the increase in contrast between the normal and cancerous cells at each time point, we used a Matlab code to evaluate the average intensity of ten cells from each condition; an intensity value of 0 was considered pure black and 255 pure white. Statistical analyses indicated no difference between either cell type incubated with only PBS (the control condition; $P>0.1$). However, differences between the MCF10A cells and the SK-BR-3 cells were significant at all four incubation times ($P<0.001$; Fig. 4). An additional analysis of variance showed no differences in the mean intensity of the SK-BR-3 cells at any of the four incubation times ($P>0.5$).

To further compare the differences between contrast that could be achieved at 5 and 60 min for the SK-BR-3 cells, we examined the number of bound nanoshells at both time points. To do so, we first developed a simple UV-vis spectroscopy method to determine the concentration of nanoshells in solution. On the basis of dilutions of known nanoshell concentrations, we used linear regression to estimate the concentration of nanoshells in a given solution (Fig. 5). We confirmed the existence of a linear relationship between absorbance and corresponding concentration of nanoshells for concentrations ranging from 9.8×10^7 to 2.0×10^9 particles/ml. With a goodness-of-fit (R^2) value of 0.986, we concluded that the absorbance accurately predicts the concentration of an unknown suspension of nanoparticles that falls within this range.

We next used this relationship between absorbance and concentration to measure the absorbance of unbound nanoshells collected after incubation and cell rinsing and subsequently resuspended in a volume of water equal to that of the diluted samples of known concentration. Knowing the initial number of nanoshells and cells, we could derive the approximate number of nanoshells bound to each cell, which we did for the triplicate samples of nanoshells plus cells after 5 and 60 min of incubation. At 5 min of incubation, 1,593±121 nanoshells were bound per cell; at 60 min, the range was 1,686±40 nanoshells per cell ($P>0.1$, not significant; Fig. 6). Thus, roughly 95% of the binding noted at 60 min had occurred within the first 5 min of incubation. Our imaging results suggest that this 5% difference did not seem to affect contrast.

Conclusions

Our findings support the proof of concept that optical contrast of HER2-overexpressing breast cancer cells can be achieved by brief periods of incubating those cells with nanoshells. Although the ability to detect malignancy by such means is critical for in vivo applications and for in vitro applications associated with biological fluids, other opportunities exist for using such techniques to diagnose solid tumor specimens in vitro. The time between diagnosis and treatment could be drastically shortened by the use of microscopic evaluations of excised tissue samples that provide rapid and reliable results. We have shown both qualitatively and quantitatively that nanoshells can be used to achieve discernible contrast between cancerous and normal breast cells in 5 min. These results suggest that gold nanoshells can be designed and optimized to enhance the scattering signatures of cancer cells at minimal incubation times necessary for potential applications in point-of-care cancer diagnostic imaging. Future studies are underway to extend these findings from the cellular level to tumor specimen models.

Acknowledgments We thank Vengadesan Nammalvar and Adrien Wang for expert technical assistance on nanoshell fabrication. We also thank Nastassja Lewinski for SEM imaging and Christine Wogan for editing assistance. This work was supported by a Department of Defense Congressionally Directed Breast Cancer Research Program Era of Hope Scholar Award to Rebekah Drezek and Tse-Kuan Yu, the Center for Biological and Environmental Nanotechnology (EEC-0118007 and EEC-0647452), the Beckman Foundation, and the John and Ann Doerr Fund for Computational Biomedicine.

References

1. Loo C, Lowery A, Halas N, West J, Drezek R. Nano Lett 2005;5(4):709–11.
2. Loo C, Hirsch L, Lee M-H, Chang E, West J, Halas N, Drezek R. Optics Lett 2005;30:1012–4.
3. Lowery A, Gobin A, et al. Int J Nanomed 2006;1:149–54.
4. Gobin AM, Lee MH, Halas NJ, James WD, Drezek RA, West JL. Nano Lett 2007;7:1929–34.
5. Sokolov K, Follen M, Aaron J, Pavlova I, Malpica A, Lotan R, et al. Cancer Res 2003;63:1999–2004.
6. El-Sayed IH, Huang X, El-Sayed MA. Nano Lett 2005;5(5):829–34.
7. Sun J, Zhu MQ, Fu K, Lewinski N, Drezek R. Int J Nanomed 2007;2(2):235–40.
8. Gao X, Cui Y, Levenson RM, Chung LW, Nie S. Nat Biotechnol 2004;22(8):969–76.
9. Cao L, et al. J Am Chem Soc 2007;129:11318–9.
10. Huang X, El-Sayed IH, Qian W, El-Sayed MA. J Am Chem Soc 2006;128:2115–20.
11. Durr NJ, Larson T, Smith DK, Korgel BA, Sokolov K, Ben-Yakar A. Nano Lett 2007;7:941–5.
12. Yu C, Nakshatri H, Irudayaraj J. Nano Lett 2007;7(8):2300–6.
13. Sukhanova A, Devy J, Venteo L, Kaplan H, et al. Anal Biochem 2004;324:60–7.
14. Zajac A, Song D, Qian W, Zhukov T. Colloids Surf B Biointerfaces 2007;58:309–14.
15. Weigum SE, Floriano PN, Christodoulides N, McDevitt JT. Lab Chip 2007;7(8):995–1003.

16. Culha M, Stokes DL, Griffin GD, Vo-Dinh T. JBO 2004;9 (3):439–43.
17. National Comprehensive Cancer Network. Breast cancer treatment guidelines for patients. Version IX. 2007.
18. Mojica CM, Bastani R, Boscardin WJ, Ponce NA. Cancer Control 2007;14(2):176–82.
19. Guthrie TH. Breast J 1995;1(6):376–9.
20. Klimberg VS, Harms S, Korourian S. Surg Oncol 1999;8:77–84.
21. Fisher B, Anderson S, Bryant J, Margolese RG, Deutsch M, Fisher ER, Jeong JH, Wolmark N. NEJM 2002;347:1233–41.
22. Hirsch LR, Halas NJ, West JL. Methods Mol Biol 2005;303:101–11.
23. Stöber W, Fink A, et al. J Colloid Interface Sci 1968;26:62–9.
24. Duff DG, Baiker A, Edwards PP. Langmuir 1993;9:2301–9.
25. Hayes DF, Walker TM, et al. Int J Oncol 2002;21(5):1111–7.
26. Kornilova ES, Taverna D, et al. Oncogene 1992;7(3):511–9.